A 3-D Finite Difference Time Domain Investigation
of Microwave Propagation Through Inhomogeneous
Biological Materials

THESIS
David B. Dunn Jr.
Second Lieutenant, USAF

AFIT/GE/ENG/94D-05

19941228 115

DEPARTMENT OF THE AIR FORCE
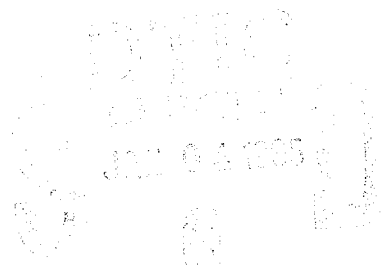**AIR UNIVERSITY**

AIR FORCE INSTITUTE OF TECHNOLOGY

Wright-Patterson Air Force Base, Ohio

A 3-D Finite Difference Time Domain Investigation
of Microwave Propagation Through Inhomogeneous
Biological Materials

THESIS
David B. Dunn Jr.
Second Lieutenant, USAF

AFIT/GE/ENG/94D-05

The views expressed in this thesis are those of the author and do not reflect the official policy or position of the Department of Defense or the U. S. Government.

Accesion For		
NTIS CRA&I		☒
DTIC TAB		☐
Unannounced		☐
Justification		
By		
Distribution /		
Availability Codes		
Dist	Avail and / or Special	
A-1		

A 3-D Finite Difference Time Domain Investigation of Microwave Propagation Through Inhomogeneous Biological Materials

THESIS

Presented to the Faculty of the School of Engineering

of the Air Force Institute of Technology

Air University

In Partial Fulfillment of the

Requirements for the Degree of

Master of Science in Electrical Engineering

David B. Dunn Jr., BSEE

Second Lieutenant, USAF

Dec, 1994

Table Of Contents   Page Number

iii

Acknowledgements

I would like to extend my sincerest thanks to the people that helped this thesis come to fruition. First and foremost, I'd likt to thank my wife, Katie who put up with a lot of added stress in a year already containing more than any individual should have to endure, and my parents who have been working hard to spend my inheritence forcing me to get a higher education.

I'd also like to thank the many professors who have added invaluable insight to my research. Special thanks are given to Dr. Rappaport of Northeastern University for providing excellent guidance throughout my quest for understanding. Thanks to Dr. Richard Albanese, Dr. Raymond Luebbers, Dr. Andrew Terzuoli, Dr. Matt Kabrisky, Maj Gerry Gerace, and Captain Joe Sacchini for their insight, input and suggestions. Thanks to all the professors who provided insight on the many conference calls including Dr. Leo Felsen and Dr. Alan Fenn. I'd also like to thank Mr. David Steich for allowing the use of the head mesh he developed from an MRI scan.

Finally a special thanks to my friends here at AFIT for helping to keep things in perspective throughout the past year and a half. A special thanks to Russ Burleson for helping to explain all those very basic, yet essential concepts I failed to learn in class, and for providing invaluable motivation when things were looking bleak.

List of Tables

Abstract

This paper extends past analysis of an optimal source distribution around a

homogeneous sphere of muscle tissue by using a 3-D finite difference time domain (FDTD)

scenario in which an anatomically correct human head model is irradiated. It first

duplicates the analytical solution within an FDTD space using an FDTD computer code

developed at Penn State University. This duplication uses a 9.45 cm radius sphere

represented in an FDTD space of 2.55 mm cubic cells. FDTD simulations are then

peformed on four, three, and two layer laminated spheres, designed to provide simple

models of a head. Finally, four simulations were performed in FDTD on the human head

model developed at Penn State from an MRI scan of an actual human head. The

comparison of analytic simulations to the FDTD simulations on a homogeneous sphere

showed a pixel by pixel average of 5.34% error between the two with a standard deviation

of 7.84%. The layered sphere models showed considerable spiking at the two poles along

with a small amount of spiking due to the stair-step approximation of the spheres. None of

these spikes increased the power beyond that at the surface and hence were not critical.

The simulations on a true human head showed improvement in depth due to the low-loss of

the bone tissue. This study demonstrates that microwave hyperthermia with good

resolution is possible in an anatomically correct head model.

1. Introduction

Cancer has been a leading cause of death in the United States for several decades and remains so today; therefore, it is a leading topic of research. Current researchers employ several methods to destroy and limit the growth of cancerous tissue. However, all methods contain a similar characteristic; they destroy the healthy tissue as well as the tumor. One promising form of treatment for cancer, for limiting the damage to healthy tissue, is non-invasive hyperthermia. In this method of therapy either ultrasound or electromagnetic waves are inserted into the tissue from many different locations. These waves induce molecular vibrations that heat and kill the cancer. The waves pass through the tissue and cross at one point where constructive interference occurs. At this location, the waveform amplitude is significantly higher than at any other point in the tissue. Since the amplitude of the wave dictates the amount of molecular vibration and the amount of vibration in turn dictates the amount of heat, the amplitude controls the heat produced. In other words, the location of constructive interference, with its increased amplitude, is heated more than other locations in the tissue.

The current drawback to non-invasive hyperthermia is achieving the optimal solution of resolution and deep penetration. The two waveforms, ultrasound and electromagnetic waves, used in this treatment both have their limitations. Ultrasound provides good resolution, however, it has large reflections at the boundaries of the different materials. These reflections make it difficult to treat tumors near dense bone tissue or open air cavities, such as tumors in the head or chest. Electromagnetic waves, on the other hand, can penetrate these substances with little reflection, but high frequencies have not been able to penetrate deeply into high water-content tissue such as muscle.

Problem Statement

This research focuses on using high-frequency electromagnetic waves as part of non-invasive hyperthermia in treating brain cancers. Although deep penetration through the

muscular tissue of the brain has been impossible in the past, this study will show that with the combination of high frequencies and constructive interference, resolution at depth improves and electromagnetic waves become the treatment of choice.

Summary of Chapters

This thesis is broken into six main chapters, introduction, background, theory, methodology, results and conclusions. The introduction you have just completed reading and requires little explanation. The background section describes the work that has been done in the past on sphere analysis, FDTD development, and material characteristics of biological tissue. The theory section provides a brief survey of the theories necessary to complete the research set out in this thesis. This includes a description of Rappaport's optimization process and Luebbers' FDTD code. The Methodology section describes the modifications made on Luebbers' code as well as the configuration of each of the FDTD simulations. The results section describes the power patterns created from each FDTD simulation. Finally, the conclusion section provides the conclusions which can be drawn from this research as well as some suggestions for future work.

2. Background

A significant amount of research has evolved the tools necessary to carryout a task as difficult as analyzing an inhomogeneous 3-D model of an actual human head. The most important is the work by Rappaport to derive an optimal field distribution for irradiating a tumor within a homogeneous sphere of muscle tissue. This research demonstrates the potential of microwave hyperthermia. To apply this theory to the inhomogeneous structure of a human head, this thesis will implement the finite difference time domain technique for electromagnetics. This theory approximates Maxwell's derivative equations as finite differences and directly solves them across time and space. Finally, a good understanding of the electrical properties of biological tissues was necessary to model adequately the different tissue types of a human head.

2.1 The Sphere Analysis

Current research analyzes only perfect spheres of homogeneous tissue [1,2,3,4]. Dr. Carey Rappaport at Northeastern University leads the work in spherical source radiation for hyperthermia treatment of cancer. In his work he has dealt solely with analytic solutions to homogeneous spheres. He began with the optimization of a spherical source distribution to irradiate a tumor at the center of a sphere of homogeneous tissue. Following the analysis at the center of a sphere, he continued on to investigate heating off-center targets with both a longitudinally and azimuthally polarized E-field.

The earliest work comes from Dr. Rappaport and Dr. Morgenthaler, a professor at Massachusetts Institute of Technology [1]. They place a tumor at the center of a sphere of muscle tissue and determine the maximum radius through which the tumor can be heated. By determining the maximum radius with an ideal distribution, this research produces a benchmark other methods such as adaptive nulling can try to obtain but never improve. To define this maximum radius, they first set up a uniform amplitude and longitudinally polarized current distribution around the sphere. They then calculate the radiation pattern

4

within the sphere. To kill only the cancer cells it is imperative the power at the focus be greater than at all other points within the sphere. An analysis of the power distribution which the surface current produces reveals that the point where power at the surface is the same as that at the focus defines the maximum depth obtainable. A power profile along the axis of the sphere is computed for several frequencies from 100 MHz to 2 GHz. The large range of frequencies tested was to examine the differing characteristics of high and low frequencies. Higher frequencies have better precision but exceptionally small penetration depths, whereas lower frequencies have excellent penetration but poor precision. This analysis shows the optimal frequency to be 915 MHz. This occurs because, due to the electrical characteristics of the muscle tissue, 915 MHz actually has better precision and better depth than the next frequency down, 700 MHz. Rappaport and Morgenthaler compute the maximum radius to be just under 9 cm for 915 MHz.

To increase this maximum radius obtainable, Rappaport and Morgenthaler turn to a modal analysis in which they add higher order spherical harmonics to the field distribution around the sphere. The modal analysis allows higher order modes, which have no power at the center, to destructively interfere near the edges around the equator of the sphere. Since surface power is highest at the equator of the sphere, this technique attempts to force the surface power around the equator to decrease, spreading that energy toward the poles. However, even with these higher harmonics, the theoretical maximum radius through which a tumor can be heated increased to only 9.45 cm from 9 cm at 915 MHz. Although this is close to a typical head size, it assumes an ideal source; thus, achieving it in practice would be impossible.

Rappaport, with his graduate student Pereira, then turned toward radiating off center targets. The one difference between the off-center heating scheme and the center heating configuration lies in polarization. For a tumor located at the center of a sphere, the polarization of the field at the focus is not a factor. The polarization of the field distribution on the surface must be in the same direction over the entire surface; however, the direction

of this polarization is unimportant. If there is the desire to have another polarization at the center of the sphere, the source distribution need only to be rotated about the outside of the sphere. If the field distribution rotates in the case of an off-center focus, the location of the focus would move.

The off-center focus requires two separate derivations, one for each polarization. To define these polarizations, it is necessary to define two axes of the sphere. The first axis defined passes directly through the center of the tumor and is therefore called the centered axis. The second axis simulations perpendicular to the first and is labeled the off-center axis. Figure 1.1 illustrates the two axes' definitions. The polarization is then set parallel to the off-center axis (azimuthal polarization) or parallel to the centered axis (longitudinal polarization).
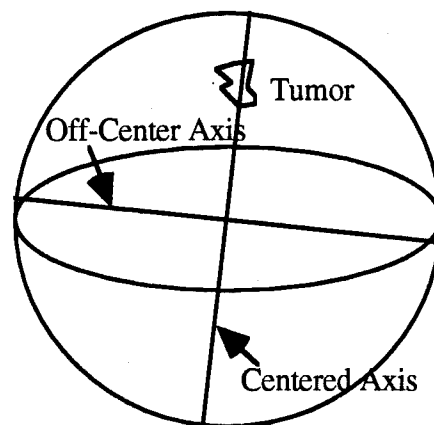
Figure 2.1: This figure illustrates the definition of the centered and off-center axes.

Rappaport and Pereira's paper looks at longitudinal polarization. They closely followed what Rappaport had done with Morgenthaler [2,3]. The difference is the location of the origin. For the off-center study, they locate the origin of analysis at the tumor location. Computing the fields that correspond to a source at that location, they set up a field distribution that focused at the off-center location. In other words, they place the center of the spherical wave distribution at the tumor location and determine the

6

corresponding field at locations on the surface of the sphere. With a modal analysis similar to the one used for heating a centered target, they are able to increase precision at the off center location. For heating a location at six-tenths of the radius, they are able to penetrate through a 12 cm radius sphere at 915 MHz.

Upon completing the longitudinal analysis with Pereira, Rappaport published a paper looking at the azimuthal polarization of the off-center target[4]. The azimuthal polarization analysis entails a similar analysis as the longitudinal, except polarization of the field is parallel to the off-center axis. This polarization is not as effective as longitudinal polarization. For treatment at six-tenths of the radius Rappaport is only able to penetrate through a 9 cm radius sphere at 915 MHz. It is possible to understand the difference from an intuitive sense. The maximum power addition comes from the sources near the equator of the source distribution, for these are the strongest sources. For the longitudinal case, these sources all lay equal distances from the tumor. In azimuthal polarization some of these tangential sources are located further than the sphere's radius away. Transmission through lossy tissue attenuates the field significantly, reducing the power contribution of these sources, which in turn reduces the maximum radius through which tumor treatment is possible.

2.2 FDTD Background

The computational finite difference time domain (FDTD) method also provides a method for analysis of electromagnetic wave propagation through tissue. FDTD breaks time and space into finite increments. It then applies Maxwell's equations directly to this grid, with the derivatives approximated as differences. Dr. Raymond Luebbers of Penn State University developed a general purpose 3-D FDTD code that is extremely versatile and easy to use [5]. It includes a graphical user interface (GUI) for inputting the geometries as well as displaying results. Although developed for backscatter predictions and antenna design problems, this codes versatility allows straightforward modification to handle a biological tumor treatment scenario. In addition, Mr. David Steich has produced a

7

human head model capable of use with this FDTD code. This geometry mesh was created from an MRI scan of an actual human head. It is important to note that this is an approximate model but will prove to be adequate for judging the effects of the inhomogeneities of the human head.

Om Ghandi and Carl Durney at the University of Utah have done a great deal of research in the field of biological FDTD research. Their research concerns the biological effects of electromagnetic waves, rather than the treatment of biological tumors. However, the methods they use to predict field propagation through tissue directly apply to the treatment scenario [6].

The research done by Ghandi and Durney has two important lessons that pertain to my research. First, It demonstrates the versatility of the FDTD code as a tool for analyzing electromagnetic effects in biological tissue. The grid set up in FDTD may contain several different electric or magnetic materials in virtually any configuration. This allows relatively easy modeling of the complex, inhomogeneous structure of the human body. The study also demonstrates the limits of actual applicators. Rappaport's studies, as well as mine, assume the ability to produce an E-field distribution exactly as desired. The study by Durney et. al. shows that in practice this will be nearly impossible because of the capacitive effects that occur due to the high conductivity of the muscle tissue. The muscle acts as a second plate of a parallel plate capacitor, hence the field does not behave as it would for a simple radiating dipole [6]. It is essential to keep this drawback in mind when doing research with ideal distributions. The ideal distribution will never be obtainable; therefore, to have hope of a workable system, the ideal maximum depth must be somewhat deeper than real applications will ever encounter. This will allow for the loss of depth that will come as a result of the inability to create a source distribution exactly as predicted in the ideal scenario.

2.3 Electrical Properties of Human Tissue

Curtis Johnson and Arthur Guy published a paper in 1972 from which most research in 1993 has obtained model electrical characteristics for human tissue [7]. In this paper, they discuss the electric properties of differing forms of tissue. The study shows that muscle tissue is the lossiest tissue of the human body. That is, electromagnetic waves attenuate more quickly through muscle than any other form of tissue. This characteristic dictates muscle tissue as the tissue of choice for calculating the performance of electromagnetic treatment. This provides a worst- case scenario. In a real head model, there is relatively low-loss bone tissue and open air cavities. This means more boundary reflections, but also means less loss as the wave propagates through the tissue.

In 1980 Stuchly and Stuchly published a more complete set of dielectric properties of biological tissues [8]. This list breaks down the material characteristics more completely, giving the permitivities of bone, muscle, white matter, gray matter, etc. This indicates the brain itself also has lower loss than muscle tissue. Thus, there remains the possibility that a small deep-set tumor within an actual human head model may be treatable, given an optimal source distribution.

The research done to date indicates that although there are certain limitations to electromagnetic hyperthermia treatment for cancer reduction, the technique still holds many benefits over other forms of hyperthermia and is worthy of continued study. The limited precision at deep locations is a shortcoming of electromagnetic waves that is avoidable, as seen in Rappaport's work and will be shown here. In any event, it is an area that clearly deserves more research. The inability of ultrasound to penetrate bone and air pockets makes it impossible to use ultrasound waves for treatment in the skull and chest region. The low loss of bone tissue and air cavities leaves electromagnetics a strong contender for future research in cranial and cardial tumors. Optimization of the source distribution using an FDTD analysis of an inhomogeneous head can be done to develop a microwave system capable of heating only the cancerous tissue, leaving the remaining tissues unharmed.

3. Theory:

There are two main theories used throughout this research. The first is the Finite Difference Time Domain (FDTD) technique for electromagnetics. This theory uses finite difference approximations for the derivatives of Maxwell's equations. It then cycles through time steps and solves these equations at every location within the FDTD space. In this way predicting the propagation of electromagnetic waves through complex media is a matter of solving millions of simple calculations. The second theory to be understood is the solution to the vector wave equation in spherical coordinates and how it applies to the optimization technique developed by Rappaport. This theory defines the optimal source distribution for irradiating deep set tumors.

3.1 Finite Difference Time Domain Technique

Unlike Rappaport's work, this thesis will not use an analytic approach for solving for the electromagnetic fields. Instead, it uses a numerical approximation technique known as the Finite Difference Time Domain (FDTD). FDTD approximates the differential form of Maxwell's equations with finite differences. To do this, it is necessary to break both time and space down into small increments. The method then directly applies Maxwell's equations to each of these cubes at each time increment thereby propagating the electromagnetic fields through the space. This allows application of any material characteristic to any cube within the space, making analysis of inhomogeneous bodies in the near field exceptionally simple. The following derivation is from [9].

As stated above, FDTD is simply a finite difference application of Maxwell's equations in differential form. Let us therefore begin at Maxwell's equations in differential form in the time domain.

10

$$\nabla \times \mathbf{E} = -\partial \mathbf{B} / \partial t$$

$$\nabla \times \mathbf{H} = \partial \mathbf{D} / \partial t + \mathbf{J}$$

$$\nabla \cdot \mathbf{D} = \rho$$

$$\nabla \cdot \mathbf{B} = 0$$

Where

$$\mathbf{D} = \varepsilon * \mathbf{E}$$

$$\mathbf{B} = \mu * \mathbf{H}$$

It is important to stop and point out that the constitutive relations here are convolutions and not simple multiplications. This is because these equations apply to the time domain, and not the frequency domain. Because the equations in the frequency domain are multiplications, in the time domain they become convolutions. If we deal with only one frequency and assume a scalar permitivity and permeability, multiplications replace these convolutions.

Before going any further, we can reduce the derivation to only the two curl equations by noting that the divergence equations are redundant. To show these are unnecessary, start by taking the divergence of each of the curl equations.

$$\nabla \cdot (\nabla \times \mathbf{E}) = \nabla \cdot \left(-\frac{\partial \mathbf{B}}{\partial t} \right) \quad (1)$$

$$\nabla \cdot (\nabla \times \mathbf{H}) = \nabla \cdot \left(\frac{\partial \mathbf{D}}{\partial t} + \mathbf{J} \right) \quad (2)$$

Now by using $\nabla \cdot \nabla \times \mathbf{A} = 0$ it is easy to see eq(1) and eq(2) transform into

$$0 = -\frac{\partial (\nabla \cdot \mathbf{B})}{\partial t} \quad (3)$$

$$0 = \frac{\partial (\nabla \cdot \mathbf{D})}{\partial t} + \nabla \cdot \mathbf{J} \quad (4)$$

Eq (3) implies

$$\nabla \cdot \mathbf{B} = \text{constant wrt time} \quad (5)$$

By using the continuity equation, $\nabla \cdot \mathbf{J} + \dfrac{\partial \rho}{\partial t} = 0,$ eq(4) can be rewritten as

$\dfrac{\partial}{\partial t}[(\nabla \cdot \mathbf{D}) - \rho] = 0$ which implies

$$\nabla \cdot \mathbf{D} - \rho = \text{constant wrt time}. \quad (6)$$

11

Since there will be no sources or currents at t=0, $\nabla \cdot \mathbf{B} = 0$ and $\nabla \cdot \mathbf{D} - \rho = 0$ at initial time. Eq(5) and eq(6) show that these equalities must hold for all time. Since we have just derived the divergence equations from the curl equations, the divergence equations are redundant.

Now, to allow for magnetic loss we will introduce a magnetic current term $\mathbf{M} = \sigma^* \mathbf{H}$, then rearrange the first two equations to produce two differential equations of the form

$$\frac{\partial \mathbf{H}}{\partial t} = -\frac{1}{\mu}(\nabla \times \mathbf{E}) - \frac{\sigma^*}{\mu}\mathbf{H} \quad (7)$$

$$\frac{\partial \mathbf{E}}{\partial t} = \frac{1}{\varepsilon}(\nabla \times \mathbf{H}) - \frac{\sigma}{\varepsilon}\mathbf{E} \quad (8)$$

In taking this step, the μ and ε were removed from within the time derivative. This requires that the permittivity and permeability cannot be functions of time (or frequency). Since in human tissue this is not the case, the analysis will use only one frequency with μ and ε given by a constant. This frequency limitation converts the convolution in the constitutive relations to a multiplication with a scalar, and allows the removal of the permitivity and permeability from within the derivative.

The total E-field can be written as the sum of an incident field and a scattered field. The incident field is defined as propagating through free space everywhere throughout the problem space and the scattered field is defined as propagating through free space outside the scatterer and propagating through the media inside the scatterer. This sum is then be inserted into eq(7) and eq(8) to produce

$$\frac{\partial(\mathbf{H}^i + \mathbf{H}^s)}{\partial t} = -\frac{1}{\mu}\left(\nabla \times (\mathbf{E}^i + \mathbf{E}^s)\right) - \frac{\sigma^*}{\mu}(\mathbf{H}^i + \mathbf{H}^s) \quad (9)$$

and

$$\frac{\partial(\mathbf{E}^i + \mathbf{E}^s)}{\partial t} = \frac{1}{\varepsilon}\left(\nabla \times (\mathbf{H}^i + \mathbf{H}^s)\right) - \frac{\sigma}{\varepsilon}(\mathbf{E}^i + \mathbf{E}^s) \quad (10).$$

Since the incident field is defined in free space it has to obey the equations

$$\nabla \times \mathbf{E}^i = -\mu_o\left(\partial \mathbf{H}^i / \partial t\right) \quad (11)$$

and

12

$$\nabla \times \mathbf{H}^i = \varepsilon_o \left(\partial \mathbf{E}^i \, / \, \partial t \right) \qquad (12).$$

The incident fields are generally known quantities. Therefore, to produce an equation for the scattered field, subtract the value for the incident field from eq(7) and eq(8). At the same time, the corresponding values in eq(11) and eq(12) replace the curl of the incident field. These substitutions produce two equations for the scattered fields of the form

$$\frac{\partial \mathbf{E}^s}{\partial t} = -\frac{\sigma}{\varepsilon} \mathbf{E}^s - \frac{\sigma}{\varepsilon} \mathbf{E}^i - \frac{(\varepsilon - \varepsilon_o)}{\varepsilon} \frac{\partial \mathbf{E}^i}{\partial t} + \frac{1}{\varepsilon} (\nabla \times \mathbf{H}^s) \qquad (13)$$

and

$$\frac{\partial \mathbf{H}^s}{\partial t} = -\frac{\sigma^*}{\mu} \mathbf{H}^s - \frac{\sigma^*}{\mu} \mathbf{H}^i - \frac{(\mu - \mu_o)}{\mu} \frac{\partial \mathbf{H}^i}{\partial t} - \frac{1}{\mu} (\nabla \times \mathbf{E}^s) \qquad (14).$$

These differential equations are then put into finite difference form by implementing the definition of a derivative,

$$\frac{\partial f}{\partial t} \equiv \frac{Lim}{\Delta t \to 0} \frac{f(x, t_2) - f(x. t_1)}{\Delta t} \approx \frac{f(x, t_2) - f(x. t_1)}{\Delta t} \qquad (15)$$

$$\frac{\partial f}{\partial x} \equiv \frac{Lim}{\Delta x \to 0} \frac{f(x_2, t) - f(x_1, t)}{\Delta x} \approx \frac{f(x_2, t) - f(x_1, t)}{\Delta x} \qquad (16)$$

Note that the del operator in eq(13) and eq(14) contains the spatial derivative. After producing these finite difference equations, it is a simple matter of breaking down the equations into x, y, and z components and implementing the finite difference equations on a computer.

Implementing the differential form of the time derivative on eq(9) and eq(10) produces the following difference/derivative equations.

$$\varepsilon \left(\mathbf{E}^{s,n} - \mathbf{E}^{s,n-1} \right) + \sigma \Delta t \mathbf{E}^{s,n} = -\sigma \Delta t \mathbf{E}^{i,n} - (\varepsilon - \varepsilon_o) \Delta t \dot{\mathbf{E}}^{i,n} + \Delta t (\nabla \times \mathbf{H}^{s, n-\frac{1}{2}}) \qquad (17)$$

$$\mu \left(\mathbf{H}^{s,n} - \mathbf{H}^{s,n-1} \right) + \sigma^* \Delta t \mathbf{H}^{s,n} = -\sigma^* \Delta t \mathbf{H}^{i,n} - (\mu - \mu_o) \Delta t \dot{\mathbf{H}}^i - \Delta t (\nabla \times \mathbf{E}^{s+\frac{1}{2}}) \qquad (18)$$

The introduction of the superscript *n* represents the *nth* time. In addition the shorthand notation $\dot{\mathbf{E}}$ represents the derivative with respect to time. The "leapfrog" method of updating the fields is also evident in these equations in the half time step offset of the

electric and magnetic fields. The "leapfrog" technique will be discussed more fully in the discussion of implementing the code.

Solving eq(13) and eq(14) for the scattered fields yields

$$\mathbf{E}^{s,n} = \left(\frac{\varepsilon}{\varepsilon + \sigma \Delta t}\right)\mathbf{E}^{s,n-1} - \left(\frac{\sigma \Delta t}{\varepsilon + \sigma \Delta t}\right)\mathbf{E}^{i,n}$$
$$- \left(\frac{(\varepsilon - \varepsilon_o)\Delta t}{\varepsilon + \sigma \Delta t}\right)\dot{\mathbf{E}}^{i,n} + \left(\frac{\Delta t}{\varepsilon + \sigma \Delta t}\right)(\nabla \times \mathbf{H}^{s,n-\frac{1}{2}}) \qquad (19)$$

$$\mathbf{H}^{s,n} = \left(\frac{\mu}{\mu + \sigma^* \Delta t}\right)\mathbf{H}^{s,n-1} - \left(\frac{\sigma^* \Delta t}{\mu + \sigma^* \Delta t}\right)\mathbf{H}^{i,n}$$
$$- \left(\frac{(\mu - \mu_o)\Delta t}{\mu + \sigma^* \Delta t}\right)\dot{\mathbf{H}}^{i} - \left(\frac{\Delta t}{\mu + \sigma^* \Delta t}\right)(\nabla \times \mathbf{E}^{s+\frac{1}{2}}) \qquad (20).$$

A computer code then solves these equations across time and space to predict electromagnetic interactions with scattering objects. The methodology section of this thesis discusses implementation of these equations in complete detail.

Before implementation of FDTD, the cell size and time step size have to be determined. In general, the cell size determines the accuracy. The cells have to be at least one tenth of the shortest wavelength within the materials. The smaller the cell size, the more accurate the results will be. If the scattering object has ramped or spherical surfaces, a quantization error will result. This error is commonly referred to as the "staircase" error. Smaller cells can reduce this error by producing a more accurate rendering of the actual geometry. Reducing the cell size has its drawbacks, however. Reduction of the cell size requires subsequent reduction of the time step size. With smaller time step increments, the code must cycle through more time steps to allow for the same amount of time and the same field propagation distance.

The cell size determines the size of the time step to ensure stability in the solution. The FDTD simulation can only propagate the field across one cell in each time step. Too long of a time step forces the FDTD simulation to propagate the field across multiple cells in one time step, which it is unable to do. Thus, the solution becomes unstable. In order

14

to determine what the optimal time step is, we turn to the Courant stability condition [9] which states that for a propagation speed v within the material, the time step must be chosen to satisfy the condition,

$$v\Delta t \leq \left(\frac{1}{(\Delta x)^2} + \frac{1}{(\Delta y)^2} + \frac{1}{(\Delta z)^2} \right)^{-\frac{1}{2}} \quad (21).$$

This condition specifies the longest time step that will maintain stability. The use of shorter time steps is possible, but show little improvement and are not worth the added computation time [9].

From this equation it can be seen that to ensure stability, the time step size must be reduced when the cell size is reduced. In addition, raising the frequency forces reduction of the cell size due to the shortening of the wavelengths; thus, reduction of the time step is necessary. To produce the best results in the shortest time, it is necessary to weigh the accuracy desired at a given frequency against the computation time necessary to set up the optimal simulation configuration. The methodology section describes the simulation configuration which this research uses.

3.2 Source Optimization

The source optimization developed by Rappaport and Morgenthaler uses the solution to the vector wave equation in spherical coordinates. Appendix A gives a complete derivation of this solution. The solution is [10]

$$\mathbf{E}(R,\theta,\phi) = \left(\frac{1}{k} \frac{\partial^2 \left(Rf_{e_{mn}} \right)}{\partial R^2} + k^2 R\psi \right)\hat{r} + \left(\frac{1}{kR} \frac{\partial^2 \left(Rf_{e_{mn}} \right)}{\partial R \partial \theta} \right)\hat{\theta} + \left(\frac{1}{kR\sin\theta} \frac{\partial^2 \left(Rf_{e_{mn}} \right)}{\partial R \partial \phi} \right)\hat{\phi} \quad (22)$$

Where

$$f_{e_{mn}} = j_n(kR)P_n^m(\cos\theta)\frac{\cos}{\sin}m\phi. \quad (23)\ [10]$$

15

Before going further, it is important to note a few of the dependencies within this equation. The spherical Bessel function of order n predominately controls the radial dependence. The m and n modes of the Legendre function dictate the theta dependence. Finally, the ϕ dependence varies as $\sin m\phi$. Figure 3.1 describes the location of all of these components
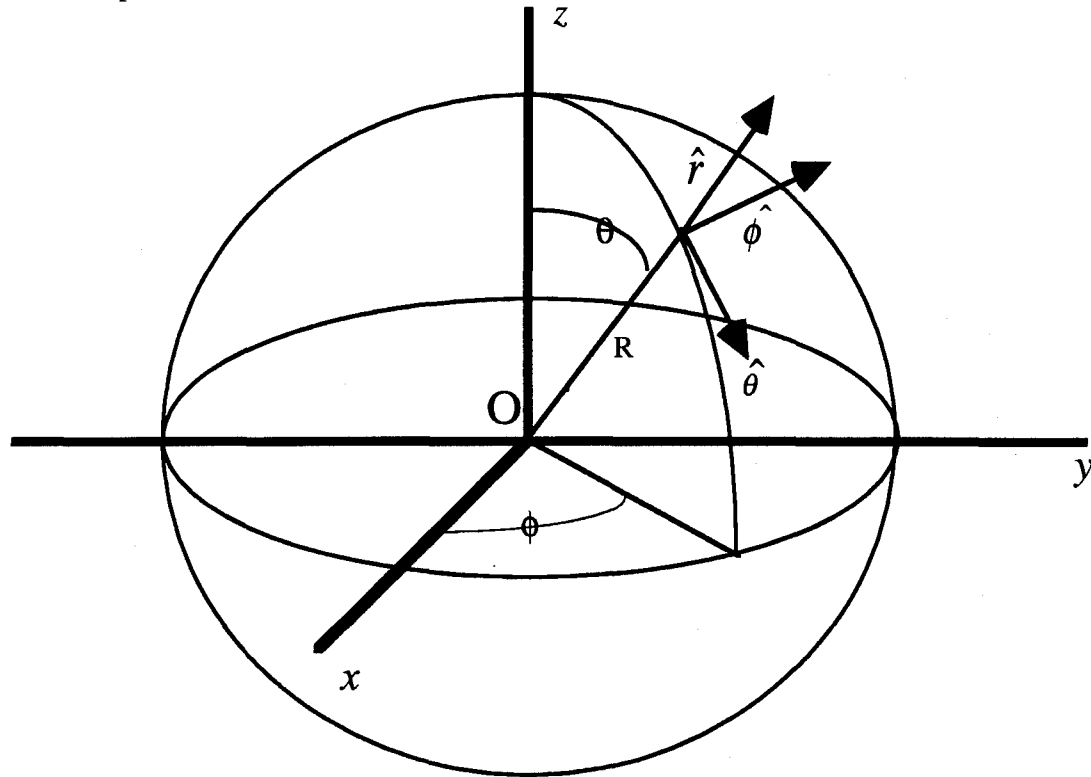
Figure 3.1: The Spherical coordinate system as used in this thesis

Rappaport and Morgenthaler began at eq (22) to find the optimal source distribution. The following description of this optimization comes from [1]. Solving eq(22) for the derivatives and using only the m=0 modes produces

$$\mathbf{E}(\mathbf{R}) = \sum_{n=1}^{N} \hat{r} A_n \frac{n(n+1)}{kR} j_n(kR) P_n(\cos\theta)$$

$$+ \hat{\theta} A_n \left[j_{n-1}(kR) - \frac{n}{kR} j_n(kR) \right]$$

$$* \left[n\cos\theta P_n(\cos\theta) - nP_{n-1}(\cos\theta) \right] \left(\frac{1}{\sin\theta} \right) \qquad . \quad (24)$$

Figure 3.2 shows a plot of the power across a vertical cut through the sphere. This is a plot of the power with only the first mode excited. It is clear from this plot that the power is concentrated near the equator. Increasing the power near the poles will allow reduction of the power near the equator, without reducing the power at the focus. In other words, the power at the equator needs to be spread out toward the poles.

Using only the m=0 modes spreads the field as evenly around the sphere as possible. Higher order m modes would force a sinusoidal variation in the Phi direction. This variation would produce nulls at evenly placed intervals, depending on the value of m. These nulls would, in turn, force higher power at the peak areas on the surface to get the same amount of power to the center due to the absence of power at the nulls. Thus, unless there was for some reason a location where the E-field had to be kept at zero, it would be counterproductive to use higher order m modes.

The higher n modes, however, can be used to our advantage. Because $j_n(kR)$ varies as $(kR)^n$ for small values of R, the n=1 mode is the only mode that has power at r=0, all other modes are zero at the center. Figure 3.3 shows this characteristic of higher order n modes. It is a plot of the first three n modes peak E-field value versus radius, where R=0 is the center of the sphere and increasing R goes out along an equatorial cut of the sphere. Therefore, addition of higher order n modes out of phase with the first mode, will allow their use to reduce the power on the surface without affecting the power at the center.

17
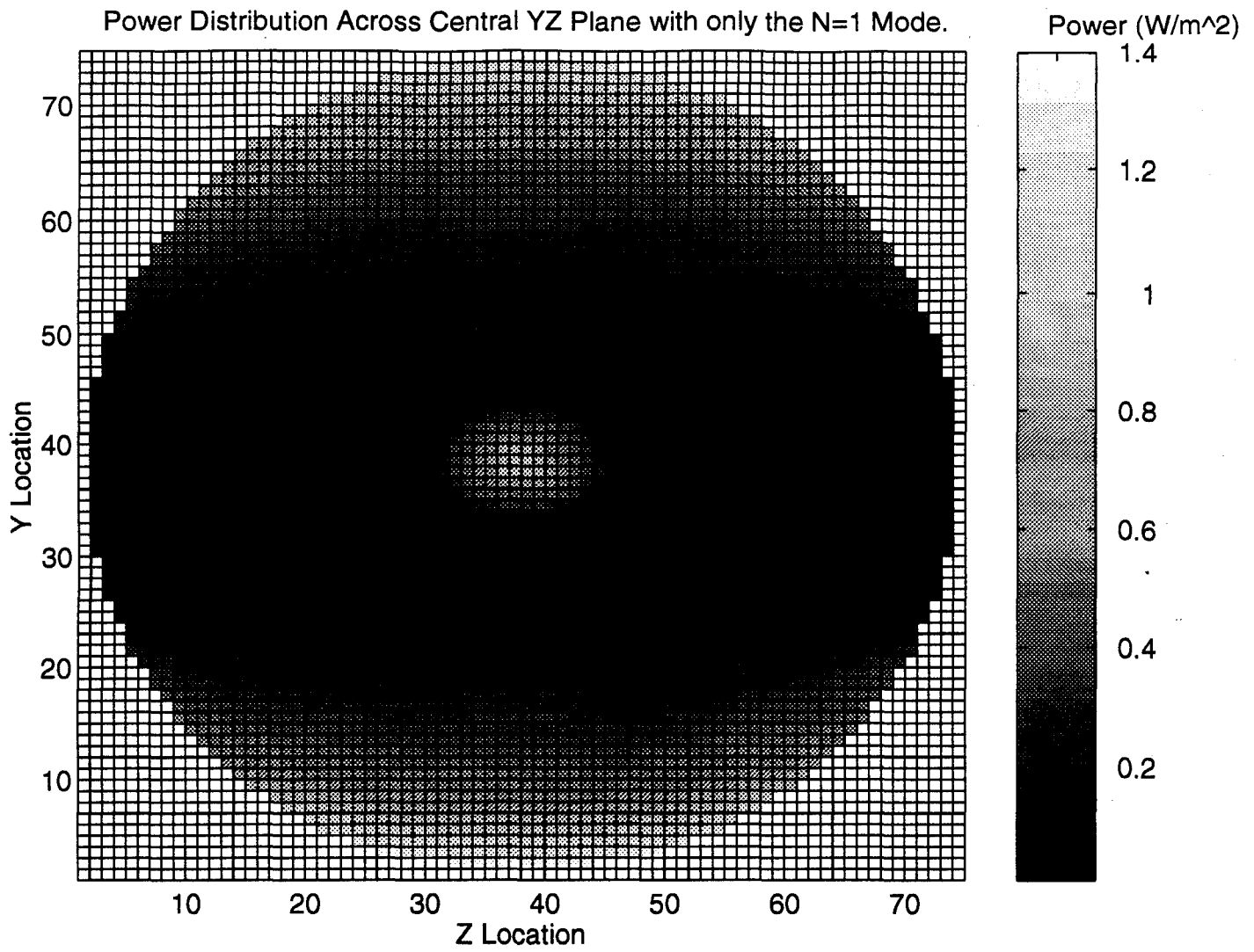
Figure 3.2: Plot of the power distribution across the central YZ cut with only the N=1 mode excited.
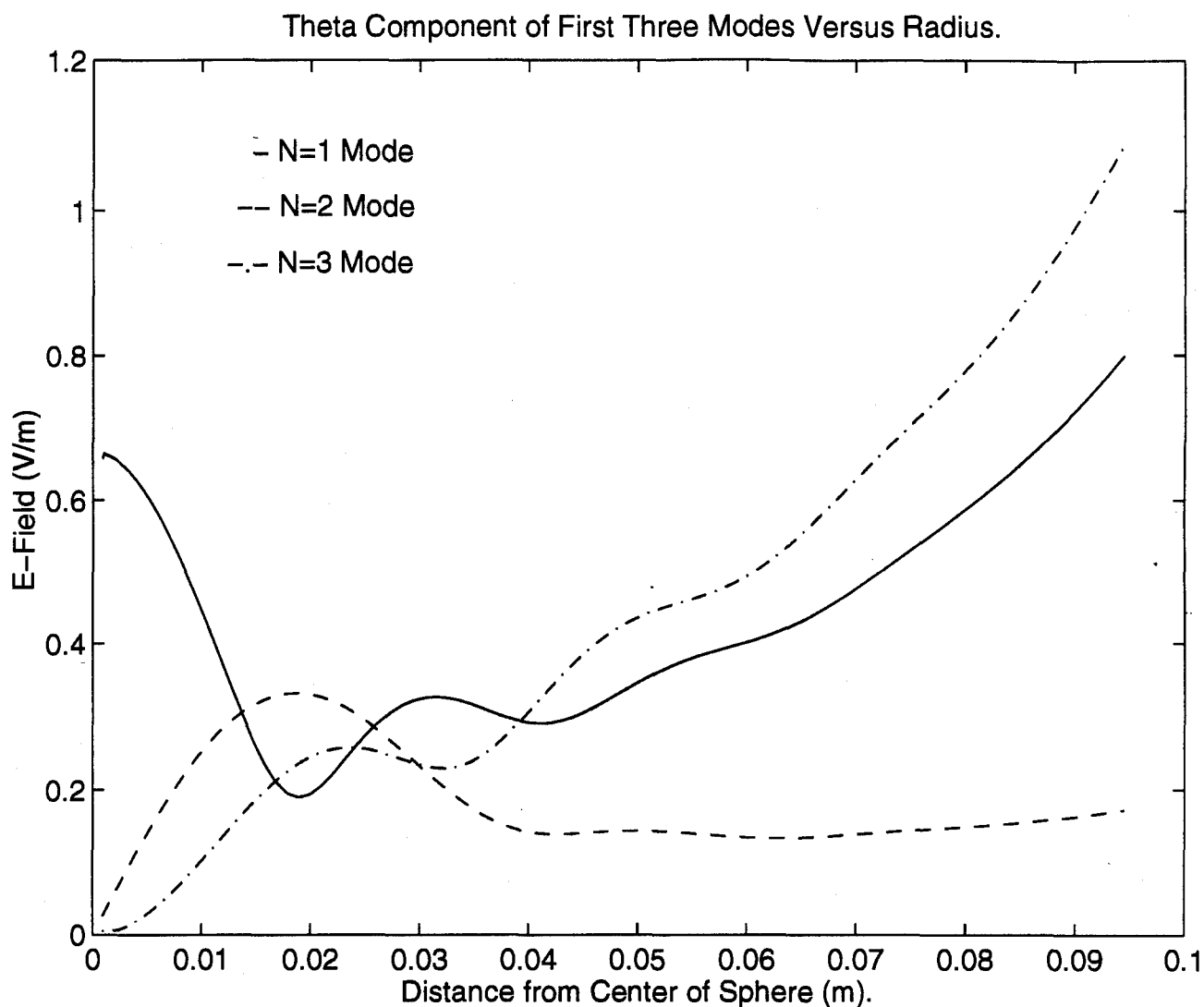
Figure 3.3: Peak E-field strength versus radius for the first three n modes. R=0 represents the center of the sphere.

However, optimization does not require the use of the even n modes. This can be seen from looking at the instantaneous E-field values along the surface of the sphere. For large radii, the $\frac{1}{kR}$ dependence reduces the $\hat{r}$ component and the $\hat{\theta}$ component becomes the dominating factor. Therefore, to reduce the power levels at the surface (large R) the $\hat{\theta}$ component is the component most important to reduce. Since we are dealing only with the m=0 mode, there is no $\hat{\theta}$ dependence in the ϕ direction, see eq(22). Therefore, the optimization must deal with the $\hat{\theta}$ dependence in the θ direction.
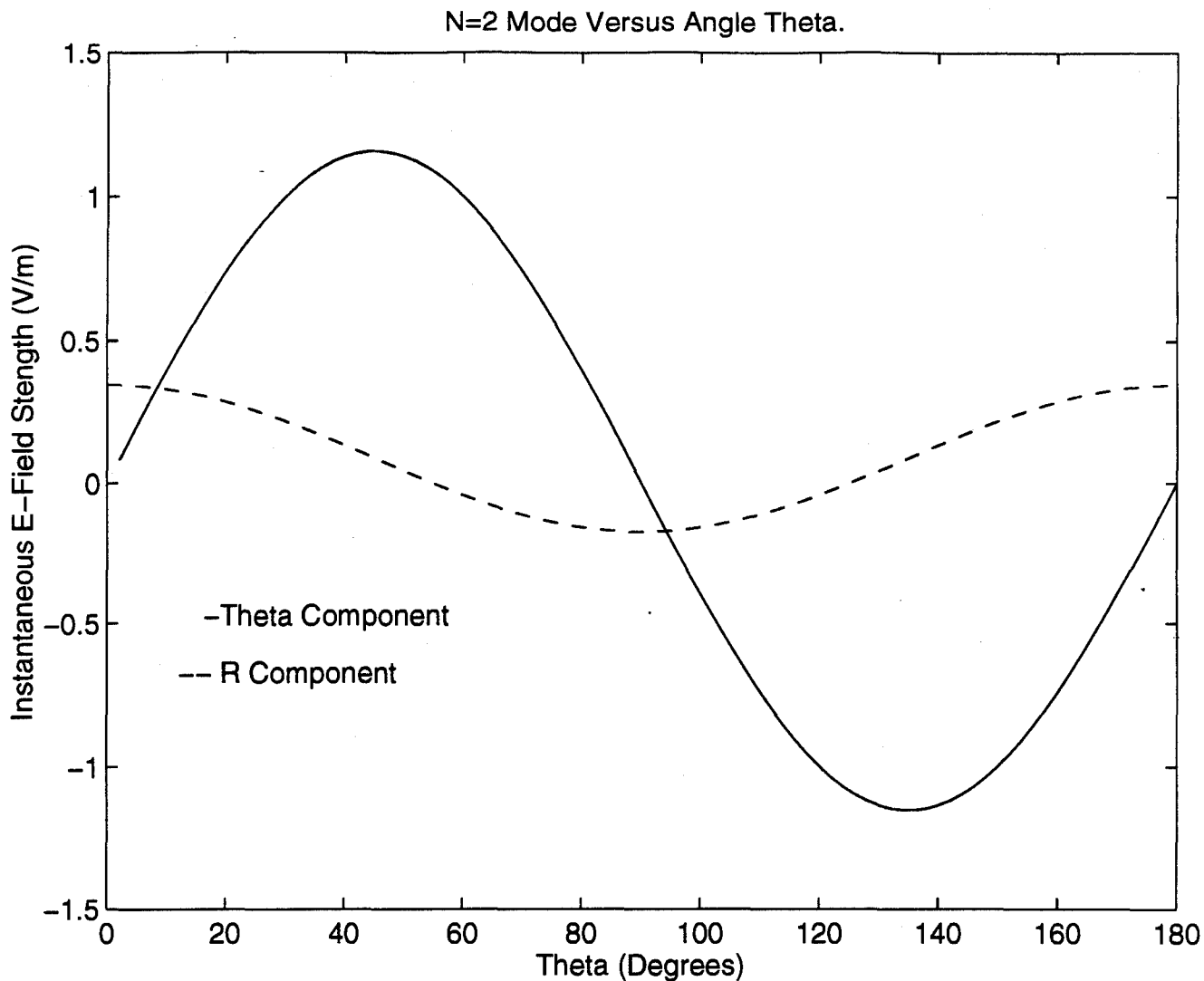
Figure 3.4: This figure is a plot of the instantaneous E-field versus angle theta for the n=2 mode at R=9.45 cm (along the surface of the sphere).

Eq(19) shows the $\hat{\theta}$ dependence to be

$$E_{\theta n} \sim \frac{dP_n(\cos\theta)}{d\theta} . \quad (25)$$

$P_n(\cos\theta)$ is an even function of θ for even values of n; therefore, its derivative will be an odd function of θ and will have a null at $\theta = \frac{\pi}{2}$. Figure 3.4 demonstrates this in a plot of the instantaneous $\hat{\theta}$ component of the E-field for the n=2 mode at a radius of 9.45 cm (the surface of the sphere). Since these even order modes have a null at the equator, where we hope to reduce the power level, they will be of no help in optimization. In addition, since

20
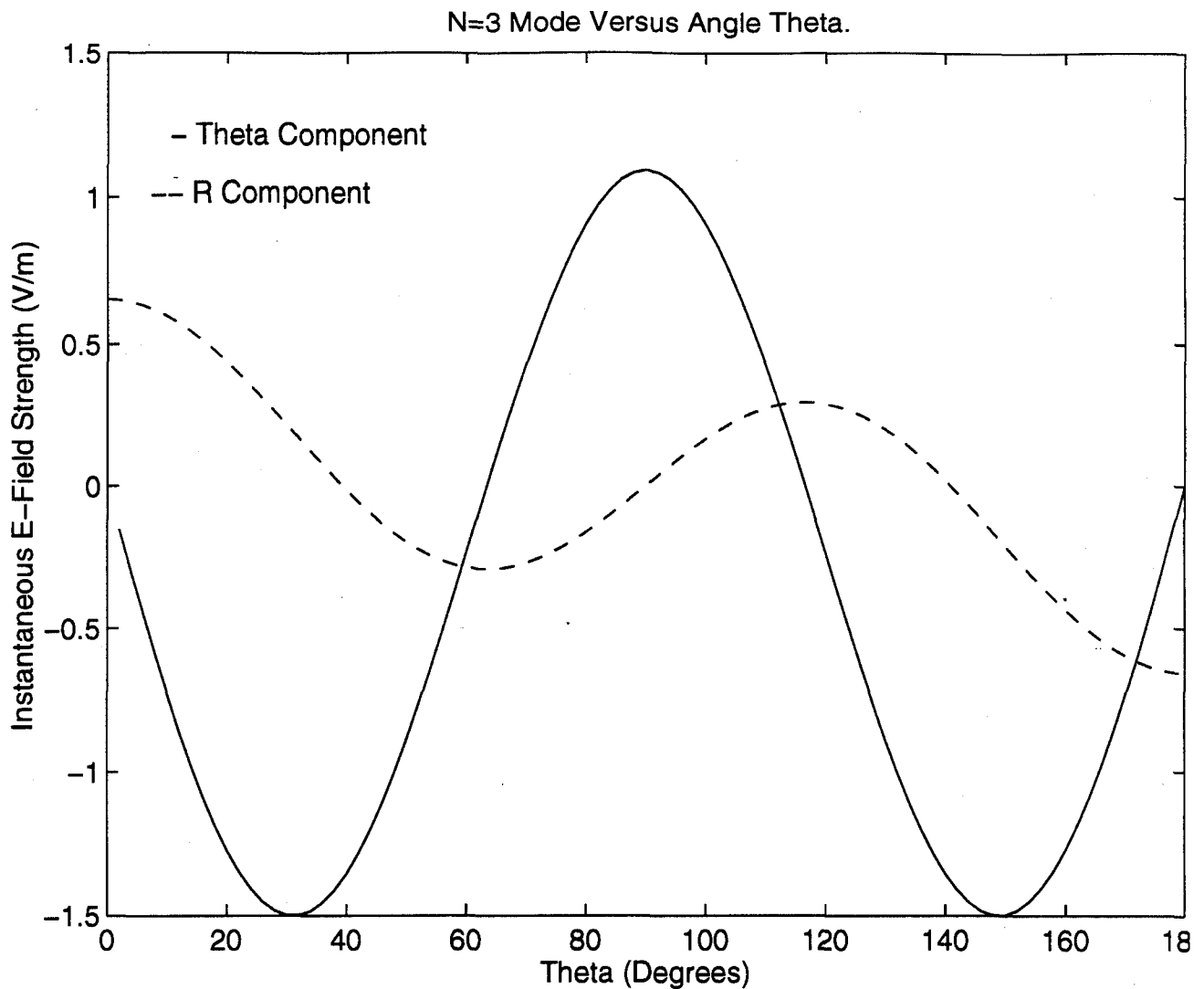
Figure 3.5: This is a plot of the instantaneous E-field versus angle theta for n=3 mode at R=9.45 cm.

they are odd functions, when the fields subtract in the lower hemisphere they will add in

the upper and vice-versa.

The Legendre functions of odd order n, however are odd functions of θ.

Therefore, their derivatives are even functions of theta and will have a peak at $\theta = \frac{\pi}{2}$.

Figure 3.5 illustrates this idea in a plot of the instantaneous E-field for the n=3 mode versus

angle theta along the surface of the sphere. From this plot it can be seen how the odd order

21

n modes can be used to reduce the power near the equator. It is the same idea as Fourier analysis of periodic time signals to produce a pulse, only it is using spatial harmonics rather than time harmonics. The reasons given above demonstrate the optimization should deal solely with the odd order harmonics of index n. It is interesting that because the $\hat{r}$ dependence varies with $P_n(\cos\theta)$, its even order harmonics would be preferential for optimization, but because they are less dominate, we deal only with the $\hat{\theta}$ component.

The optimization plan was to add these first three odd order harmonics in such a way to reduce the power at the equator as much as possible. To do this, start at the θ dependence of the derivative of the Legendre function for n=1,3 and 5.

$$E_{\theta 1} \sim -\sin\theta$$
$$E_{\theta 3} \sim -\frac{15}{2}\cos^2\theta\sin\theta + \frac{3}{2}\sin\theta \qquad (26)$$
$$E_{\theta 5} \sim -\frac{315}{8}\cos^4\theta\cos\theta + \frac{105}{4}\cos^2\theta\sin\theta - \frac{15}{8}\sin\theta$$

Using trigonometric identities, rewrite these equations in terms of odd multiples of θ.

$$E_{\theta 1} \sim -\sin\theta$$
$$E_{\theta 3} \sim -\frac{15}{8}\sin 3\theta + \frac{3}{8}\sin\theta \qquad (27)$$
$$E_{\theta 5} \sim -\frac{315}{128}\sin 5\theta - \frac{105}{128}\sin 3\theta - \frac{30}{128}\sin\theta$$

It is now possible to rewrite the three equations (27) into one equation describing the θ dependence as

$$f(\theta) = \sin\theta + B_1\sin 3\theta + B_2\sin 5\theta \qquad (28)$$

Next, solve this equation for the B coefficients to minimize the maximum value of $(f(\theta))^2$ from 0 to π. This produces coefficients of value $B_1 = .2365$ and $B_2 = .0640$. The resulting form of the equation has three peaks at the maximum value .685 of the previous maximum. Figure 3.6 shows a plot of the equation for the first three odd harmonics as well as for the first harmonic alone.
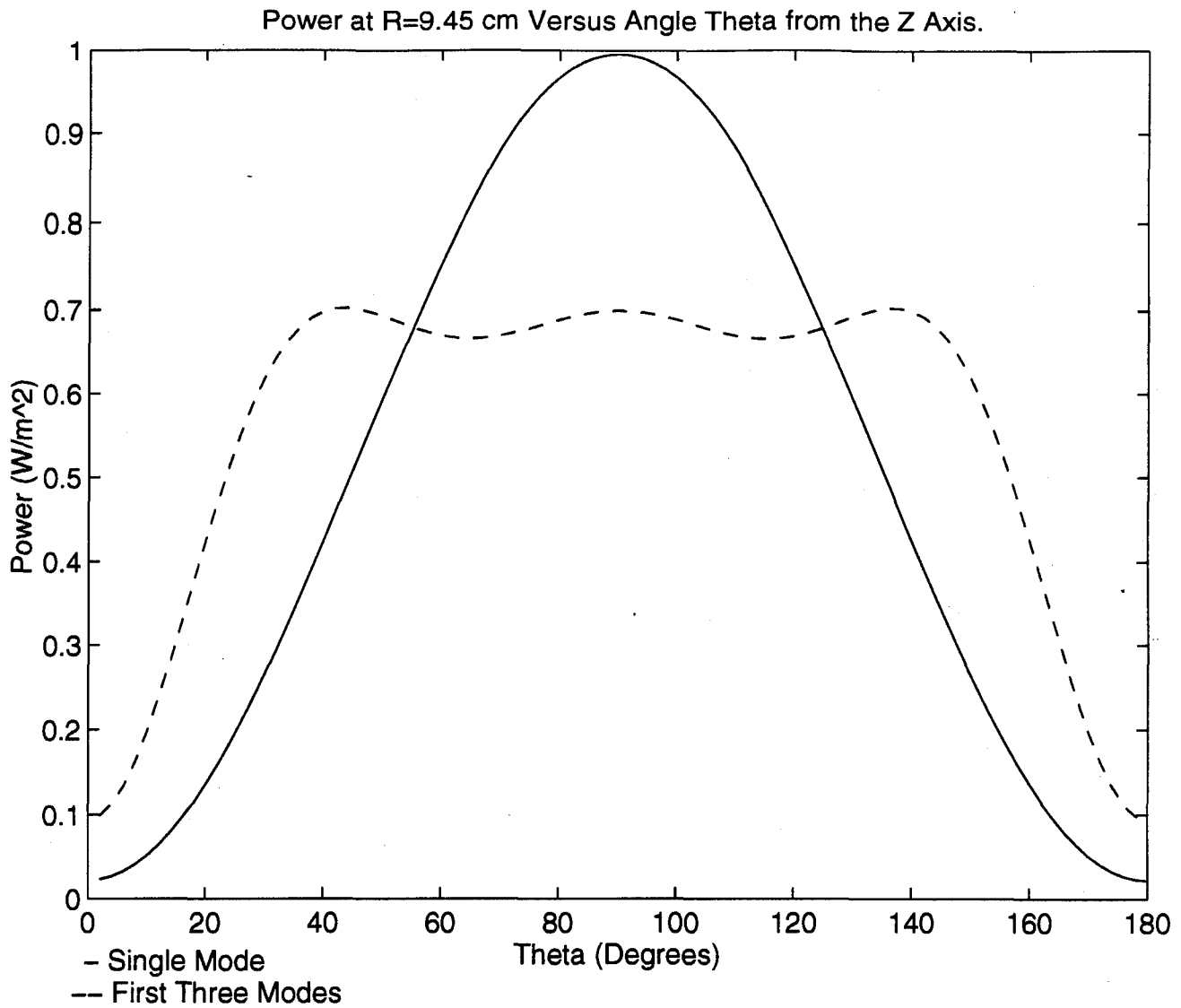
Figure 3.6: This figure is a plot of $(f(\theta))^2$ for the first three odd modes compared to the plot of only the first mode.

From here it can be seen how this could be extended out in terms of SIN's of higher multiples of θ to reduce the ripple further. However, because there is a great deal of error inherent in determining the material characteristics of the head, this decreased ripple will not not be worth the extra time required for analysis.

The next step is to add in the spherical Bessel function scaling factors on each mode. This is done by introducing the coefficients $J_n = A_n \left[j_{n-1}(kR) - \dfrac{n}{kR} j_n(kR) \right]$.

Combining this definition with the B coefficients, eq (28) for $f(\theta)$, and the three equations (27) produces a system of equations for the J coefficients of the form

$$J_1(-1) + J_3\left(-\frac{3}{8}\right) + J_5\left(-\frac{30}{128}\right) = 1$$

$$J_3\left(-\frac{15}{8}\right) + J_5\left(-\frac{105}{128}\right) = 0.2365 . \qquad (29)$$

$$J_5\left(-\frac{315}{128}\right) = 0.0640$$

The solution for this system is $J_1 = -0.9509$, $J_3 = -0.1148$, and $J_5 = -0.0260$.

The first J coefficient is reduced from unity due to the $\sin\theta$ terms in the higher order modes. Thus, the power at the center of the sphere is reduced by the same amount (the higher order modes due not contribute to the power at the center). Division of these three coefficients by -0.9509 produces a J_1' coefficient equal to unity and $J_3' = 0.1207$, and $J_5' = 0.0288$. Thus, the power at the surface will be 72% the value of a single mode excitation.

From here the optimization changes based on the characteristics of the material and the frequency used. This research uses a frequency of 915 MHz which corresponds to a relative permittivity in muscle tissue equal to 51 and a conductivity of 1.26. These values are used to solve for the value of k and substituted back into the definition of the J coefficients to find values for the A coefficients. In solving for the optimal value of the A coefficients, the equations change for each choice of radius R, thus the optimization is an iterative process. When these iterations are complete, the optimal A coefficients for a homogeneous sphere of muscle tissue are found to be A1=1.21 + 0.89j, A3=-.19 - 0.05i, and A5=.05 - .02i.

4. Methodology

This research entails setting up three distinct simulations. The first is an analytic simulation that serves as a comparison for the FDTD results to validate the FDTD code. For this simulation, a FORTRAN program solves the spherical vector wave equation on a homogeneous sphere of muscle tissue. A series of FDTD simulations on laminated spheres comprise the second set of simulation. This set provides insight into the effects of inhomogeneities on the propagation of the ideal source radiation. A series of FDTD simulations on an actual model of a human head developed from an MRI scan at Penn State comprise the final set of simulations.

4.1 Spherical Vector Wave Equation Computer Code

The first step entails duplicating Rappaport's analytic results to use as a control with which to compare FDTD solutions. A FORTRAN code solves Rappaport's optimized solution in a space that has the same grid size as the proposed FDTD space. Solving this equation across a grid identical to the one used in the FDTD simulation allows easy comparison. Figure 4.1 shows the flow diagram of the code.
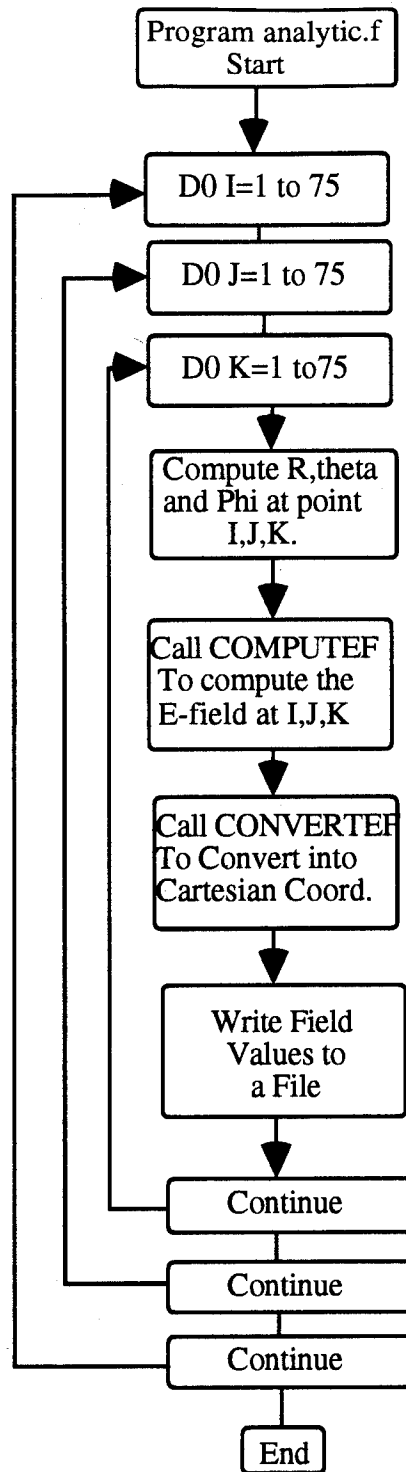
Figure 4.1: This figure shows the flow diagram of the FORTRAN code to compute the analytic solution to spherical vector wave equation.

The main body of the code steps through x, y, and z increments each running from one to seventy-five. As in the FDTD grid that will be used, each 'cell' is cubic with a length of .002554 m. As the code steps through each cube in the grid, it computes the angle θ down from the z axis and the angle φ off the x axis, as well as the distance, R, from the center of the cube of interest to the center of the sphere, that is located at x=37.5, y=37.5, and z=38. The code then calls the subroutine COMPUTEEF which computes the R and θ directed components of the E-field (recall that there is no φ component). It then calls the subroutine CONVERTEF to transform these components into x, y, and z directed components for comparison to the FDTD results that are in Cartesian, not polar coordinates. The program then writes out the value of the E-field to a data file for Matlab to read.

This field distribution is assumed to be throughout a muscle-filled space; therefore, the field grows everywhere outside the sphere of muscle tissue. The FDTD code defines the E-Field source distribution at Rappaport's maximum 9.45 cm radius. Defining this surface around the sphere electrically isolates the inside and outside. In this manner, the inside of the sphere should contain the same distribution as the analytical solution within the 9.45 cm radius. Outside this radius of interest, the fields will be drastically different, thus all analysis ignores this region.

This field distribution is then compared with the FDTD solutions of the same sphere geometry. This provides an analysis to test the validity of the FDTD code and its modifications. This simulation provides a simple duplication of Rapport's work.

4.2 FDTD Computer Code

The code for producing the analytic solution is used to specify the incident field in the FDTD space. This code sets up an electric 'shell' around the sphere by setting the E-field values at every cube along the 9.45 cm radius. This distribution then radiates, and the field propagates through the FDTD grid and produces the same results as the analytic

27

version. This simulation validated the use of FDTD in this way to simulate a constant E-field around a sphere.

4.2.1 FDTD Geometry Implementation

Before discussing the implementation of the equations, it is important to discuss the definition of geometries in FDTD and the layout of the Yee cell [9]. An understanding of this geometry is essential to understand the FDTD equations.

The design of the Yee cell offsets the magnetic and the electric fields by one half a cell size. Along with being offset by a half step in space, the code also updates the E and H fields a half time step apart. Figure 4.2 shows the geometry of the Yee cell. The cell shows the location of each of the E and H field components. The user creates a geometry by assigning a material ID number to each field component location that defines its electrical characteristics.
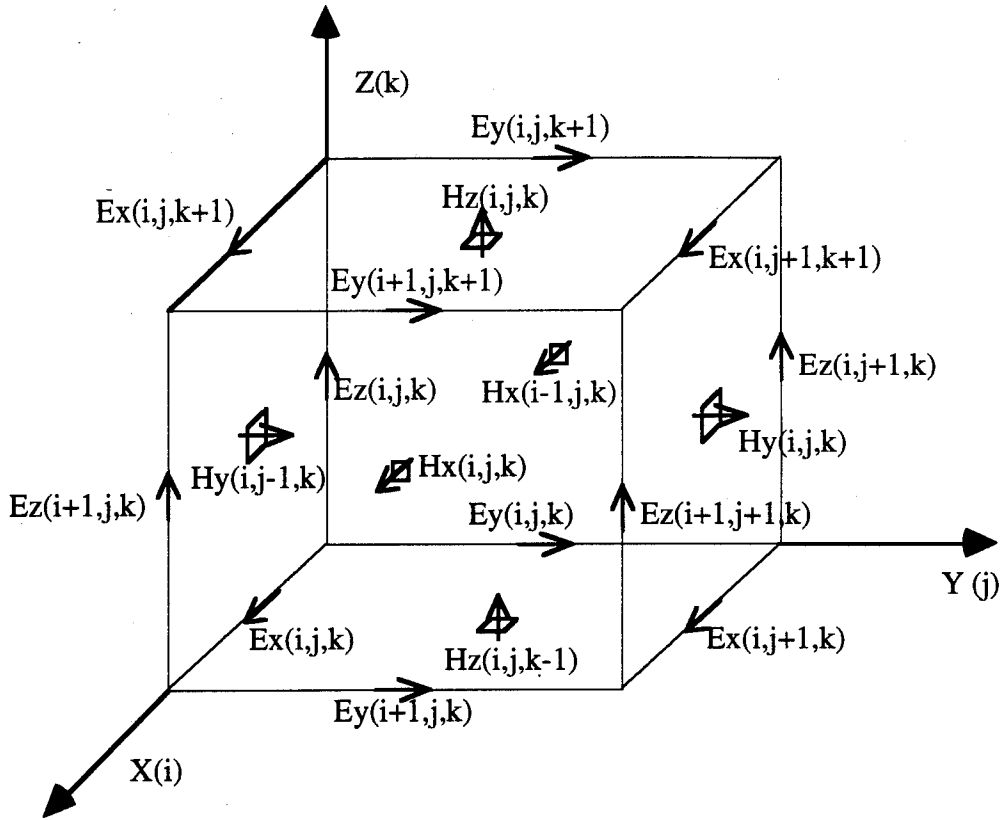
Figure 4.2: This figure shows the geometry of the Yee Cell [9].

The user builds FDTD structure by assigning a material ID number to each position. These numbers run from 0 to the number of materials in the space. Zero specifies free space, 1 specifies perfect electric conductors (PEC) and numbers two and up have a corresponding permeability, permittivity, conductivity and magnetic conductivity stored in a matrix. This building process defines six matrices containing an ID number corresponding the material at each position. The matrix IDONE contains the material ID number for each of the X directed components in the FDTD space; likewise, IDTWO and IDTHRE correspond to the material ID number at the Y and Z locations respectively. IDFOUR, IDFIVE, and IDSIX contain the ID numbers for the materials located at the X,

Y, and Z components of the magnetic grid in the FDTD space. These six matrixes define the objects in the FDTD space [9].

4.2.2 FDTD Implementation in FORTRAN

Implementing FDTD in a computer code involves solving eq(15) and eq(16) over time and space. This can take an immense amount of time if the problem space is large or the frequency high. Therefore, it is important to implement the code in the most efficient manner possible.

The first step in doing this is to note that the code does not have to recalculate the multipliers before each field component for every cell at every time step [9]. Since most problems will have a small number of different scattering materials, the program calculates and stores these multipliers away ahead of time in a matrix. To do this, define the following FORTRAN equalities [9]:

$$ECRLY(M) = \frac{DT}{(EPS(M) + SIGMA(M) * DT) * DY} = \frac{\Delta t}{(\varepsilon + \sigma \Delta t)\Delta Y}$$

$$ECRLZ(M) = \frac{DT}{(EPS(M) + SIGMA(M) * DT) * DZ} = \frac{\Delta t}{(\varepsilon + \sigma \Delta t)\Delta Z}$$

$$ESCTC(M) = \frac{EPS(M)}{(EPS(M) + SIGMA(M) * DT)} = \frac{\varepsilon}{\varepsilon + \sigma \Delta t}$$

$$EINCC(M) = \frac{SIGMA(M) * DT}{(EPS(M) + SIGMA(M) * DT)} = \frac{\sigma \Delta t}{\varepsilon + \sigma \Delta t}$$

$$EDEVCN(M) = \frac{DT * (EPS(M) - EPSO)}{(EPS(M) + SIGMA(M) * DT)} = \frac{(\varepsilon - \varepsilon_o)\Delta t}{\varepsilon + \sigma \Delta t}$$

Where M is an index representing the different material types present in the problem space. Defining and solving these equations ahead of time reduces the computation time considerably. These numbers are then input into eq (19) page 14 to produce a form suitable for FORTRAN code [9].

$$
\begin{aligned}
EXS(I,J,K) = \ &EXS(I,J,K) * ESCTC(IDONE(I,J,K)) \\
&-EINCC(IDONE(I,J,K)) * EXI(I,J,K) \\
&-EDEVCN(IDONE(I,J,K)) * DEXI(I,J,K) \quad\quad (6)\\
&+(HZS(I,J,K) - HZS(I,J-1,K)) * ECRLY(IDONE(I,J,K)) \\
&-(HYS(I,J,K) - HYS(I,J,K-1)) * ECRLZ(IDONE(I,J,K))
\end{aligned}
$$

Similar equations are also formulated for the Y and Z components of the electric field as well as for the X, Y, and Z components of the magnetic field.
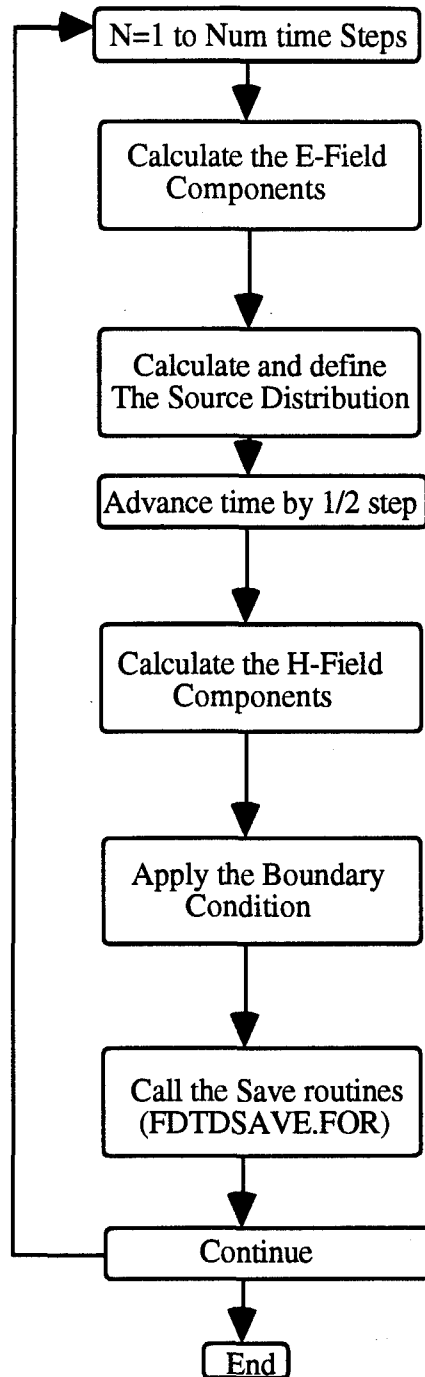
Figure 4.3: This figure shows a flow diagram of the FDTD code.

To solve for the field over time, the code runs through the time steps, recalculating these equations for every component. For each of these loops, the code first runs through all the X, Y and Z locations of the electric grid. For each location in the FDTD space, the X, Y and Z components of the electric field are updated using the corresponding equation similar to eq (6). The program then calls the FEED subroutine that forces the field at the feed locations to be equal to the specified source wave form. The time is then incremented by half a time step and the X, Y and Z components of the magnetic grid are updated using the corresponding magnetic equations similar to eq (6). The program then increments time by another half step and the process repeated. Figure 4.3 shows a flow diagram of this process.

4.2.3 Code Modifications

Two major modifications had to be made on the Penn State code. First, the FEED subroutine had to be changed. The design of the code is for use in antenna calculations; thus, it is set up to have a small number of feeds, one for each antenna. Forcing an E-field around the surface requires around 50,000 feeds. Specifying each one individually proves to be both time consuming and memory intensive. To avoid this pitfall, the FEED subroutine is modified to calculate each value using the analytic field equations. Figure 4.4 and figure 4.5 show flow diagrams of two modifications of the subroutine .

The first modification cycles through the FDTD space and determines if each point is along the surface of the sphere. When it comes across a point on the surface, it calls the COMPUTEEF subroutine from the analytic program. This computes the amplitude and phase for the R and THETA components of the E-field. It then uses a simple conversion routine to convert into x, y and z directed field components and forces the E-field at the location to have the desired value. The Yee cell geometry places each field component in a slightly different location. The first modification computes the location of each component and then figures the analytic value of the field individually for each component. This

32

requires computing 6 values for every cube. This subroutine repeats every time step, so increasing its speed can significantly increase computing time.
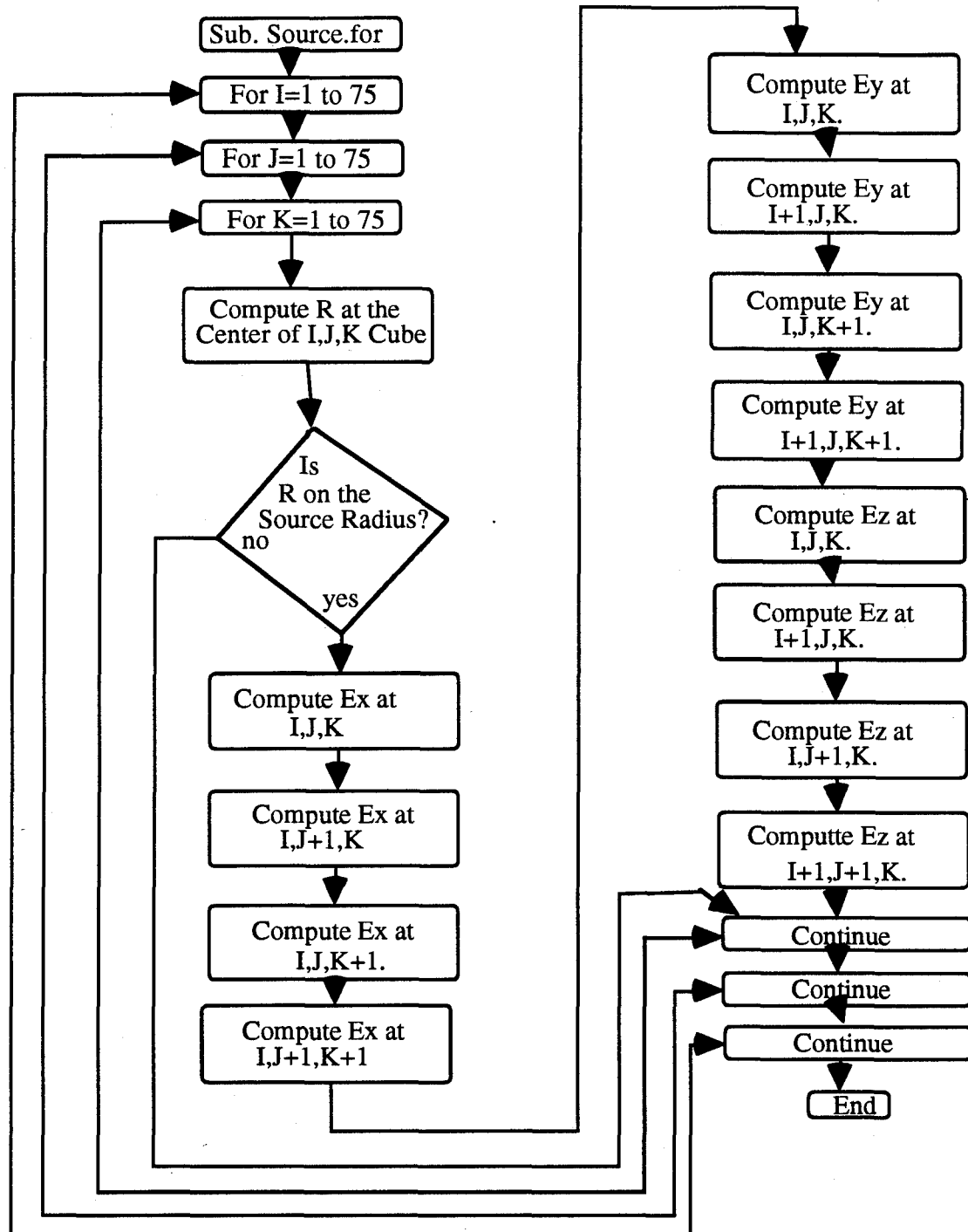
Figure 4.4: Flowchart of FEED subroutine that defines the exact source distribution.

```
┌─────────────────┐
│ Sub. Source.for │
└─────────────────┘
         │
         ▼
  ┌──────────────┐
  │ For I=1 to 75│
  └──────────────┘
         │
         ▼
  ┌──────────────┐
  │ For J=1 to 75│
  └──────────────┘
         │
         ▼
  ┌──────────────┐
  │ For K=1 to 75│
  └──────────────┘
         │
         ▼
  ┌──────────────────┐
  │ Compute R at the │
  │ Center of I,J,K Cube│
  └──────────────────┘
         │
         ▼
       ╱╲
      ╱  ╲
     ╱ Is ╲
    ╱ R on the╲
    ╲ Source Radius?╱
   no╲        ╱
      ╲  yes ╲
       ╲╱
         │ yes
         ▼
  ┌──────────────────┐
  │Compute E field at the│
  │center of cube I,J,K │
  └──────────────────┘
         │
         ▼
  ┌──────────────────┐
  │ Assign values for│
  │ each of the twelve│
  │ source components│
  │ on the cube.     │
  └──────────────────┘
         │
         ▼
  ┌──────────────┐
  │   Continue   │
  └──────────────┘
         │
         ▼
  ┌──────────────┐
  │   Continue   │
  └──────────────┘
         │
         ▼
  ┌──────────────┐
  │   Continue   │
  └──────────────┘
         │
         ▼
     ┌──────┐
     │ End  │
     └──────┘
```
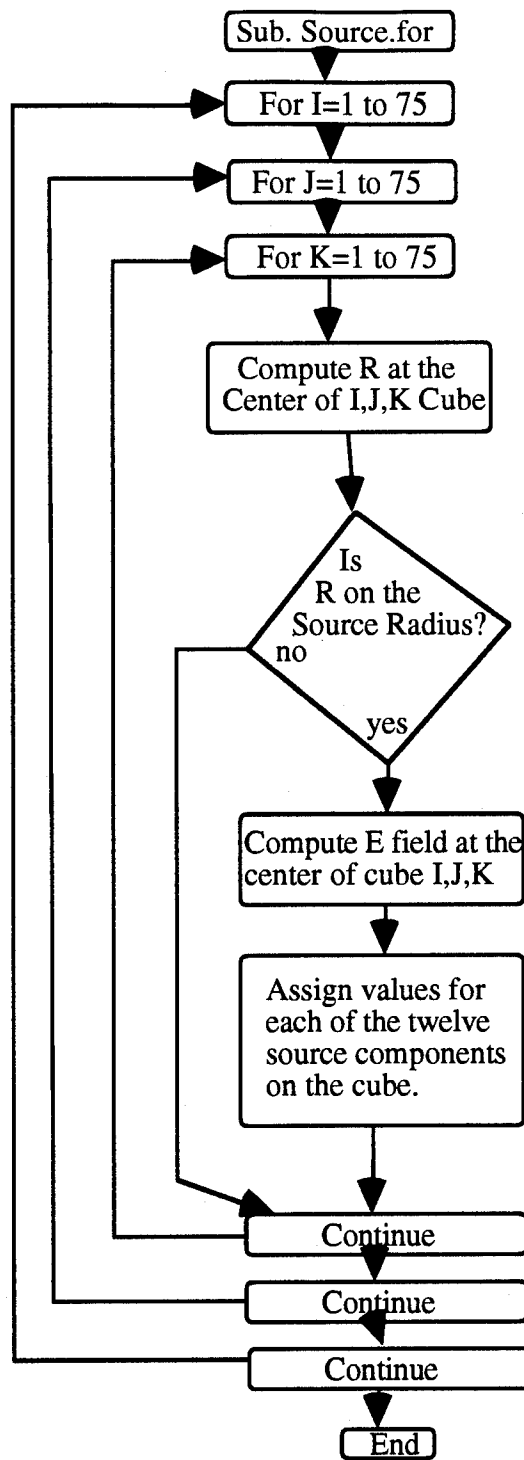
Figure 4.5: Flowchart of FEED subroutine that defines an approximate source distribution based on the E-field at the center of each cube.

To reduce the computational time at each time step, the second modification approximates the source. This code does not compute a different value for each component. Instead, the code computes the analytical value the components would have at the center of the cube and gives all six components their value based on this result. A further modification to decrease computation time would be to cycle through theta and phi at the radius 9.45 cm rather than cycling through all space thereby reducing the cycle length.

The second major modification is the addition of a peak E-field storage array. This allows the user to specify an area over which the peak E-field value will be recorded. Figure 4.6 shows the code of the implementation of this in the DATSAV subroutine.

```
C       WRITES OUT MAX VALUES FOR A BLOCK DEFINED BY TWO POINTS
C       (ONLY USEFUL FOR SINGLE FREQUENCY RUNS)

        ELSE IF (NTYPE(NPT).EQ.19) THEN
        IF (N.GT.(.9*NSTOP)) THEN
        REWIND(50+NPT)
         DO 246 I=IOBS(NPT),IOBSE(NPT)
          DO 247 J=JOBS(NPT),JOBSE(NPT)
             DO 248 K=KOBS(NPT),KOBSE(NPT)
               EX=ABS(EXS(I,J,K)+FINC(I,J,K,4))
               EY=ABS(EYS(I,J,K)+FINC(I,J,K,5))
               EZ=ABS(EZS(I,J,K)+FINC(I,J,K,6))
             IF (EX.GT.EXM(I,J,K)) EXM(I,J,K)=EX
             IF (EY.GT.EYM(I,J,K)) EYM(I,J,K)=EY
             IF (EZ.GT.EZM(I,J,K)) EZM(I,J,K)=EZ
             WRITE((50+NPT),*) EXM(I,J,K),EYM(I,J,K),EZM(I,J,K)
248        CONTINUE
247      CONTINUE
246    CONTINUE

        ENDIF
```

Figure 4.6: The Code of the DATSAV modification.

This is only useful because the FDTD simulations are using one electromagnetic frequency. By recording the peak value of the E-field, the power deposited can be easily calculated using $P = \frac{|\mathbf{E}|^2}{2}\sigma$. Where σ represents the conductivity of the material. Thus a simple conversion into the frequency domain has been made for comparison to the analytical results.

Simulation description	Cell Size	Srce Radius	Location of Schematic
Homogeneous Sphere	2.55 mm	9.45 cm	N/A
4-Layer Laminated Sphere	2.55 mm	9.45 cm	Figure 4.6a
3-Layer Laminated Sphere	2.55 mm	9.45 cm	Figure 4.6b
2-Layer Laminated Sphere	2.55 mm	9.45 cm	Figure 4.6c
Small Head w/ Muscle Bolus	2.55 mm	9.45 cm	Figure 4.7 and 4.8
Small Head w/ Bone Bolus	2.55 mm	9.45 cm	Figure 4.7 and 4.8
Large Head w/ Muscle Bolus	3.2 mm	11.8 cm	Figure 4.7 and 4.8
Large Head w/ Bone Bolus	3.2 mm	11.8 cm	Figure 4.7 and 4.8

Table 4.1: This table gives a description of each of the setups along with the locations of their schematics.

These two modifications allow the source distribution to be specified, and the resultant field to be recorded and analyzed. The first modification allows the FDTD code to implement the source distribution around any geometry specified in the FDTD space. The code propagates the field through the space and the second modification allows the frequency response to be recorded for analysis in matlab. Appendix B gives a number of matlab routines that aid in analysis of the field distributions. These routines make it possible to look at any slice through the head as well compute errors and hot spots.

4.3 FDTD RUNS

Three basic forms of FDTD simulations are done. Table 4.1 gives a description of each setup as well as the figure numbers of the schematics. These are set up with identical FDTD space parameters, but the geometry is changed for each simulation. For these simulations, a 92x92x95 grid is set up with cubic cells 2.55 millimeters on a side. The

Courant stability condition (page 16) produces a 49.19 picosecond time step. The outer sphere in each simulation has a radius of 37 FDTD cells, or 9.45 cm. The analytical solution sets the spherical source distribution at the radius of 37 FDTD cells.

The first simulation is on a simple homogeneous sphere. This simulation serves as a validation of the code. It is to demonstrate the ability to use the FDTD code with an entire incident field specified. The results of this simulation are compared with the analytic results.

For the second simulations, a series of laminated spheres simulates the skin-bone-brain structure of the human head. Figure 4.7 shows a schematic of each of these simulations. The first of these is a two level sphere the outer shell being bone, the inner being muscle. This model defines an inner sphere at a radius of 32 FDTD cells. The next simulation is of a three-layer model composed of an outer muscle layer to simulate the skin and bolus, a layer of bone to simulate the skull and an inner sphere of muscle simulating the brain. The radius for the inner sphere was 18 cells, the outer radius for the bone sphere is 19 cells and the outer sphere is again at a radius of 37 FDTD cells. A four layer model comprises the final simulation. This contained an outer shell of bone, to simulate a bone-like fluid bolus, a thin layer of muscle tissue, simulating the skin layer, a bone sphere to simulate the skull and finally an inner shell of muscle, simulating the brain. For this simulation, the radius of the inner sphere is thirty-two FDTD cells. The outer radius of the bone layer is thirty-four FDTD cells, and the radius of the skin shell is 35 FDTD cells.
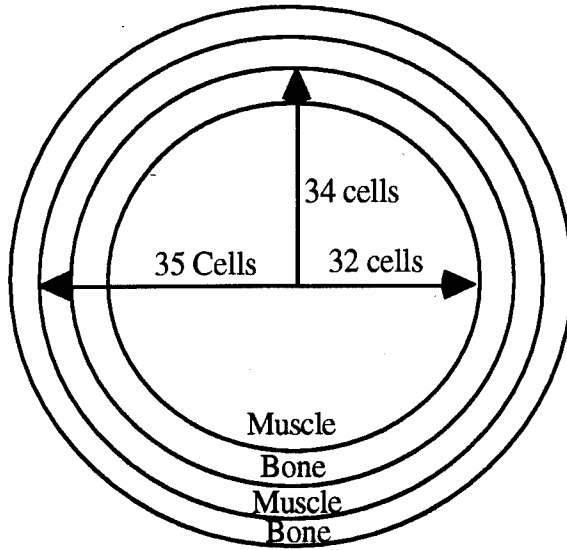
Figure 4.7a: 4-Layer Model
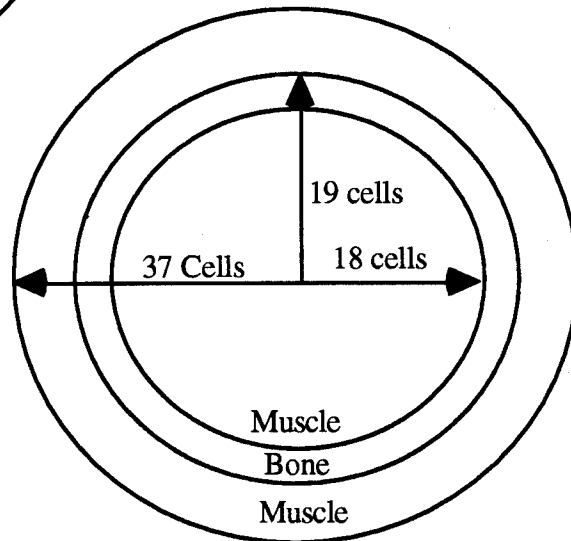
Figure 4.7b: 3 Layer Model
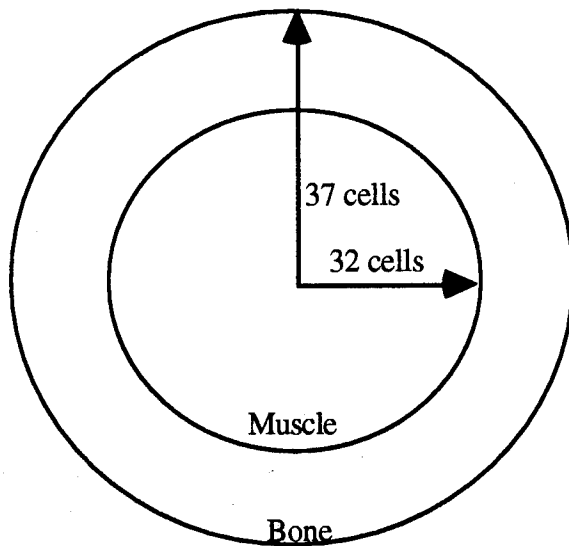
Figure 4.7c: 2-Layer Model

Figure 4.7: This figure shows a schematic of each of the laminated sphere simulations (not to scale). 4.7a is the four layer sphere, 4.7b is the three layer sphere and 4.7c is the two layer sphere.

An FDTD model of an actual human head provides the basis for the final simulations. This model is made by converting an MRI scan of a human head into a head mesh to be read in by the Penn State FDTD code. This is a four tissue model of the head. To create it, the MRI scan creates a map of the different materials of the head. It is then necessary to determine the actual tissue type at each location. Once the operator determines the exact tissue type, the typical electrical characteristics of each tissue are assigned to each point in the FDTD space. In doing this, the actual permeabilities, permitivities, conductivities and magnetic conductivities are never directly measured. Typical values are inserted for each material type. This provides a first level approximation to the human head. The addition of a basic neck extension was added to the Penn State head to simulate the inability to place a source in the neck region. The addition of a neck is a simple extension of the final layer in the head down to the edge of the FDTD grid. Figures 4.8 and 4.9 show two cuts through the head model. X=0 is the back of the head, Y=0 is the left side of the head and Z=0 corresponds to the bottom of the head.
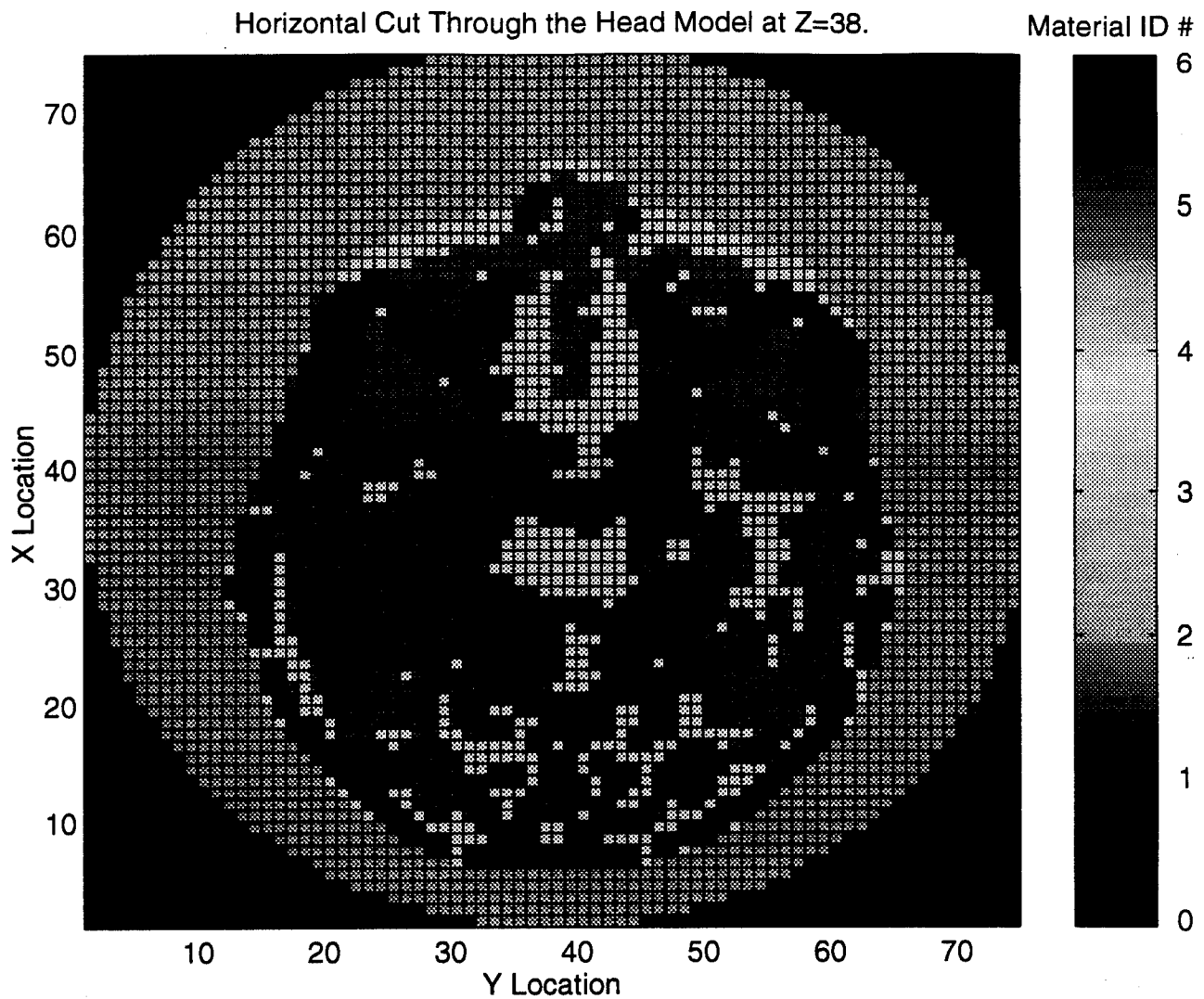
Figure 4.8: This figure shows a horizontal cut through the center of the head model. X=0 corresponds to the back of the head and Y=0 corresponds to the left side of the head.

A liquid bolus surrounds this head approximation. This bolus allows the use of the spherical source distribution on the edge of the bolus, providing a closer match in material parameters as the field propagates into the head. Although it is about 9.45 cm to the center of the head, it is not spherical; therefore, the full size head cannot fit within the 9.45 cm bolus and has to be shrunk for the initial tests. To do accomplish this, the original head

Coronal Cut Through the Head Model at X=38.
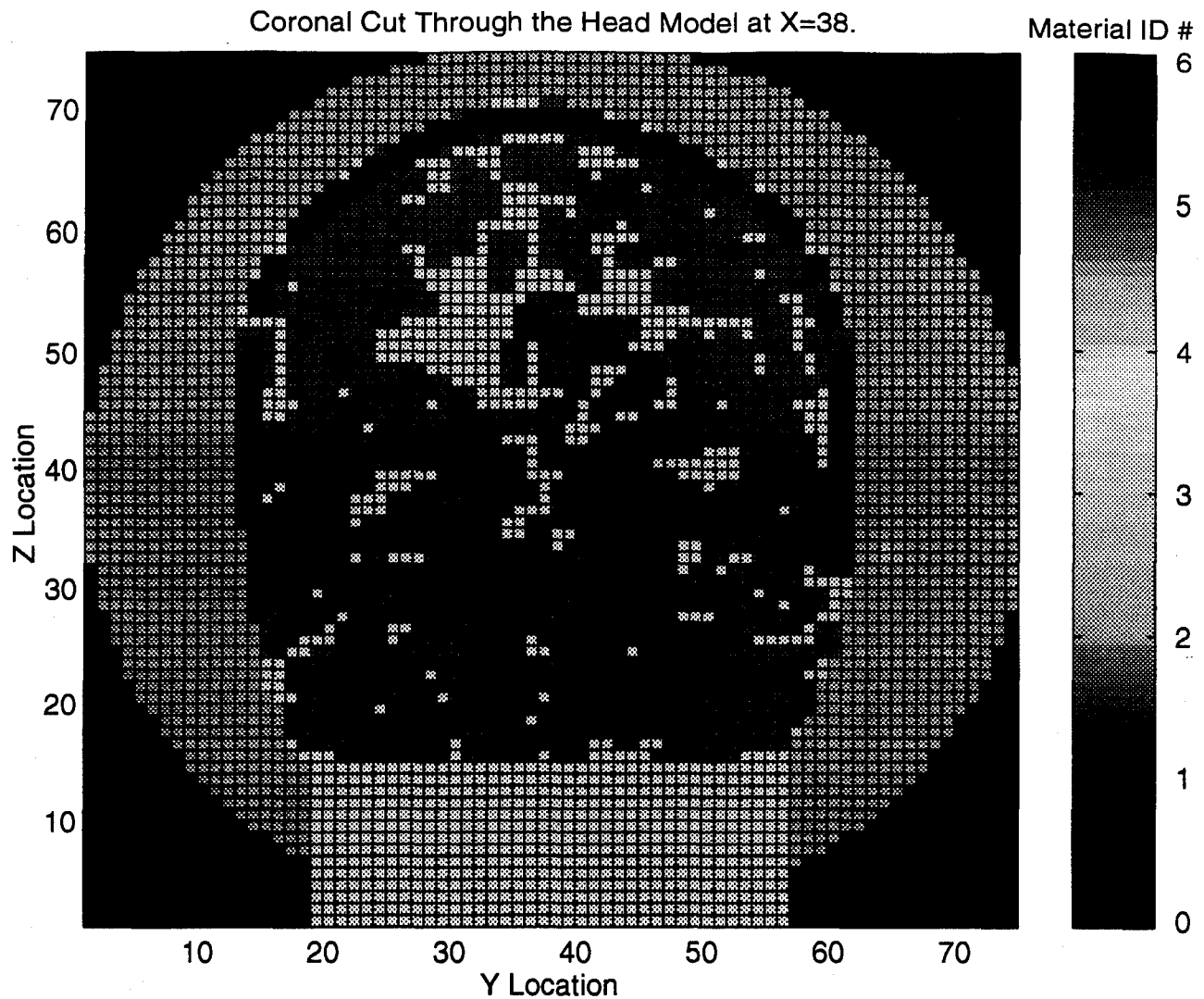
Figure 4.9: This figure shows a longitudinal cut through the center of the head model. Y=0 is the left side of the head and Z=0 is the bottom of the head.

mesh cell size of 3.2 mm is reduced to 2.554 millimeters. The material characteristics of

the bolus can be set at any value desired. The first simulation gives muscle-like

characteristics to the bolus. The second simulation uses a bone-like bolus. These two

simulations provide a comparison to determine which material characteristics in the bolus

are preferred.

41

Along with the simulations using a small head model, two simulations use the full size human head. For these simulations, the cell size increases from 2.554 millimeters to 3.2 millimeters on each side of the FDTD cubes. These simulations provide an opportunity to determine if increasing the penetration depth in the actual head is possible. Brain tissue is less lossy than muscle tissue; therefore, it is conceivable that greater penetration may be possible in the presence of the inhomogeneities of the human head. These two simulations also contain one simulation with a bone-like bolus and one done on a head with a muscle-like bolus.

5. Results

The results for all the simulations proved to be very encouraging. The analytic simulation duplicates Rappaport's work with excellent accuracy, indicating a 9.45 cm sphere as the maximum size sphere through which a centrally located tumor could be irradiated. The FDTD simulation on a homogeneous sphere shows excellent correlation with the analytic simulations. These results show it is possible to model this scenario using the FDTD method. The laminated sphere simulations demonstrate a "staircase" effect error introduced from the cubed approximation of spheres. This illustrates an error to watch for in the head simulations. Finally, the head simulations prove that not only will this technique work on a small head within the 9.45 cm optimal radius, it will also work on a full sized human head.

All the figures in this section refer to levels within the spheres. These levels correspond to grid cells within the FDTD space; e.g., X=38 refers to 38th plane forward from the back of the head. FDTD simulation requires a 10 cell empty space region around the spheres that is cut out to clarify the results' descriptions; therefore, the levels run from 1 to 75. Since the spheres were 37 cells in radius, the exact center of the spheres and head are at X=38, Y=38, Z=38. The bottom of the head is at Z=1, the back of the head is at X=1 and the left side of the head is located at Y=1.

5.1 Analytical Simulation

The first simulation solves the analytic solution across space for the homogeneous sphere. This simulation serves as the control to ensure FDTD gives reasonable results in this treatment scenario. Figures 5.1 and 5.2 show the results for this simulation. These figures show a cut through the equator of the sphere (figure 5.1) and a cut through a meridian of the sphere (figure 5.2). Each grid increment represents an increase of 2.554 millimeters. Therefore, the 37 cell radius sphere is equivalent to the 9.45 centimeter radius source shell. The matlab analysis removes everything outside the location of the
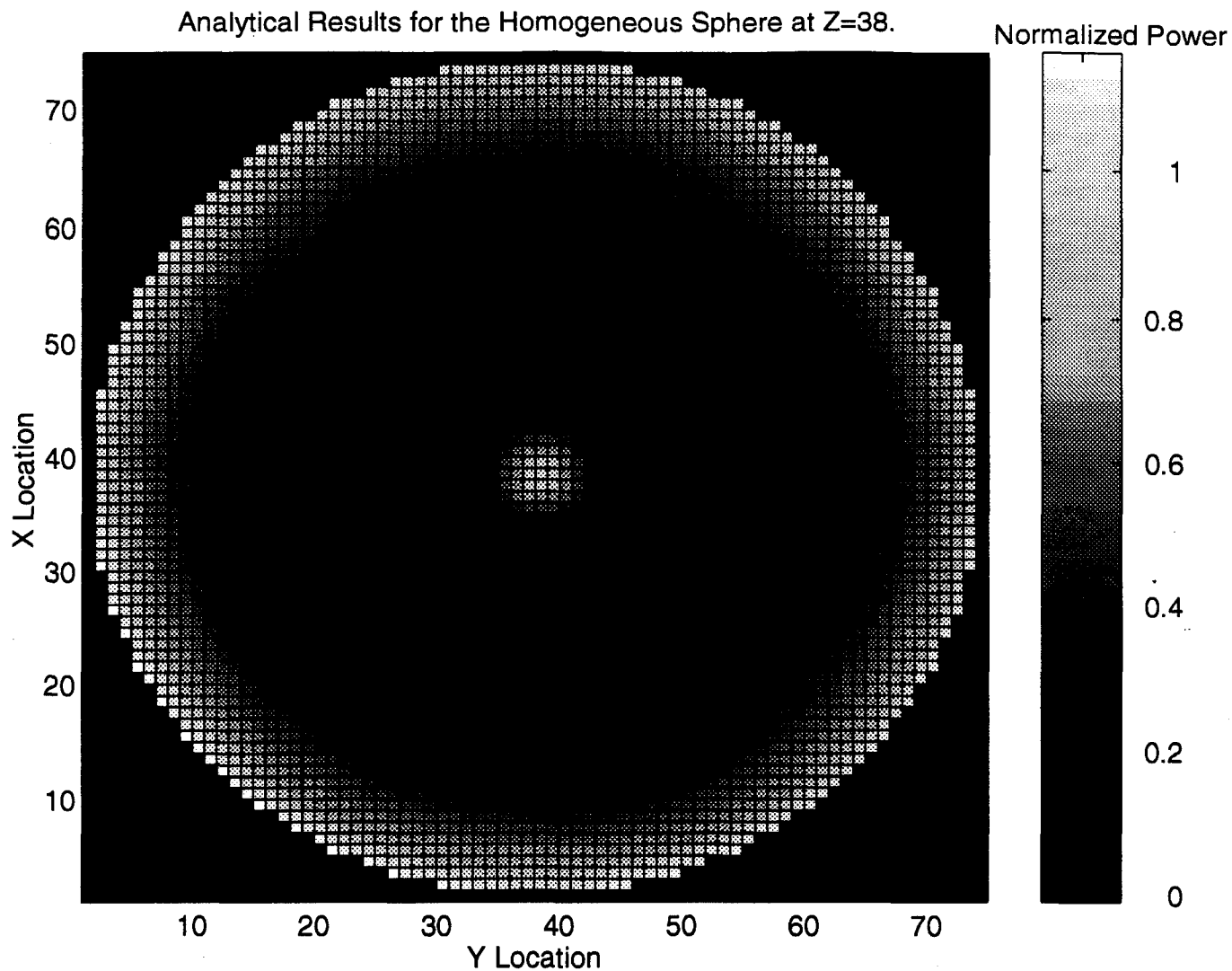
Figure 5.1: This figure shows the analytical results for the power distribution across the center XY plane of the homogeneous sphere (normalized to one at the center). Everything outside the proposed source location is removed for clarity.

theoretical source to clarify the plots. In reality, the field would continue to grow towards the corners. This is because the analytic solution describes an E-field distribution and not a radiating source.
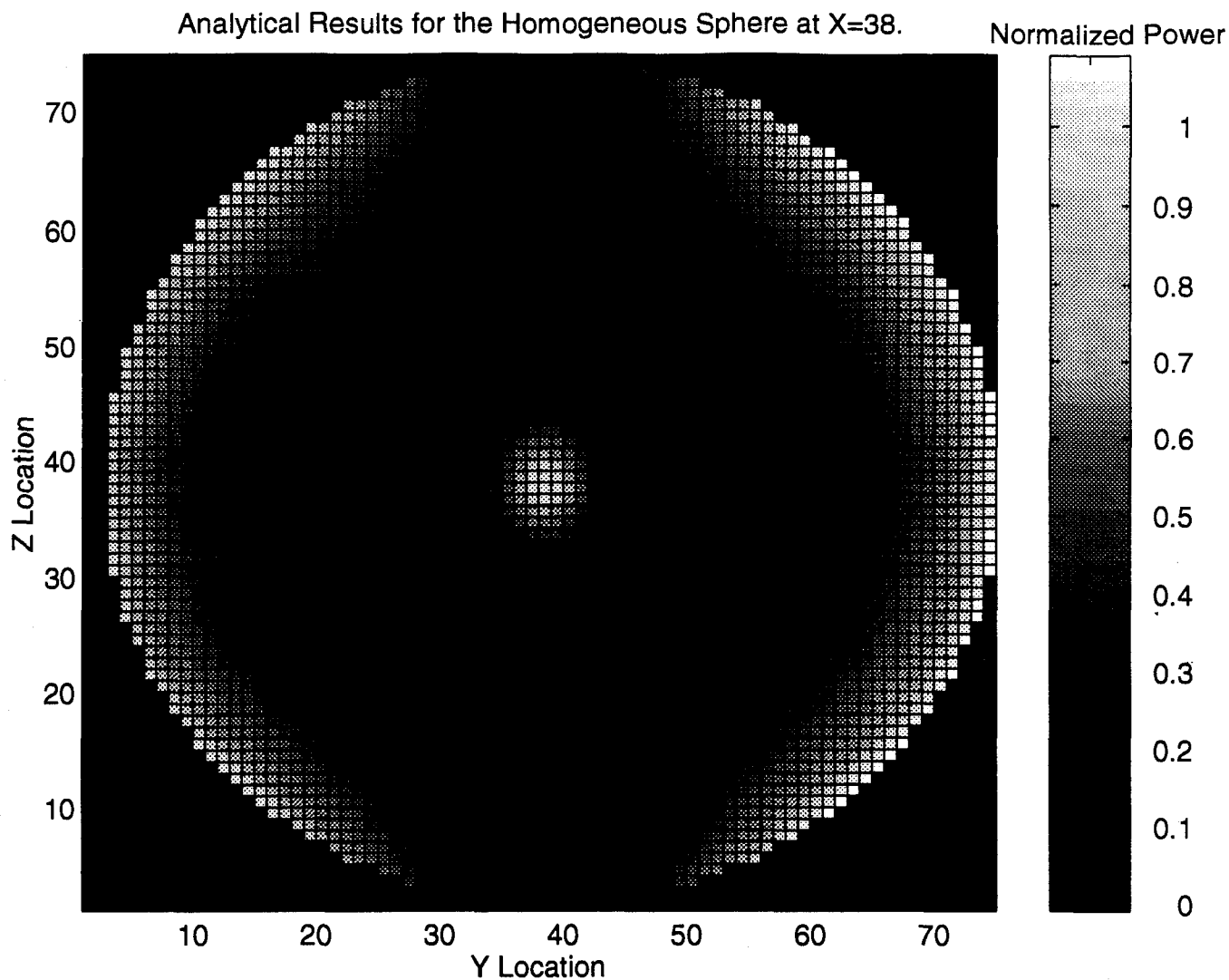
Figure 5.2: This figure shows the analytical results for the power distribution across the center YZ plane of the homogeneous sphere (normalized to one at the center). Everything outside the proposed source location is removed for clarity.

Figure 5.1 shows the central XY plane of the sphere. The light circle in the center is the location of the power concentration. Because the pattern as no phi dependence, this pattern is completely symmetric. Figure 5.2 shows the central YZ plane of the sphere. Again the light spot in the center of the sphere illustrates the power focus. Unlike the XY plane, this power profile is not symmetric. This would be expected due to the theta

dependence produced by the optimization process. Recall that the final field had very little strength near the poles and a power maximum at three points near the equator (figure 3.6).

5.2 FDTD Simulations on a Homogeneous Sphere

The first simulation on the FDTD sphere proved to be ineffective. This simulation produced significant spikes along the poles. An analysis of this simulation displays spikes of over four hundred times the value of the E-field at the center along the top and bottom of the sphere. Therefore, the power is not completely coupling into the sphere. Defining the source as a surface causes these spikes. That is, when the code reaches a point in a grid that is along the spherical source, it sets the three field components corresponding to that cell location to the value the optimal analytical solution dictates. This produces a surface of sources. This surface contains small holes along the stepped edges of the sphere. Because of these holes, the source does not isolate the inside of the sphere from the outside and the E-field circulates through the holes which prevents it from completely coupling into the muscle sphere and creates the spikes. This obstructs the power at the center from reaching its full potential value.

To reduce this effect, the source was redefined as a cubic volume instead of a surface. In other words, at each source point the code defines six source components instead of three. This cubic volume eliminates the holes and creates a continuous spherical source.

There remains one other consideration in the source distribution. Recall that the Yee cell geometry places each field component in a slightly different spatial location. Therefore, to be completely accurate in defining the source distribution, the code must recalculate the value for each field component based on its specific position. This requires six individual calculations for each source cube at every time step, adding tremendous computation time to an already slow process.

Therefore, two more homogeneous simulations investigate the effect of an exact source distribution versus an approximate distribution to speed computation time. The

approximate source code calculates what the source component values should be at the center of the cube and defines all six components based on these values. This reduces the computation time by a factor of six with a minimal loss in accuracy. Table 5.1 shows a comparison of the results. The table gives the percent error and standard deviation versus the analytic results.

FDTD Simulation	Mean % Error Vs. Analytic Simulation	Standard Deviation Vs. Analytic Simulation
Exact	5.39%	7.84%
Approximate	6.00%	8.49%

Table5.1: Comparison of exact and approximate source distributions for homogeneous sphere FDTD simulations

The error shown in table 5.1 indicates very little loss in accuracy due to the approximation of the source. The tremendous gain in computation time and small loss in accuracy dictates the use of the approximate solution for remaining simulations. Figure 5.3 shows a mesh of the power distribution across the YZ plane of the FDTD approximate source simulation. Again, each grid increment is equivalent to 2.554 millimeters. The spikes along the top and bottom of the sphere show locations where the field is not completely coupling into the muscle tissue. This effect is pronounced at the top and bottom of the sphere because of the polarization. Since the tangential component of the E-field is always continuous and the field is essentially Z-polarized, the field along the equator is tangential and couples completely. The field near the poles is normal to the sphere's surface. Because the normal E-field is discontinuous by a factor of the difference in the permitivities, the field at the poles does not completely couple into the muscle tissue; forming the spikes.

E–Field Across the Homnogeneous Sphere at Z=38 (approximate source).
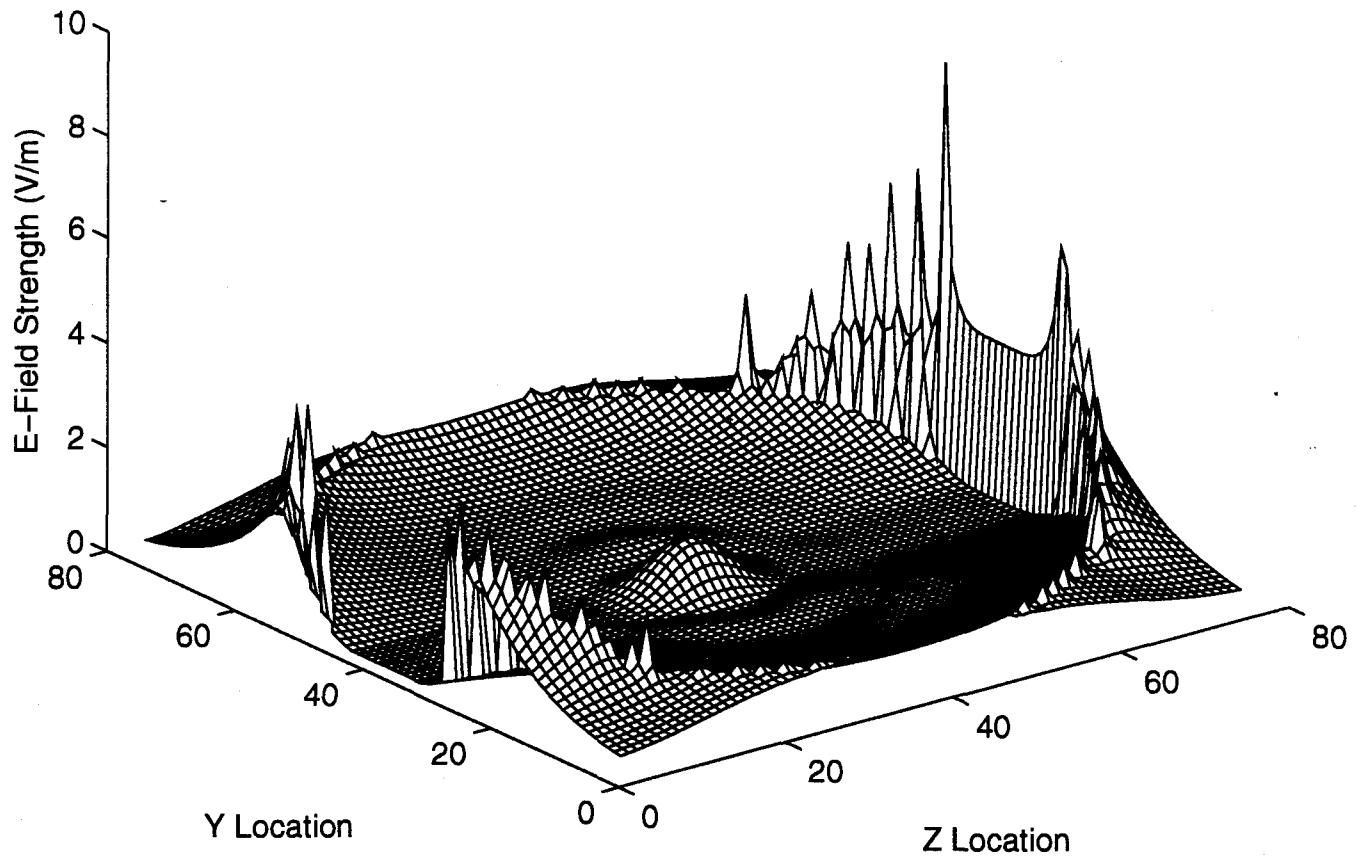
Figure 5.3: Mesh of the power distribution across the YZ plane of the homogeneous sphere. The results shown are of the FDTD simulation on the homogeneous sphere with an approximate source distribution (normalized to one at the center).

Despite this incomplete coupling, the field profiles show good correlation to the analytical results. Comparing the similarities between the FDTD field solution in figure 5.4 and 5.5 and the analytical solutions shown in figures 5.1 and 5.2 shows this correlation. Figure 5.4 is a cut through the equator of the sphere showing the power profile calculated by the FDTD model. Figure 5.5 shows the power profile across the center YZ plane

through the sphere. Both of these plots have the fields set to zero outside the sphere to clarify the display. Again the bright spot at the center shows the focusing of the power.
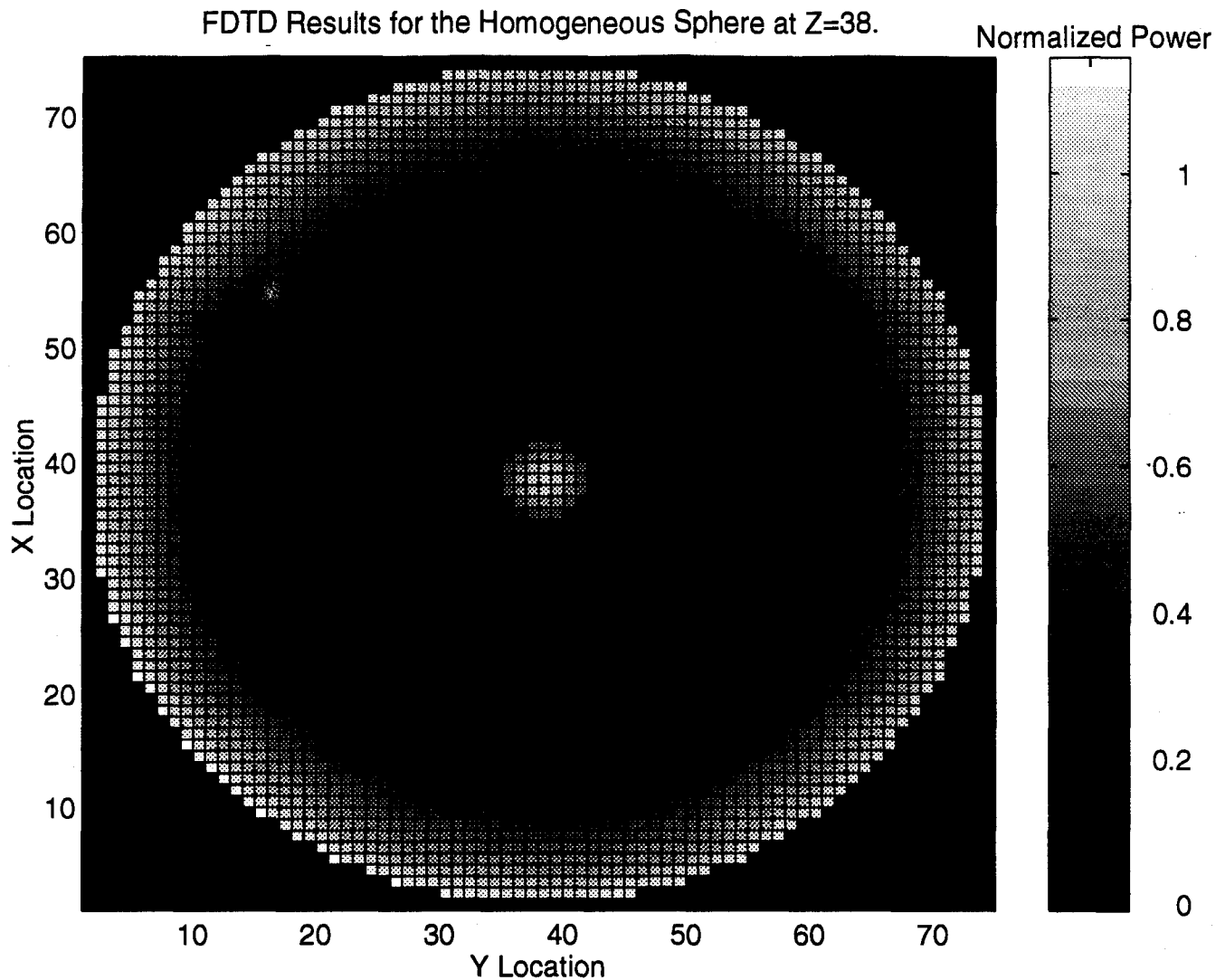
Figure 5.4: Power profile across the equatorial cut through the homogeneous sphere with an approximate source distribution (normalized to one at the center, source removed).

Figures 5.6 and 5.7 shows the FDTD power profile along with the analytical solution along the central Y and Z lines in figures 5.6 and 5.7. These plots show extremely strong correlation between the analytical and the FDTD solutions along the central lines.
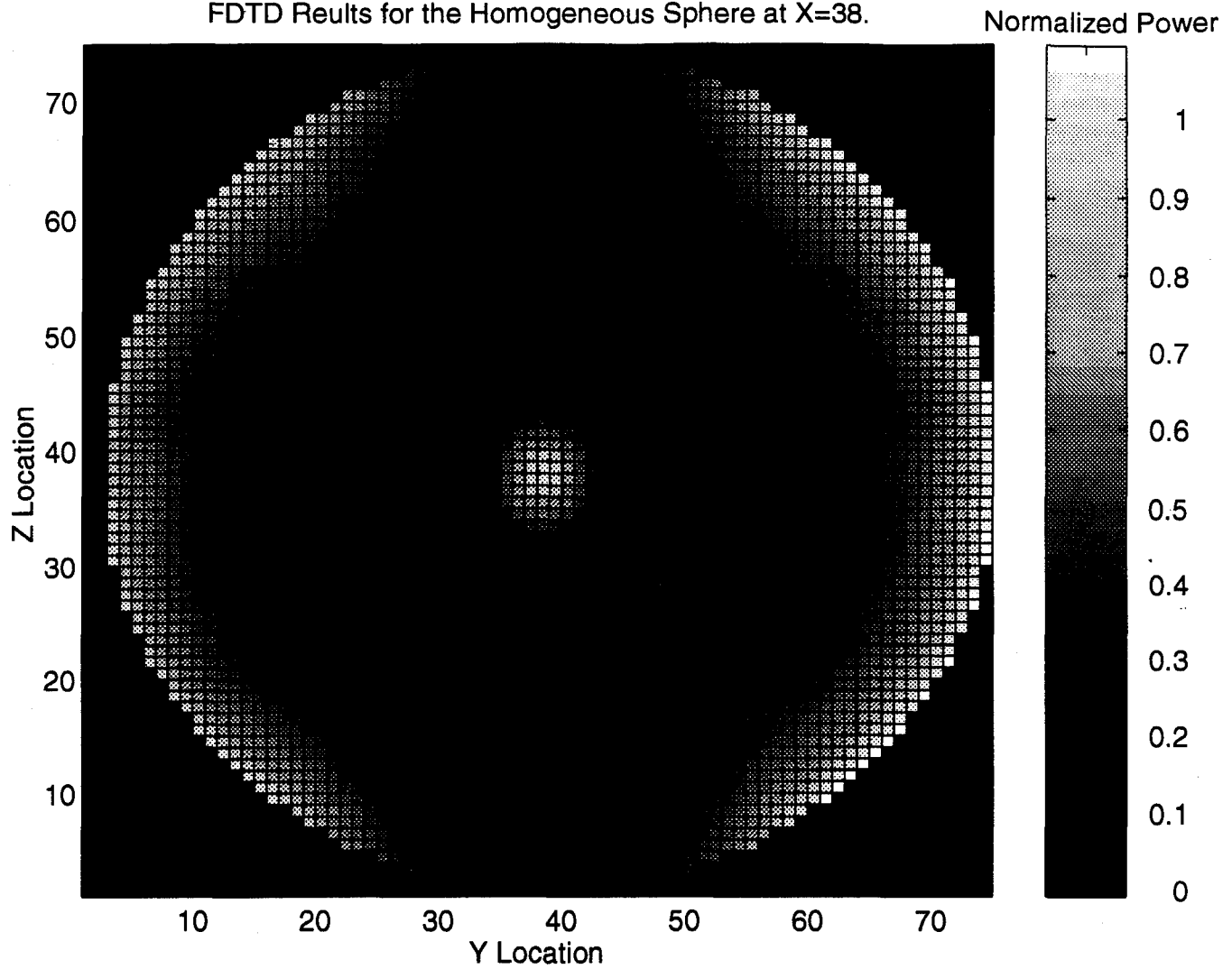
Figure 5.5: Power Profile across the central YZ cut through the homogeneous sphere with an approximate source (normalized to one at the center, source removed).
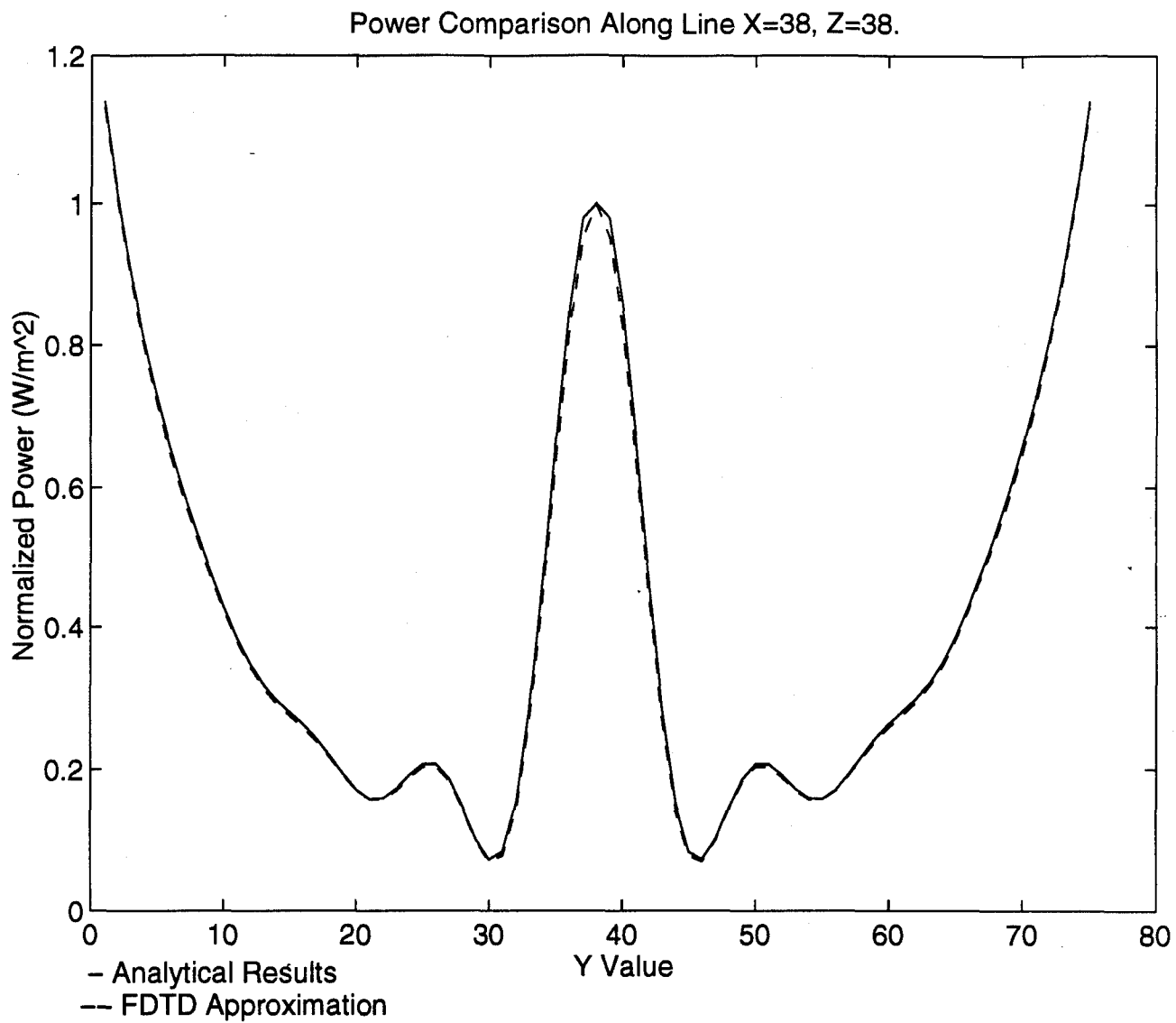
Figure 5.6: Power comparison along the line X=38, Z=38 showing Analytical and FDTD results (normalized to one at the center).
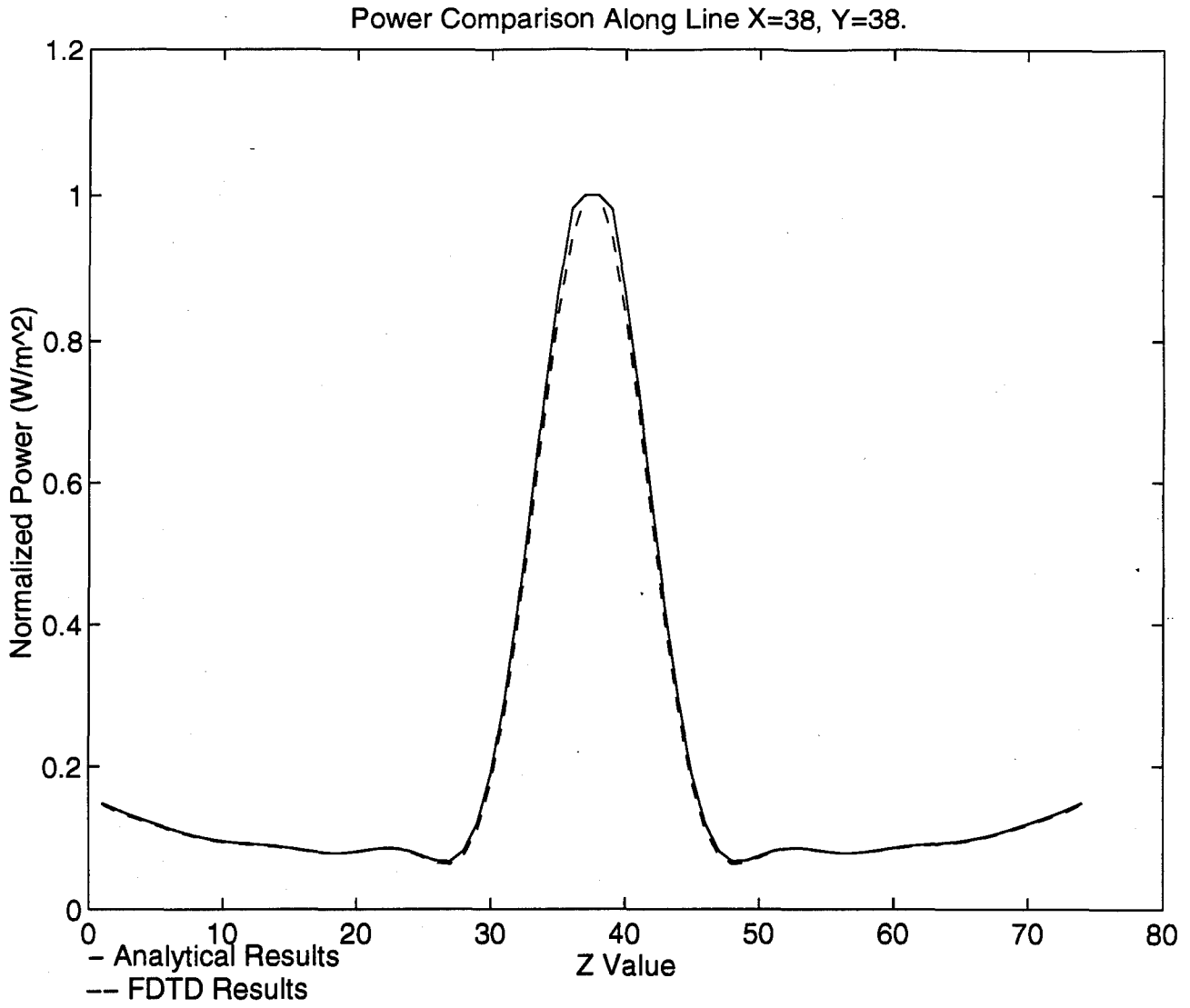
Figure 5.7: Power comparison along the line X=38, Y=38 showing Analytical and FDTD results (normalized to one at the center).
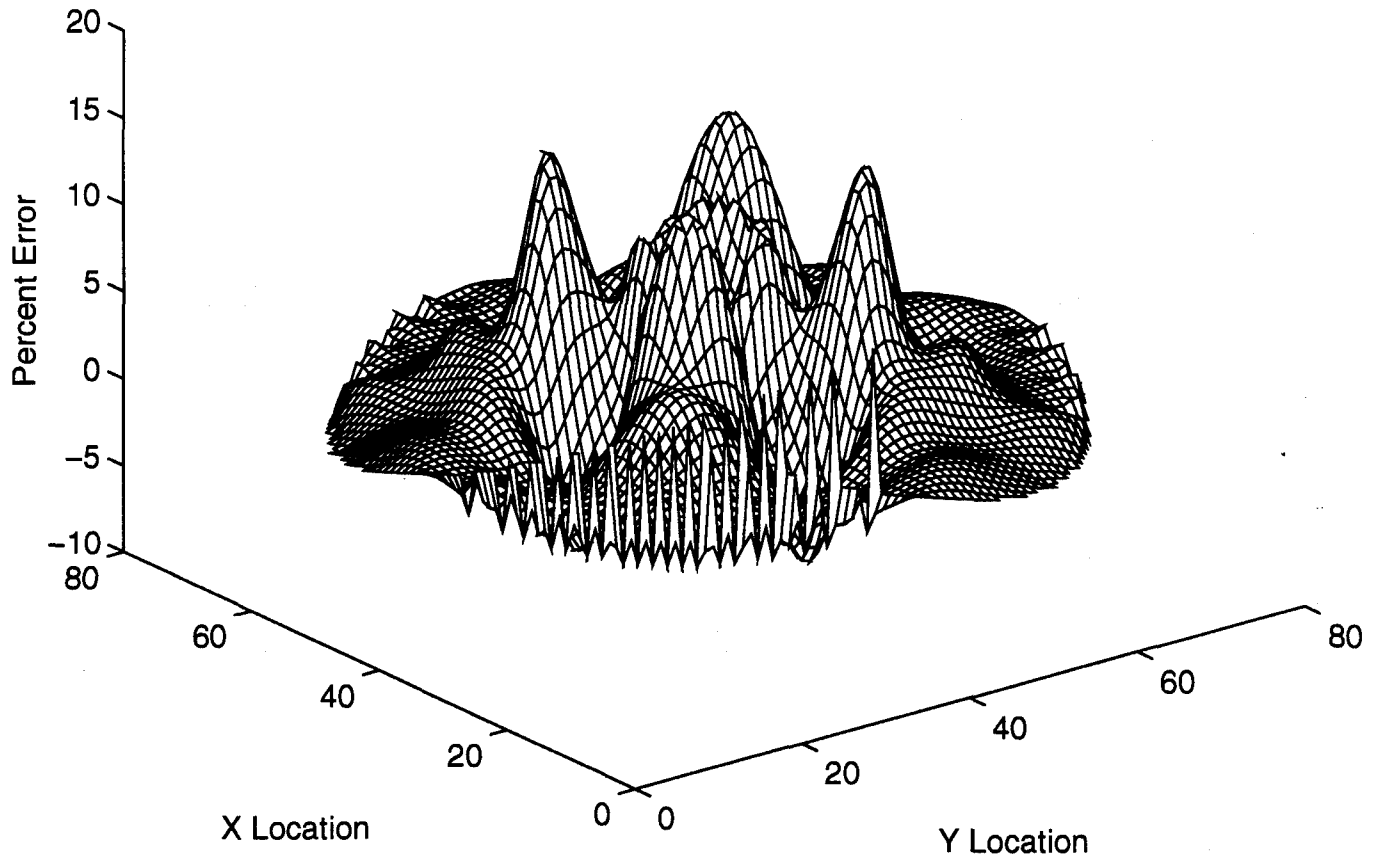
Figure 5.8: Equatorial cut showing the error between the analytical and FDTD results for the homogeneous sphere.

Figure 5.8 shows the error between the analytical simulation and the FDTD simulation with an approximate source distribution. This figure shows the error across the equatorial cut of the sphere. As expected, this central plane has exceptionally low error, with a maximum around 8%. With such strong correlation along the central lines and the equatorial cut the question becomes where the error lies.

The answer to this question comes by looking at figure 5.9 which shows the error across the central YZ plane. It is clear from this mesh that the majority of the error is coming along the central core of the sphere along the Z-axis. This is expected because figure 5.3 showed earlier that the power was not completely coupling into the sphere near the poles. Since the power is not completely entering the sphere in these regions due to the E-field discontinuity, the power profile of the FDTD solution will differ from that of the analytical solution near the poles. In addition, the interference of all the sources in the respective hemisphere forms the power along the central core. Thus, the lack of complete coupling at the poles only slightly effects the power near the edges. However, the small effects on the edges will combine in the central region where interference occurs producing expanded error. In other words, although the majority of the interference occurs at the focus, there will also be some amount of interference in the central region that will combine the small loss along the poles into a significant amount of error.
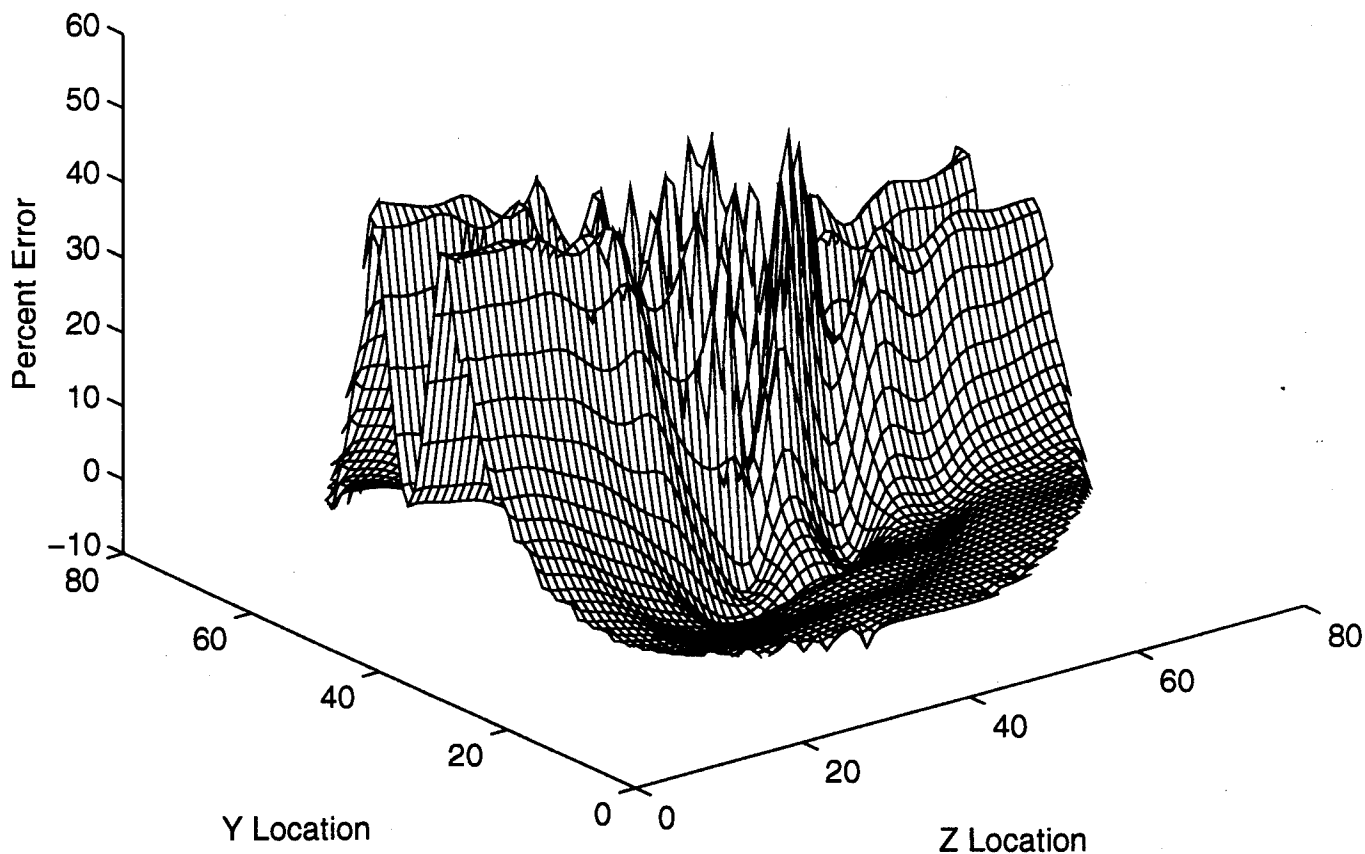
Figure 5.9: Central YZ cut showing the error between the analytical and FDTD results for the homogeneous sphere.

5.3 FDTD simulations on Laminated Spheres

The next series of simulations are done on laminated spheres to investigate the effects of adding simple inhomogeneous geometries into FDTD. These simulations all demonstrated the same stair step spikes introduced by the stair step approximation necessary in modeling a sphere as a series of cubes. The schematics for each of the simulations is shown in figrue 4.6.

Figure 5.10: 3-D plot of the E-field across the equatorial cut of the four-layer laminated sphere.

The first of these simulations is on a four-layer sphere (figure 4.7a). The material properties of the outer sphere model bone-like material. The next layer down patterns muscle material. The third layer is defined as bone material. Finally, the properties of the inner sphere imitate muscle tissue. Therefore, this simulation is attempting to recreate a liquid bolus with bone-like electrical characteristics around a head. This simulation models the head as a muscle-like brain core surrounded by a spherical 'skull' of bone and finally a thin 'skin' layer of muscle tissue.

Figure 5.10 shows the E-field distribution across the central XY cut of the laminated sphere normalized to one at the center. The field along the equator of the sphere is predominately directed in the Z direction. Thus, along this equatorial cut, the field will be tangent to the surface of each sphere. Because the tangential E-field has to be continuous across a dielectric boundary, along this cut the field should be continuous everywhere. Figure 5.10 shows this is not the case. There are E-field spikes along the edges of the inner spheres. The stair stepped edges of the spheres causes this phenomenon. Instead of having a smooth surface, small cubes compose the edge. At some point a given layer of cubes ends producing an edge. This edge produces a locally horizontal rather than vertical surface. At this point the E-field becomes normal rather than tangential. The amount of the discontinuity of the normal E-fields is proportional to the difference in relative permitivities of the two materials; therefore, the field spikes in the cube.
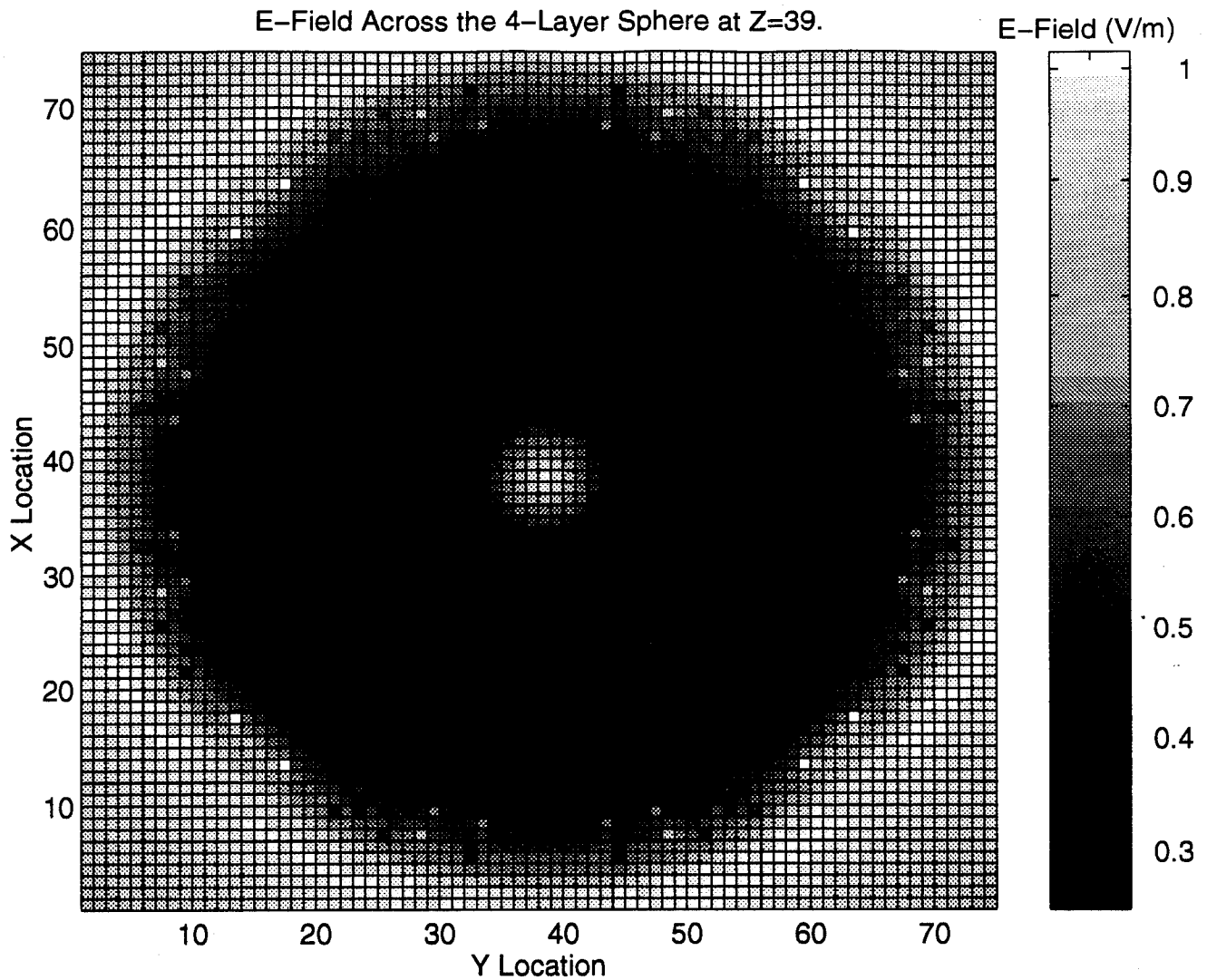
Figure 5.11: 2-D image of the E-field distribution across the Z=39 cut of the 4-layer laminated sphere.

Figures 5.11 and 5.12 illustrate the effect of the staircase errors. Figure 5.11 shows the E-field distribution across the sphere in a two-dimensional image. The spikes show up as single pixels slightly darker or lighter than those around them. Figure 5.12 is plot of the changes in the IDTHRE components from level Z=39 to level Z=40. Recall that the IDTHRE array contains the material ID's for the Z-directed geometry components.

Changes in IDTHRE Components of 4–Layer Sphere From Z=40 to Z=39.
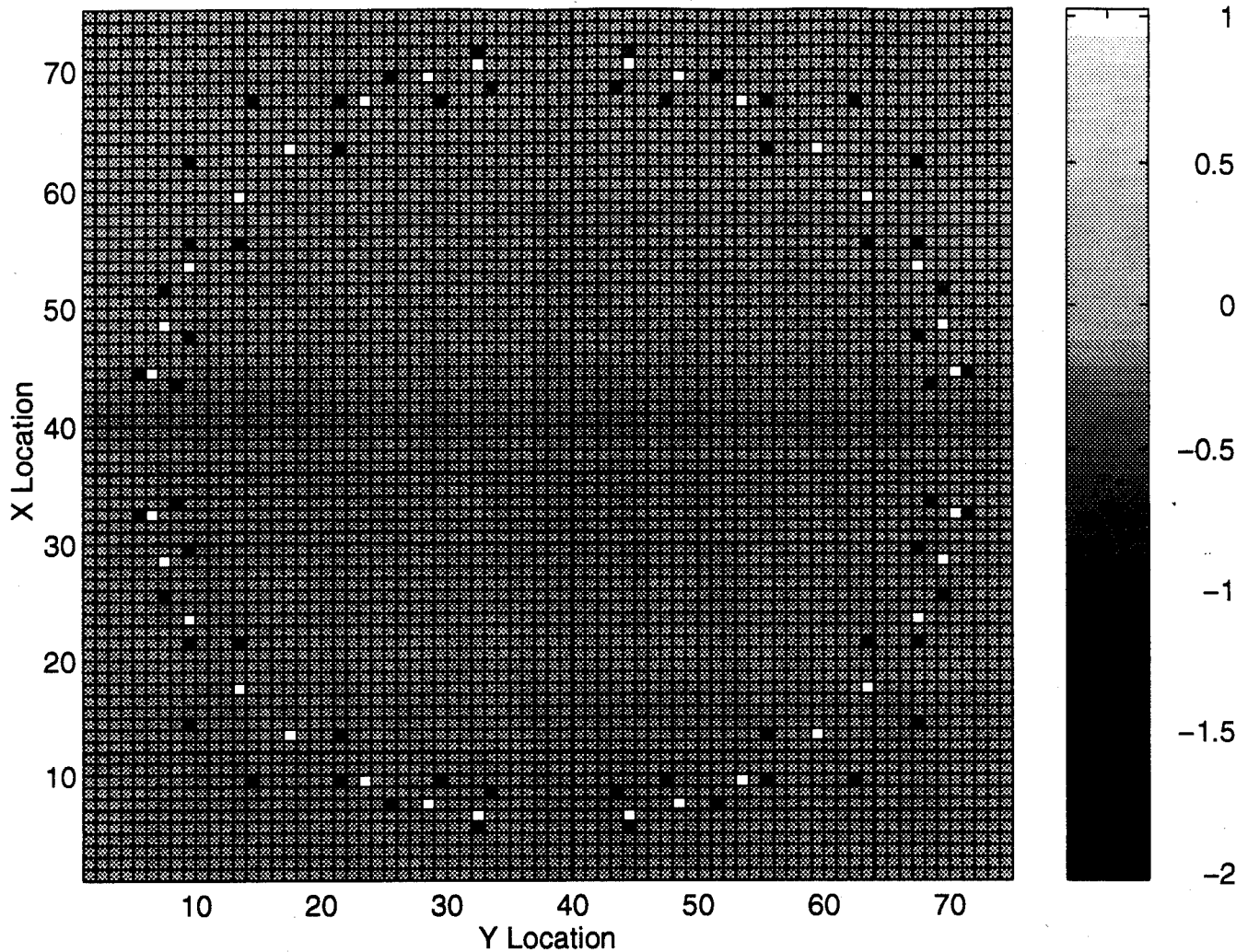
Figure 5.12: This figure shows a 2-D image of the changes in the Z-directed material components from Z=39 to Z=40.

That is, where the IDTHRE, or Z-directed component changes from one level to the next, there is a locally horizontal surface where it should be vertical. Therefore, figure 5.12 shows only the location of each stair step. Investigation of figures 5.11 and 5.12 reveals that every spike corresponds to the edge of a stair step. These spikes are numerical artifacts which will not occur in actual practice.

E–Field Across 4–Layer Sphere at X=38.
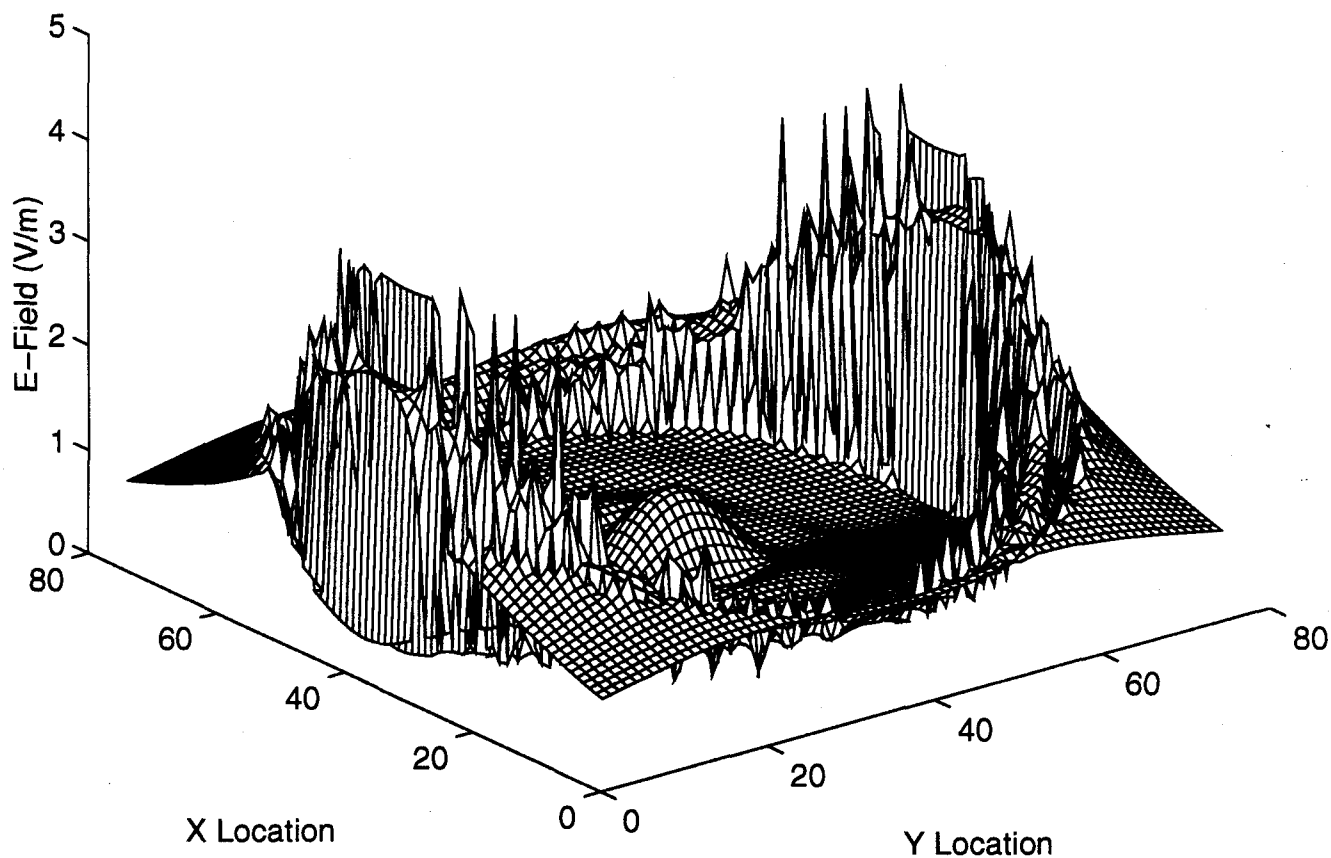
Figure 5.13: This figure shows a 3-D mesh of the E-field distribution across the central YZ cut of the four-layer model.

Figure 5.13 shows the E-field distribution across the central YZ plane of the 4-layer sphere. As expected, the field is continuous along the central Y line. The discontinuities through the center spheres become more apparent near the poles. This is because the field is predominately Z-directed; therefore nearer the poles the field is normal rather than tangential to the dielectric interface so the discontinuity will be larger.

The next simulation incorporated three layers as compared to the former 4-layer model. The 3-layer simulation produced the same stair step spikes along with a new phenomenon . The 3-layer model had a much smaller 'skull' layer than any of the other models (figure 4.7b). As the field nears the center, the radial component becomes more pronounced. Thus, along the equatorial cut, shown in figure 5.14, the field has a noticeable discrepancy as it passes through the dielectric interfaces. The radial component is more prominent near the center of the sphere causing the discontinuity. The field thus has a larger normal component to produce the discontinuity.

E-Field Across 2-Layer Sphere at Z=38.
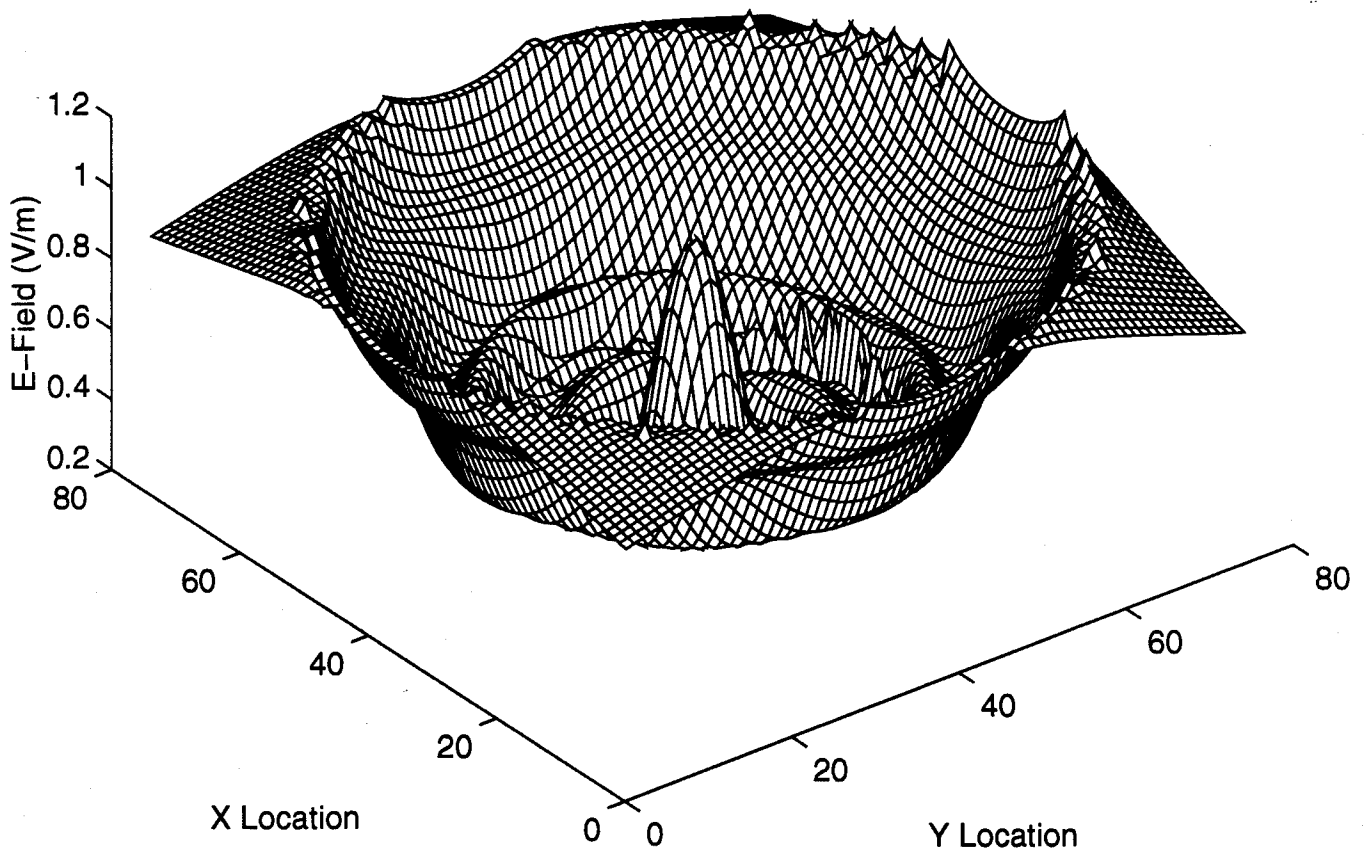
Figure 5.14: This figure shows the E-Field across the equatorial cut of the 3-layer sphere model (normalized to one at the center).

61
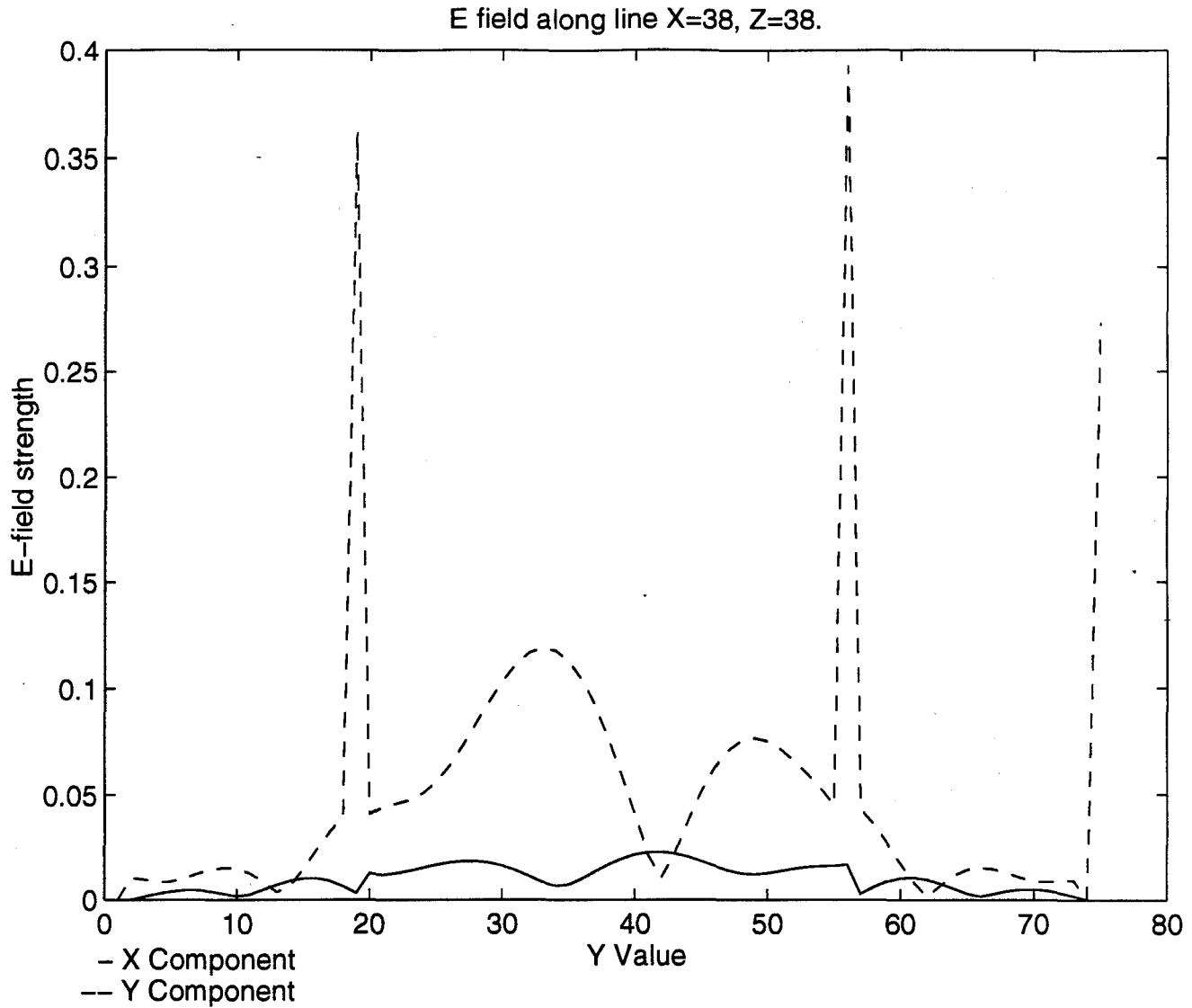
Figure 5.15: Plot of the X and Y E-field components along an equatorial radial line in the 3-layer Sphere model (E-field normalized to one at the center).

Figure 5.15 is a plot of the x and y components of the E-field along an equatorial radial line. The Z directed component contains the theta component along equatorial plane. The X and Y directed components contain the radial component. Figure 5.15 shows these two components along an equatorial line. From this plot the discontinuity can be seen to be due to the larger radial component that is normal to the interface.

Using the 2-layer model (figure 4.7c) in the next simulation showed the same stair step spikes seen in the other laminated sphere simulations. Figures 5.16 and 5.17 show

the results of this simulation. Figure 5.16 is a mesh of the field strength across the

equatorial cut of the 2-layer sphere. Figure 5.17 shows the field strength across the central

YZ plane.

E-Field Across 2-Layer Sphere at Z=38.
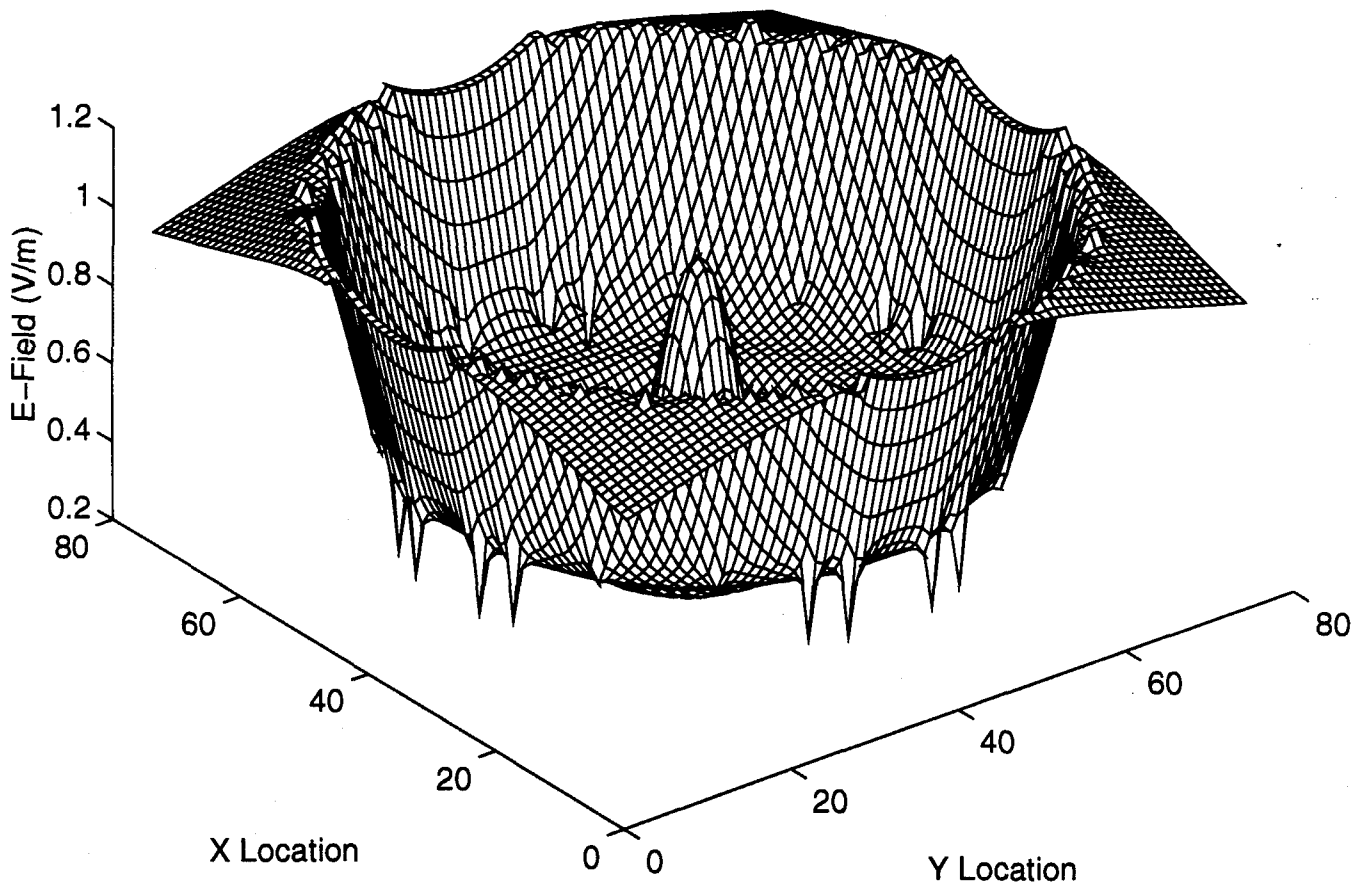
Figure 5.16: This figure shows a 3-D mesh of the E-field strength across the equatorial plane of the two-layer model (normalized to one at the center).

E–Field Across 2–Layer Sphere at X=38.
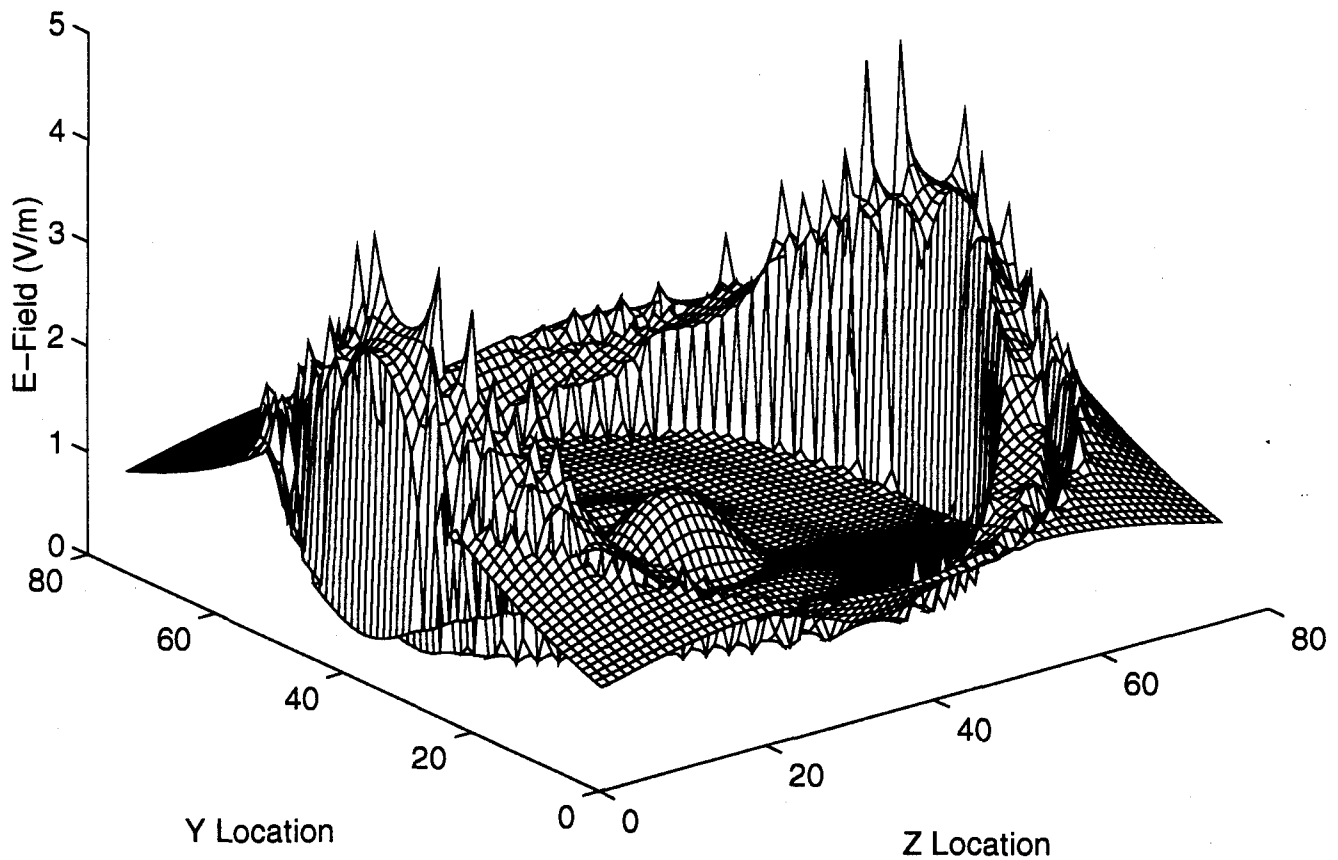
Figure 5.17: This figure shows a 3-D mesh of the E-field strength across the central YZ plane of the two-layer model (normalized to one at the center).

These simulations on laminated spheres show several important aspects that will be seen in the simulations on the actual head model. The most important of these lessons is the presence of the "staircase" spikes. The head simulation shows these spikes as well. It is important to keep in mind that extended spikes due to a true horizontal surface will occur; the single cell spikes, however, are due to the "staircase" error and would not occur in actual practice. Another lesson this illustrates is the spiking due to the horizontal surfaces

near the poles. Computing the power will significantly reduce the spiking due to the very low conductivities of the bone tissue where the spiking occurs. If it does become a problem, going back to the original field distribution that concentrates the source power more near the equator can reduce this spiking.

5.4 FDTD Simulations on the Head Model

After investigating the effects of the simple inhomogeneities, The next simulation places the head model derived from an MRI scan within the homogeneous sphere. The sphere will then act as a model of a liquid bolus placed around the patient's head. This bolus is used to help the field couple more completely into the tissue. To investigate the effects of bolus composition, two different bolus types are used, a bone-like bolus and a muscle-like bolus. This provides the basis for five different head simulations. The first is an error, reported here to demonstrate the importance of proper characteristics. The next two simulations use a shrunken head with both a bone-like and a muscle-like bolus. The final two simulations use a full size head model, one with a bone-like bolus and one with a muscle-like bolus.

The first simulations on the head model produce troubling results. The inhomogeneous head model had absolutely no correlation to the simulation on the head model. A mesh across the central horizontal slice is shown in figure 5.18. This plot shows tremendous spiking throughout the edge regions and practically no focusing. Further investigation shows these discrepancies are due to inaccurate material characteristics in the head model. The model had been given the material characteristics of fat rather than muscle for the brain tissue. These results demonstrate the importance of the optimization process. The focusing could be accomplished on such a head; however, a new optimization would have to be done to account for the different material characteristics associated with fat.

Power Across Fat Head Model at Z=38.
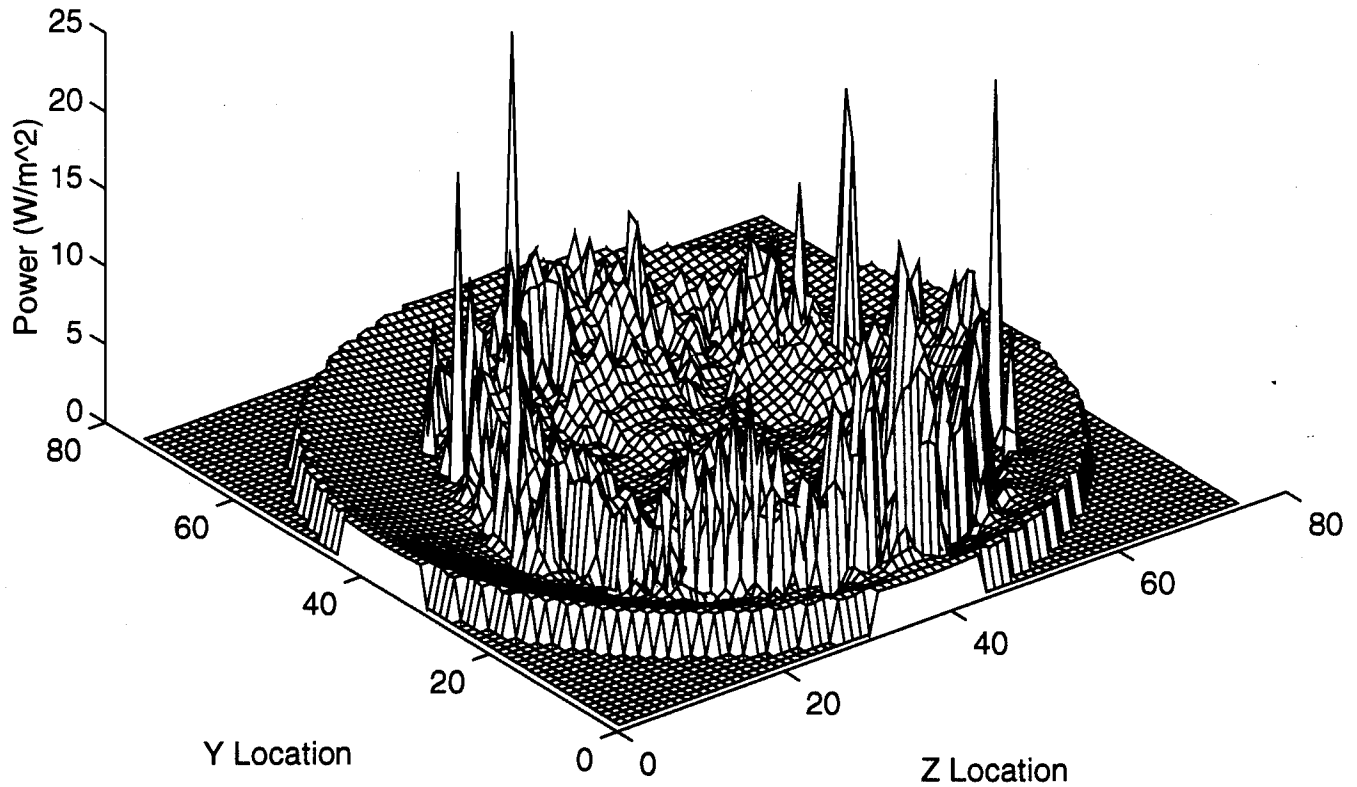
Figure 5.18: Power across the central horizontal slice of the head model (normalized to one at the center). These results are of a head with a bone-like bolus and brain tissue defined as fat.

The remaining four simulations again use the model of the head developed from an MRI scan, except with proper material characteristics. The material characteristics define three different materials with muscle-like properties representing skin and white and gray matter, and one material with the low-water content properties of bone. The first two of these uses a head that is reduced to fit within the 9.45 cm source shell. The second two use a full size head, with an enlarged source shell to fit around the enlarged head. Each of these sets contains one simulation with a bone-like bolus and one done with a muscle-like

bolus. Figures 5.19 through 5.22 show a plot across the central XY plane of each of these simulations.

Horizontal cut of the small head with muscle–like bolus at Z=38.
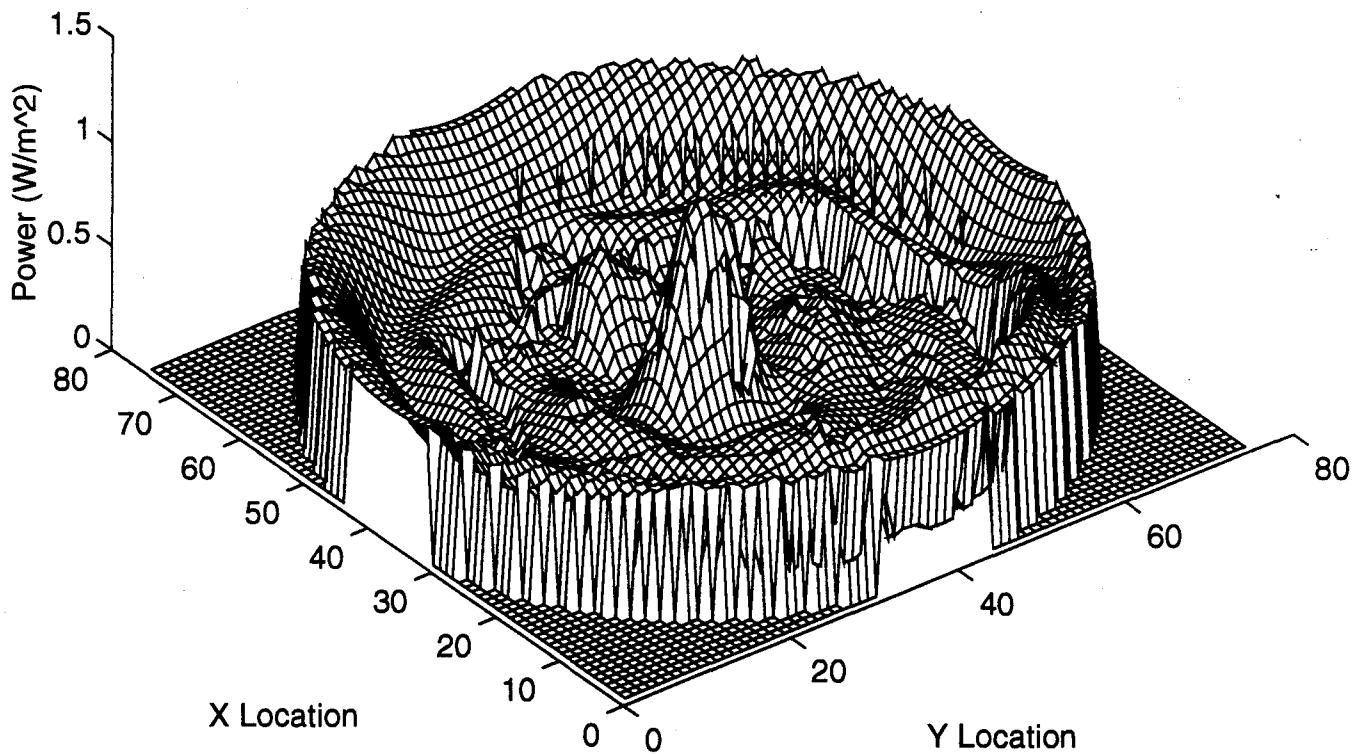
Figure 5.19: Power across the central XY plane of the simulation of a small head model with a muscle bolus (normalized to one at the center).

Horizontal cut of the small head with bone–like bolus at Z=38.
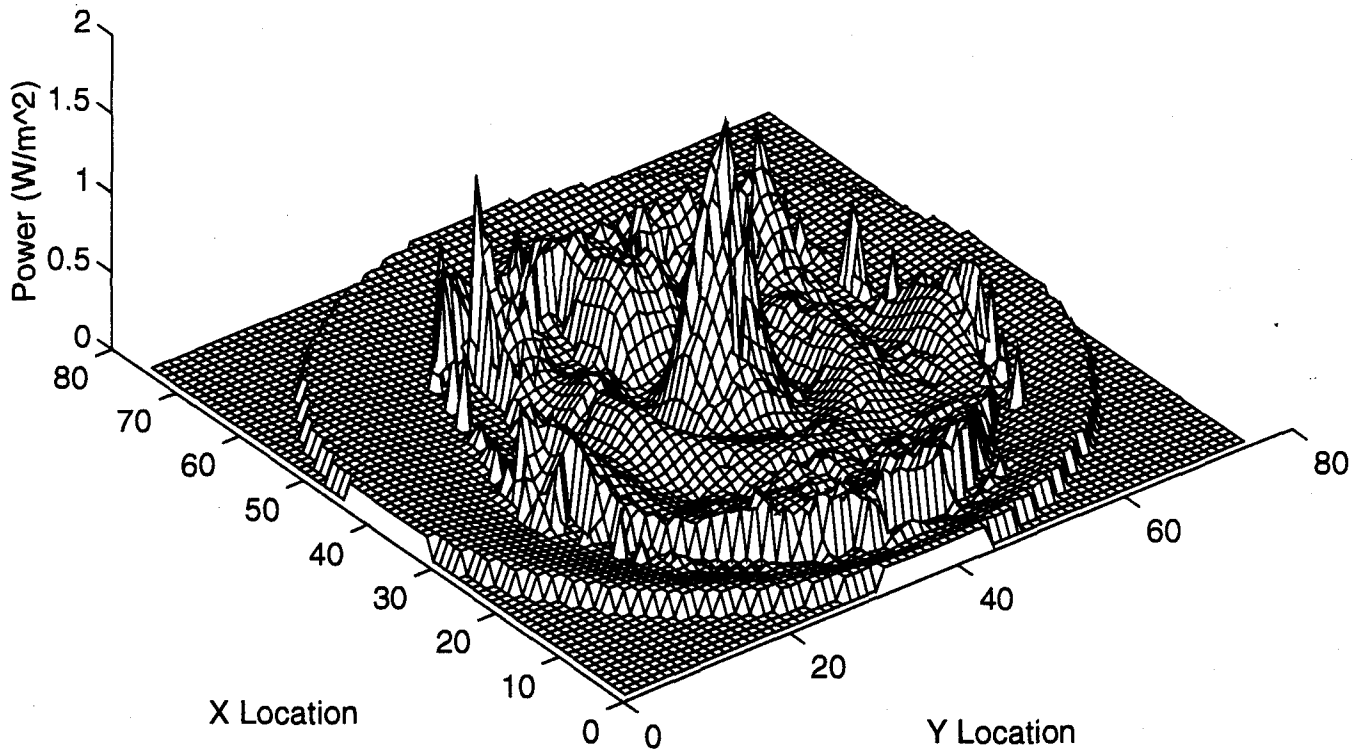
Figure 5.20: Power across the central XY plane of the simulation of a small head model with a bone bolus (normalized to one at the center).

Horizontal cut of the large head with muscle–like bolus at Z=38.
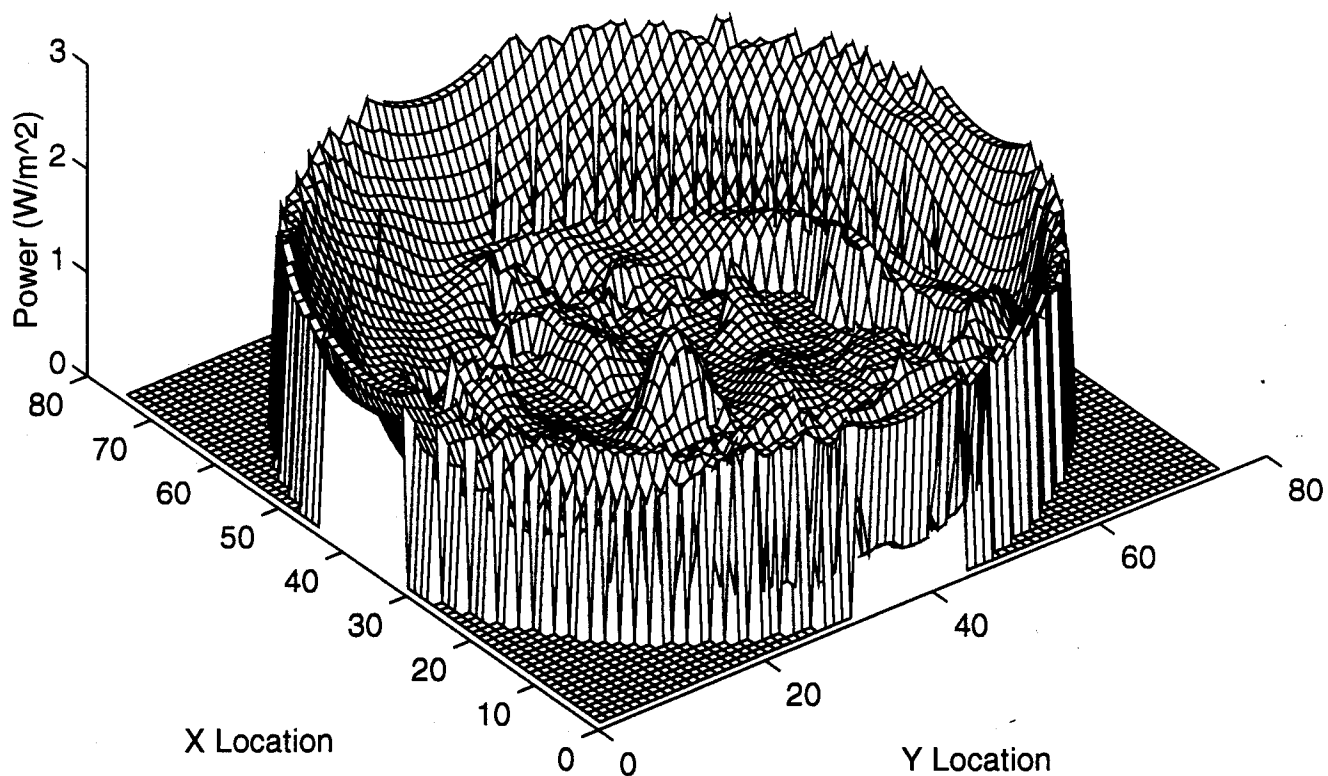
Figure 5.21: Power across the central XY plane of the simulation of a large head model with a muscle bolus (normalized to one at the center).
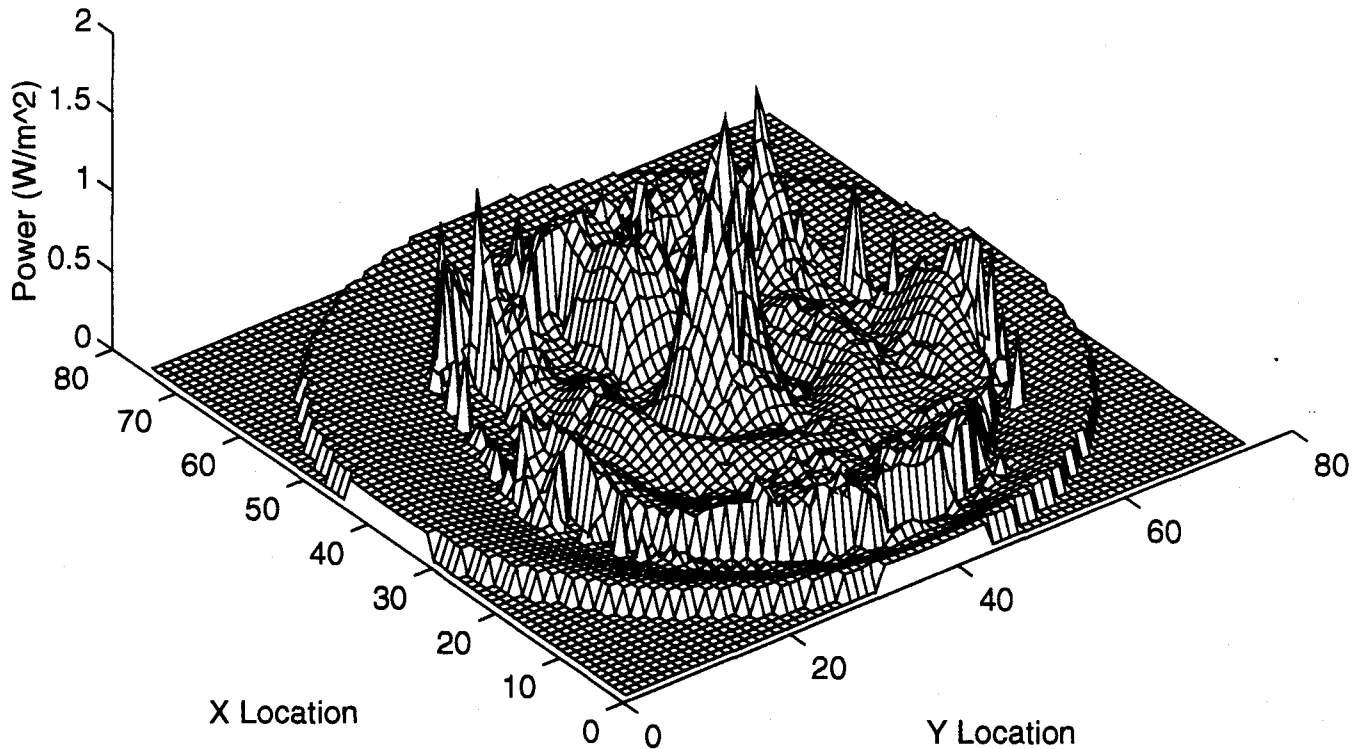
Figure 5.22: Power across the central XY plane of the simulation of a large head model with a bone bolus (normalized to one at the center).

Table 5.2 shows a comparison of the analysis statistics on each of the simulations. Center mean is a measure of the mean power in the center three-cell cube of the head. Because the power is normalized to one at the center, this will always be near one. The smaller it is, however, the more narrow the spike will be near the center, thereby producing a more accurate focusing. Total mean is a measure of the mean power everywhere else in the head. This does not include the power in the bolus because circulation of the bolus liquid can prevent overheating in the bolus. The lower this value, the smaller the risk will

70

be of over-heating undesirable locations. The third value in the table is the ratio of the mean power at the center to the total mean power. The higher this value, the easier it will be to heat the tumor without affecting healthy tissue. The final three numbers are percentages of cells over various thresholds. the first column gives the percent of cells with a value greater than 1. Each of these points will reach temperatures higher than the central tumor, thus destroying the healthy tissue at that location. It is preferable this number remains small. The next two are similar to this, however they are the percent of cells over .9 and .8 the power at the center. Although these points would not be raised to fatal temperatures, the high temperature levels may be dangerous to the healthy tissue.

Simulation	Cntr Mean	Total Mean	CM/TM	% cells over 1	% cells over .9	% cells over .8
Fat Head with Bone Bolus	.9910 (W/m^2)	2.946 (W/m^2)	.3364	72.7 %	75.9%	79.3%
Small Head with Bone Bolus	.8982 (W/m^2)	.2187 (W/m^2)	4.108	.26%	.39%	.58%
Small Head with Muscle Bolus	.8795 (W/m^2)	.1142 (W/m^2)	7.203	.01%	.05%	.08%
Full Head with Bone Bolus	.9057 (W/m^2)	.2942 (W/m^2)	3.078	1.66%	2.33%	3.32%
Full Head with Muscle Bolus	.8436 (W/m^2)	.2389 (W/m^2)	3.531	1.33%	2.0%	2.89%

Table 5.2: Statistics on the FDTD Head model simulations

Table 5.2 shows the muscle bolus is the preferred bolus type. However, as the head size becomes larger, the bolus composition becomes less important. This is because

71

the increased power necessary in the larger head models. The spikes are predominately introduced in the neck region. This is because the source distribution is abruptly turned off at the edge of the neck. Because there is an abrupt change in the source distribution from outside and inside the neck region, the field diffracts along the edge of the source distribution introducing the large spikes. The larger this discrepancy the larger the diffracted field spikes. In the small head models, the change in material characteristics in going from the bone of the bolus to the muscle of the neck has the predominate effect in introducing the diffracted field. In the larger head, the higher source power makes the stepped edge of the source power the larger contributor to the diffracted field. Figure 5.19 shows the power spikes in the neck for each of the four simulations.

In both cases, the muscle bolus produces a more precise heating pattern. This is because the optimization is designed around a muscle sphere. The phase of the source is designed for propagation through muscle. Passing through bone changes the velocity of the wave, thereby reducing the focusing, and smearing the central spike across a larger area.

6. Conclusions

This research provided seeral valueable insights into electromagnetic therapy as well presenting some important areas for further research. The final simulations on the complete head model illustrated the potential of microwave therapy. These simulations showed with proper optimization, it may be possible to irradiate a deep set tumor within a full size human head with adequate precision. The research also demonstrated the need for improved head modeling to ensure proper material characteristics are given to the tissue of the head.

6.1 Findings

FDTD proved to be an effective tool in this field of research. The initial simulations duplicating the optimal analytical solution derived by Rappaport demonstrated the validity of the FDTD numerical approach for treatment scenario.

The inhomogeneous simulations on laminated spheres demonstrated the effects inherent in an FDTD Approach. The stairstep approximation of a spherical surface introduced 'stairstep spikes' due to a locally horizontal surface along an otherwise vertical interface. In addition to these spikes, the FDTD approach proved to be difficult in obtaining complete coupling from the source to the sphere of treatment. These drawbacks not only demonstrate the effects of an FDTD approximations, but also introduce an area to be considered in microwave treatment. Because the head is not spherical, there will be horizontal sections of interface along what would otherwise be a vertical interface. For example, along the base of the mandible, there is a long vertical interface. In addition, along the inside of the occipital cavity there are vertical interfaces. All of these areas will be candidates for the 'stairstep spiking' phenomenom.

The simulations on the actual head models proved very encouraging. The results demonstrated a muscle-like bolus is preferred over a bone-like bolus. The muscle-like

bolus provided better precision as well as reduced spiking outside of the center. The source distribution placed around a small head within a spherical water bolus produced excellent focusing. There were only 20 cells above that at the center, all of which were confined to the neck region. This came about due to the stepped-edge of the source distribution near the neck. There was no taper down as the source neared the edge of the neck, thus a diffracted field was created near the edge of the source distribution creating several small, but strong spikes in the neck region.

These spikes are troubling, although not discouraging. As mentioned above, there was no attempt made to taper the edge of the field distribution, in addition the neck region itself was extremely approximate. The MRI scan produced no neck region, therefore the head was simply continued down from the base to the edge of the FDTD space. There was no spinal chord, esophagus, or trachea modeled. In addition, the head itself was approximated from an MRI scan. Although serving to produce an example of what could be possible in this area, it still needs a great deal of research and refinement.

The final head simulations showed it is possible to get good resolution at the center of an actual human head with minimal destruction to healthy tissue. With the addition of an optimization process, this precision can be furhter enhanced. This can also be used to reduce the unwanted fatal spikes in the neck region.

The simulations done on a full size head demonstrated two critical lessons. First, these are the first simulations to show FDTD can be used on a complete 3-D model of a human head in a treatment scenario. Second, and most important, these simulations show that even without any form of optimization to account for the inhomogeneous structure of the human head, it is possible to irradiate a deep-set tumor with decent precision.

6.2 Recommendations

The results obtained in this research shows an avenue for continued research in the field of microwave therapy. The simulations on the head model demonstrated the ability to

concentrate microwave energy in an actual head model. The results obtained thus far contain no optimization done based on the inhomogeneities of the head.

Several areas present themselves as prime candidates as a result of the simultations presented here. The most intuitively obvious of these follow-on oppurtunities is to derive a optimal source distribution taking into account the presence of the neck. The inability to place the source within the neck region requires some form of optimization in defining the taper. This can be done in several ways, by introducing a spatial filter or by customizing the spherical harmonics to concentrate the power near the top reducing it near the lower pole.

A comparison of the FDTD results to actual measurements of a real head also needs to be done. This research demonstrated FDTD's ability to duplicate analytic results. It was assumed the ability to model analytic homogeneous solutions implied the ability to model inhomogeneous geometries. A simulation of these solutions compared to actual measurements is needed to further prove this method is a valid modeling tool.

Another area open for research is in developing a more accurate modeling system for creating the head mesh. The head mesh used in this research is only an approximate rendering of an MRI scan. The method used to model the brain has no connection to the actual electrical charateristics of the that individual's head tissue. The parameters used were 'typical' values for average tissue. The actual properties in real tissue vary immensely from individual to individual. For this reason, a system is needed to non-invasively measure material parameters of the head region.

This research serves to illustrate the potential inherent in microwave treatment. The results show that electromagnetic field propagation can be predicted in an inhomogeneous, three-dimensional scenario. In addition, the resutls show that good penetration and precision can be obtained in an actual human head with proper optimization. This research clearly indicates the need for continued research in the area of microwave hyperhtermia of cancerous tissue.

Appendix A: The Vector Wave Equation in Spherical Coordinates

The source optimization developed by Rappaport and Morganthaler is based upon solution to the wave equation in the spherical coordinate system. The geometry of this coordinate system is shown in figure 2.1. Before discussing this optimization it is important to go over the basics of the solution to the spherical vector wave equation.
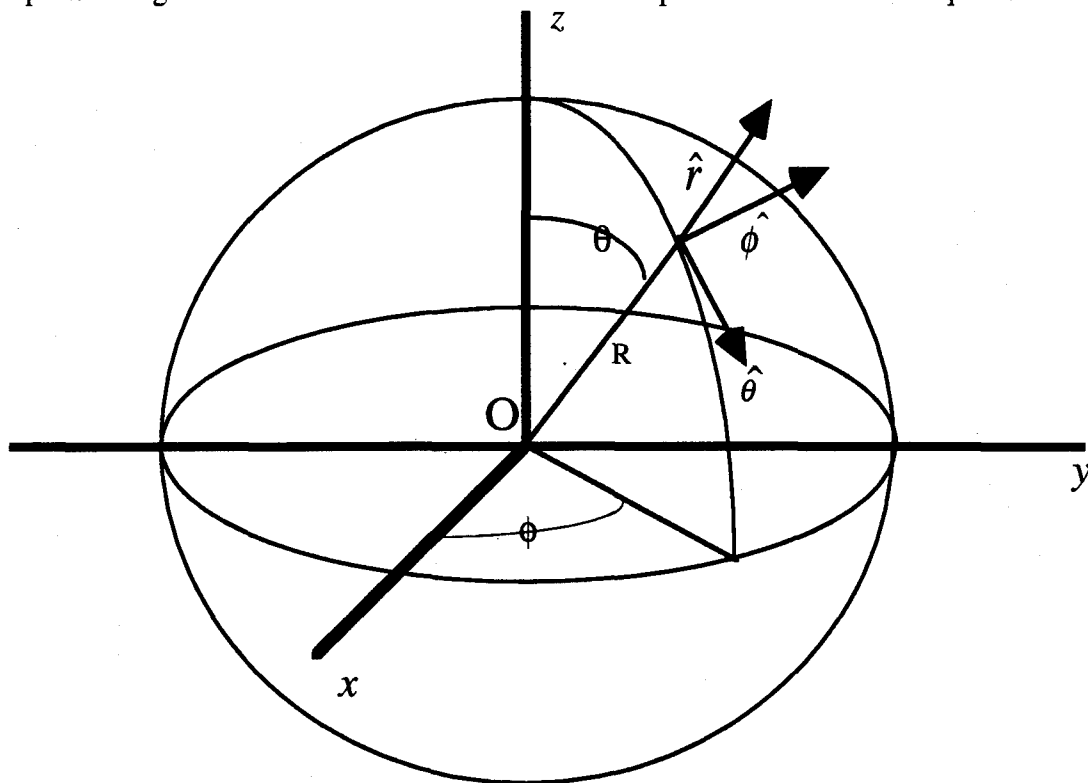
Figure A.1: The Spherical coordinate system as used in this thesis

Solution to the Spherical Vector Wave Equation

Any electromagnetic wave in an isotropic, homogeneous, source free region must satisfy the vector wave equation [10]

$$\nabla^2 C - \mu\varepsilon \frac{\partial^2 C}{\partial t^2} - \mu\sigma \frac{\partial C}{\partial t} = 0. \qquad (1)$$

Where C represents a field vector (E, B, D, or H) and μ, ε, and σ represent permeability, permittivity and electrical conductivity as usual. The analysis presented here will deal exclusively with the electric and magnetic field intensities, E and H. The linearity of this equation allows the vectors E and H to be expanded by Fourier analysis into time harmonics of the form $C = \sum Ce^{-i\omega t}$ with no loss in generality. This allows the entire time dependence to be expressed as $e^{-i\omega t}$ and will be left out in the interest of clarity. If it is then noted that $\nabla^2 C = \nabla\nabla \cdot C - \nabla \times \nabla \times C$ and that $\varepsilon\mu\omega^2 + i\sigma\mu\omega = k^2$, eq (1) can be rewritten as

$$\nabla\nabla \cdot C - \nabla \times \nabla \times C + k^2 C = 0. \qquad (2)$$

There exists a solution set to equation (2) containing three forms of waves, a longitudinally polarized wave and two transverse waves commonly referred to as transverse electric (TE) and transverse magnetic (TM) waves dependent upon whether the magnetic or electric field is tangential to the direction of propagation (in this case along a radial line from the center of the sphere of interest). This thesis is based only on the electric field solution for a TM wave.

To find an expression for the TM wave, we will look for a magnetic field solution to (2) of the form

$$H = \nabla \times \left(\hat{r}\, u(R)\psi \right) \qquad (3)$$

Where $u(R)$ is a function of R yet to be determined and ψ is a scalar function of R, θ, and ϕ and a solution to the equation

$$\nabla^2 \psi + k^2 \psi = 0. \qquad (4)$$

Employing the del operator of the spherical coordinate system, the three components of H can be written as

$$H_r = 0, \qquad H_\theta = \frac{1}{R\sin\theta} \frac{\partial}{\partial \phi}(u\psi), \qquad H_\phi = -\frac{1}{R} \frac{\partial}{\partial \theta}(u\psi) \qquad (5)$$

The divergence of the cross product of any two vectors is identically zero, thus the divergence of **H** will be zero and (2) can be rewritten as

$$\nabla \times \nabla \times \mathbf{H} - k^2 \mathbf{H} = 0. \qquad (6)$$

Expanding this out in spherical coordinates reveals that the $\hat{r}$ component is identically zero and the $\hat{\theta}$ component is satisfied by the equation

$$\frac{1}{R^3 \sin^2 \theta}\left[\frac{\partial^2}{\partial \theta \partial \phi} \sin \theta \frac{\partial}{\partial \theta}(u\psi) \right] + \frac{1}{R^3 \sin^3 \theta} \frac{\partial^3}{\partial \phi^3}(u\psi) +$$
$$\frac{1}{R\sin \theta} \frac{\partial^3}{\partial r^2 \partial \phi}(u\psi) + \frac{k^2}{R} \frac{\partial}{\partial \theta}(u\psi) \qquad (7)$$

The $\hat{\phi}$ component is satisfied by the equation

$$\frac{\partial}{\partial \theta} \frac{1}{R^3 \sin \theta}\left[\frac{\partial}{\partial \theta} \sin \theta \frac{\partial}{\partial \theta}(u\psi) \right] + \frac{\partial}{\partial \theta} \frac{1}{R^3 \sin^2 \theta} \frac{\partial^2}{\partial \phi^2}(u\psi) +$$
$$\frac{1}{R} \frac{\partial^3}{\partial r^2 \partial \theta}(u\psi) + \frac{k^2}{R} \frac{\partial}{\partial \theta}(u\psi) \qquad (8)$$

Both eq(7) and eq(8) will be satisfied by the equation

$$\frac{\partial^2}{\partial r^2}(u\psi) + \frac{1}{R^2 \sin \theta} \frac{\partial}{\partial \theta}\left[\sin \theta \frac{\partial}{\partial \theta}(u\psi) \right] + \frac{1}{R^2 \sin^2 \theta} \frac{\partial^2}{\partial \phi^2}(u\psi) + k^2 u\psi = 0. \quad (9)$$

If we know take a look at the requirement placed on ψ by eq (4); expanding that equation yields

$$\frac{1}{R^2} \frac{\partial}{\partial r}\left(r^2 \frac{\partial \psi}{\partial r} \right) + \frac{1}{R^2 \sin \theta} \frac{\partial}{\partial \theta}\left(\sin \theta \frac{\partial \psi}{\partial \theta} \right) + \frac{1}{R^2 \sin^2 \theta} \frac{\partial^2 \psi}{\partial \phi^2} + k^2 \psi = 0. \qquad (10)$$

When this is done, it immediately becomes apparent that if we let $u(R)=R$ eq. (5) will be satisfied.

This shows one solution to the vector wave equation is given by **H** whose components are

$$\mathbf{H}_r = 0, \qquad \mathbf{H}_\theta = \frac{1}{\sin \theta} \frac{\partial \psi}{\partial \phi}, \qquad \mathbf{H}_\phi = -\frac{\partial \psi}{\partial \theta}. \qquad (11)$$

The optimization is based upon the electric field solution to a TM wave which can easily be found from the relation

$$k\mathbf{E} = \nabla \times \mathbf{H}. \qquad (12)$$

Which produces an electric field of the form

78

$$E_r = \frac{1}{k}\frac{\partial^2(R\psi)}{\partial R^2} + k^2 R\psi, \qquad E_\theta = \frac{1}{kR}\frac{\partial^2(R\psi)}{\partial R\partial\theta}, \qquad E_\phi = \frac{1}{kR\sin\theta}\frac{\partial^2(R\psi)}{\partial R\partial\phi} \qquad (13)$$

Solution for the Elementary Wave Function

Those paying attention will be quick to point out that this expression for the electric field means absolutely nothing without an expression for ψ. You will remember this variable was introduced as the solution to the scalar wave equation (4) in spherical coordinates. In order to find this solution, start with the assumption that it can be written as

$$\psi = f(R,\theta,\phi)e^{-i\omega t}. \qquad (14)$$

Which will result in no loss of generality if the time dependence is left out as described earlier.

Therefore, in a homogeneous isotropic medium, the function f must satisfy the scalar wave eq (4) which, when expanded, looks like eq (10). If f can be written as $f = f_R(R)f_\theta(\theta)f_\phi(\phi)$, then eq(10) is separable into

$$R^2\frac{d^2 f_R}{dR^2} + 2R\frac{df_R}{dR} + (k^2 R^2 - p^2)f_R = 0 \qquad (15)$$

$$\frac{1}{\sin\theta}\frac{d}{d\theta}\left(\sin\theta\frac{df_\theta}{d\theta}\right) + \left(p^2 - \frac{q^2}{\sin^2\theta}\right)f_\theta = 0 \qquad (16)$$

$$\frac{d^2 f_\phi}{d\phi^2} + q^2 f_\phi = 0 \qquad (17)$$

Where p and q are introduced as variables of separation yet to be determined. Since we are working in a homogeneous, isotropic medium, the properties of the medium will be independent of equatorial angle ϕ. In addition, it is physically impossible for a field to have two different values at the same point in space, therefore eq(17) must be periodic function of ϕ with a period of 2π. To avoid the complications involved in introducing a complex function, set $f_\phi = \frac{\cos m\phi}{\sin m\phi}$. Thus, q must be an integer of the form

m=0,±1,±2,....

Finding a value for q is slightly more complicated. To find this solution, start by noting the remarkable resemblance of eq (16) to the associated Legendre equation [11]

$$\frac{1}{\sin\theta}\frac{d}{d\theta}\left(\sin\theta\frac{dP_n^m(\cos\theta)}{d\theta}\right) + \left[n(n+1) - \frac{m^2}{\sin^2\theta}\right]P_n^m(\cos\theta) = 0 \quad (18)$$

In fact, if we set $p^2 = n(n+1)$, where n=0,1,2... we have the same equation, if f_θ is an associated Legendre polynomial of the form

$$f_\theta(\theta) = P_n^m(\cos\theta) = \left(1 - \cos^2\theta\right)^{m/2}\frac{d^m}{d\cos^m\theta}P_n(\cos\theta). \quad (19)$$

This all works out mathematically but it is also important to understand it physically. f_θ must be periodic in theta with a period of 2π, symmetric about π, single valued and finite for this to physically make sense. Since we are defining the Legendre function as a function of $\cos\theta$, it will be periodic in theta with a period of 2π and symmetric about π. Examining the definition in eq(19) it quickly becomes apparent that the associated Legendre function will be zero at ± 1, and single-valued and finite everywhere in between. With this, p and q have been determined as well as solutions for $f_\theta(\theta)$ and $f_\phi(\phi)$.

The final step is to determine a solution for $f_R(R)$. This stems from the solution to eq (15) with p^2 replaced by $n(n+1)$. In addition, if $f_R(R)$ is replaced by $f_R(R) = kR^{-\frac{1}{2}}v(R)$ eq (15) can be put in the form

$$R^2\frac{d^2v}{dR^2} + R\frac{dv}{dR} + \left[k^2R^2 - \left(n+\frac{1}{2}\right)^2\right]v = 0 . \quad (20)$$

Thus, $v(R)$ is given by a cylindrical Bessel function of half order. From this the radial dependence can be given as

$$f_R(R) = \frac{1}{\sqrt{kR}}J_{n+\frac{1}{2}}(kR) \quad (21)$$

This is actually a much simpler equation to employ than the cylindrical Bessel function. Because of its frequent occurrence, this is redefined as a spherical Bessel function.

$$j_n(kR) = \frac{1}{\sqrt{kR}}J_{n+\frac{1}{2}}(kR). \quad (22)$$

Which leaves the final form of the elementary wave function as

80

$$f_{\substack{e \\ o \\ mn}} = j_n(kR)P_n^m(\cos\theta)\,\frac{\cos}{\sin}\,m\phi. \quad (23)$$

This equation can then be placed back into the solution for the E-field to give the final

equation for the solution to the spherical vector wave equation.

$$\mathbf{E}(R,\theta,\phi) = \left(\frac{1}{k}\frac{\partial^2\left(Rf_{\substack{e \\ o \\ mn}}\right)}{\partial R^2} + k^2 R\psi \right)\hat{r} + \left(\frac{1}{kR}\frac{\partial^2\left(Rf_{\substack{e \\ o \\ mn}}\right)}{\partial R\partial\theta} \right)\hat{\theta} + \left(\frac{1}{kR\sin\theta}\frac{\partial^2\left(Rf_{\substack{e \\ o \\ mn}}\right)}{\partial R\partial\phi} \right)\hat{\phi} \quad (24)$$

Appendix B: Power Across Full Head with Bone Bolus

This appendix contains selected power profiles across the full head with bone tissue simulation. The slices were selected to show a good representation of the power profile near the center along with a basic view of the power near the edges. Note most spiking occurs in the neck region with a little along the outside skin surface.

Coronal Cut Through the Head Model at X=38.
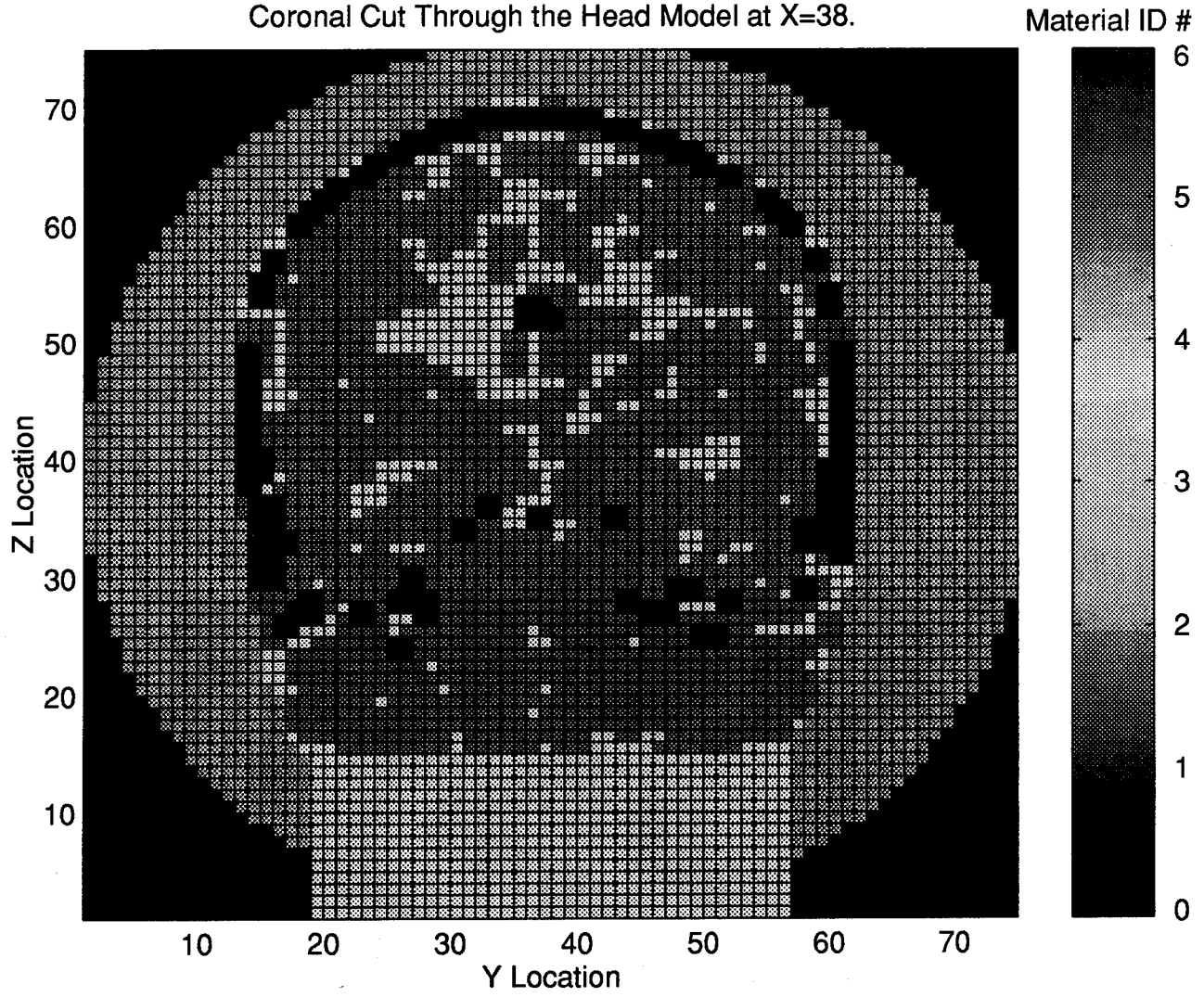
Power at X=12.
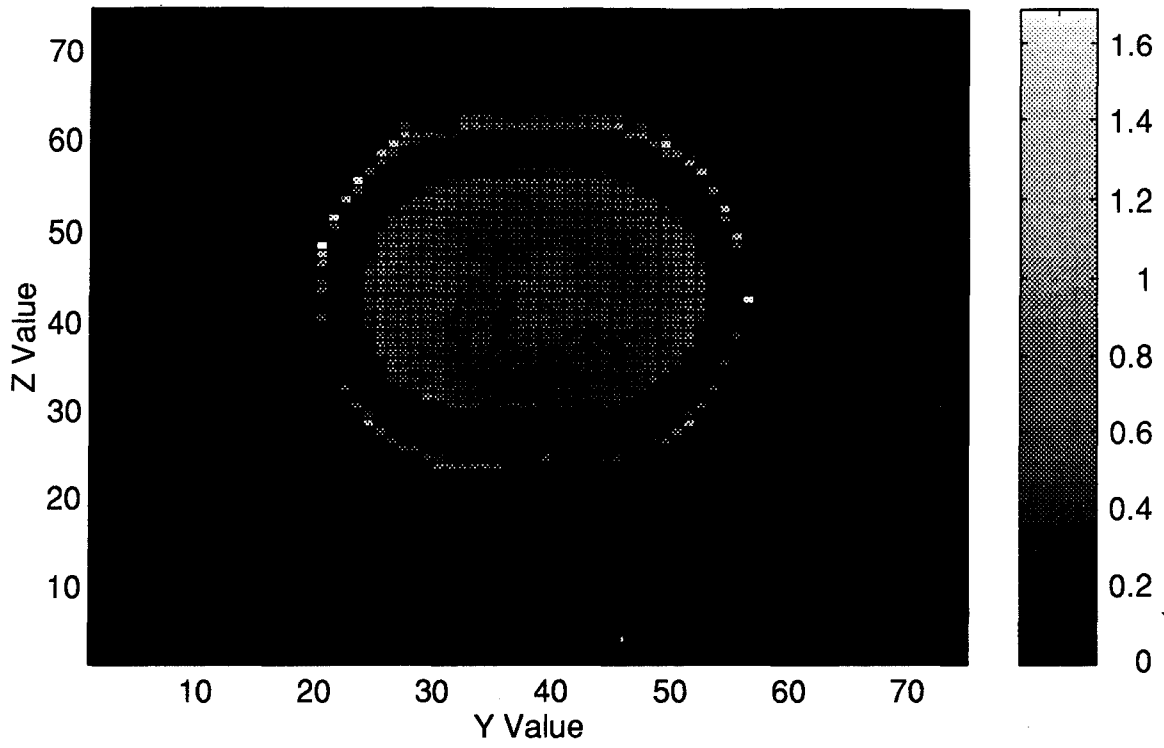
Power at X=16.
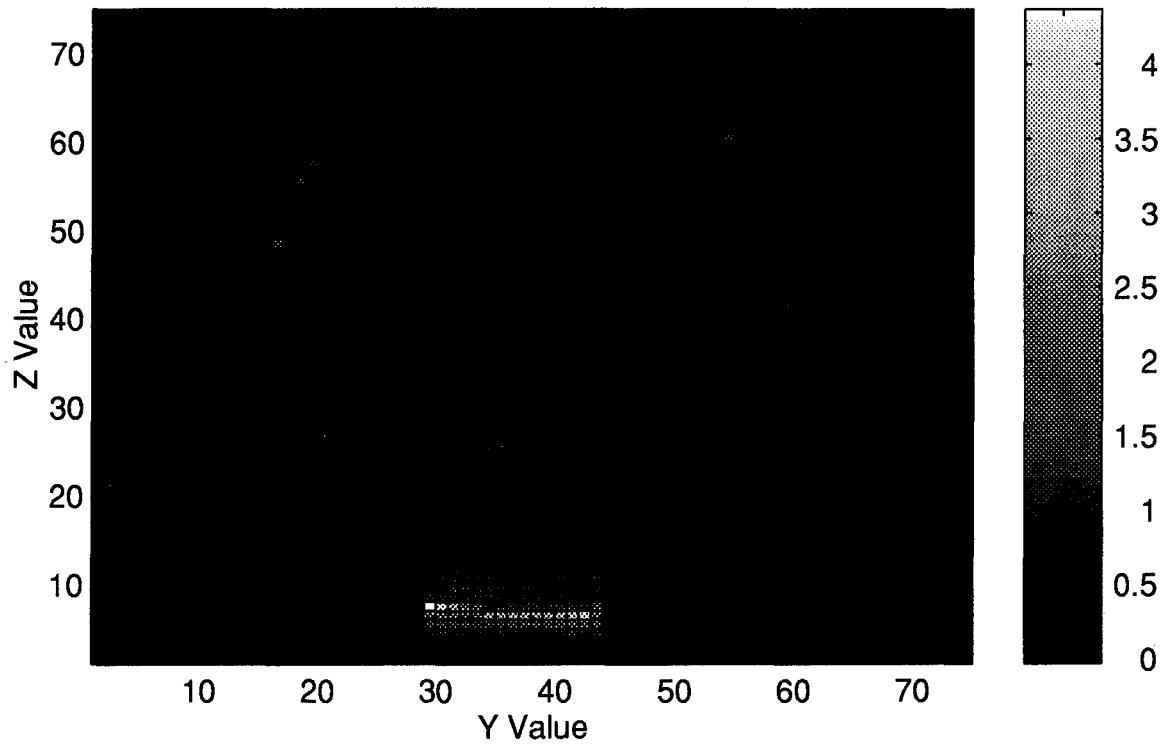
Power at X=20.
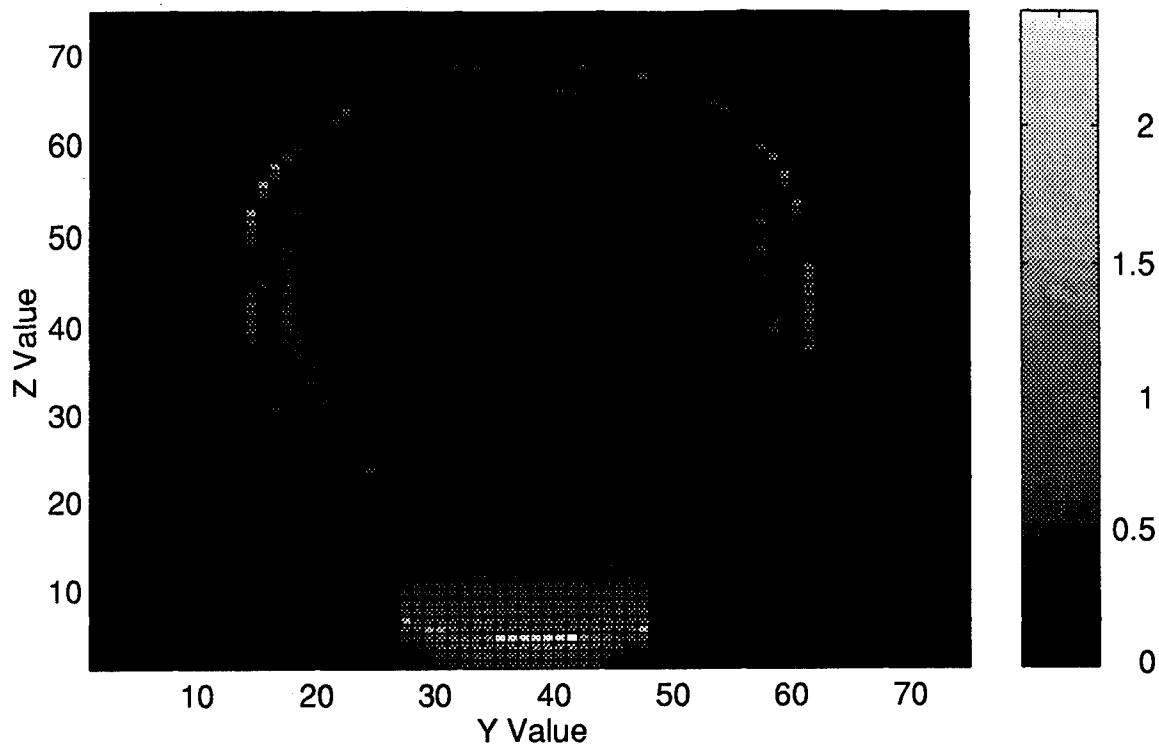
Power at X=24.
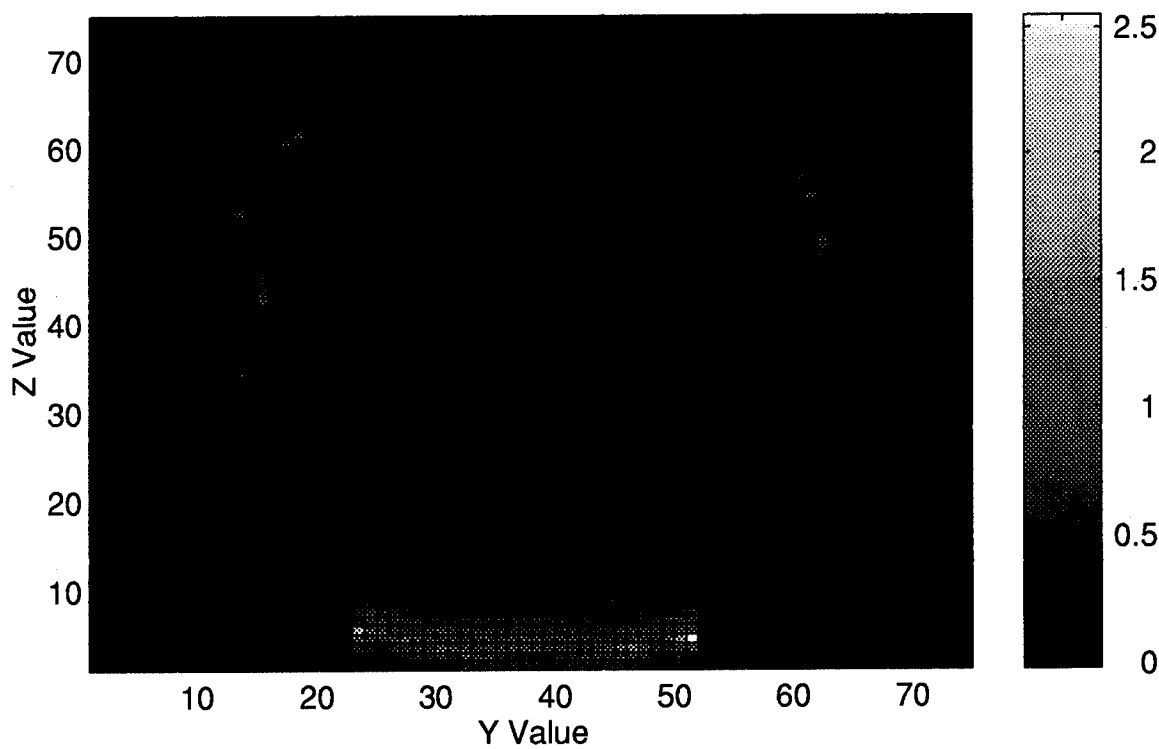
Power at X=28.
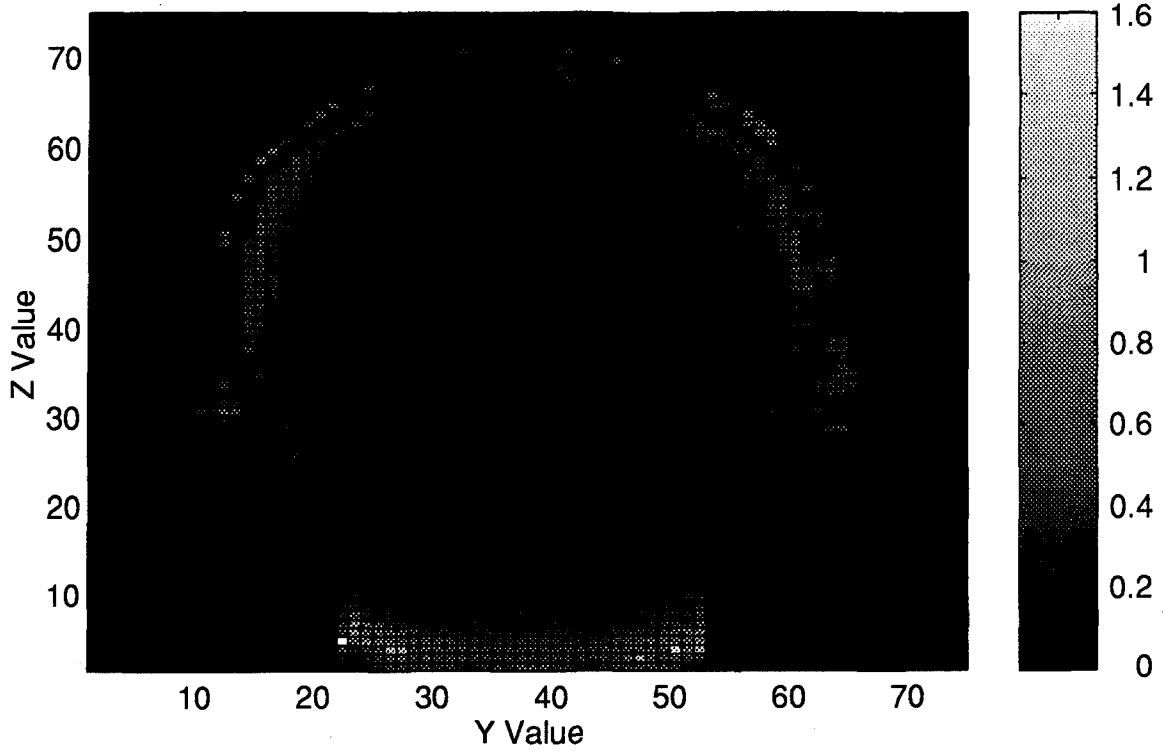
Power at X=32.
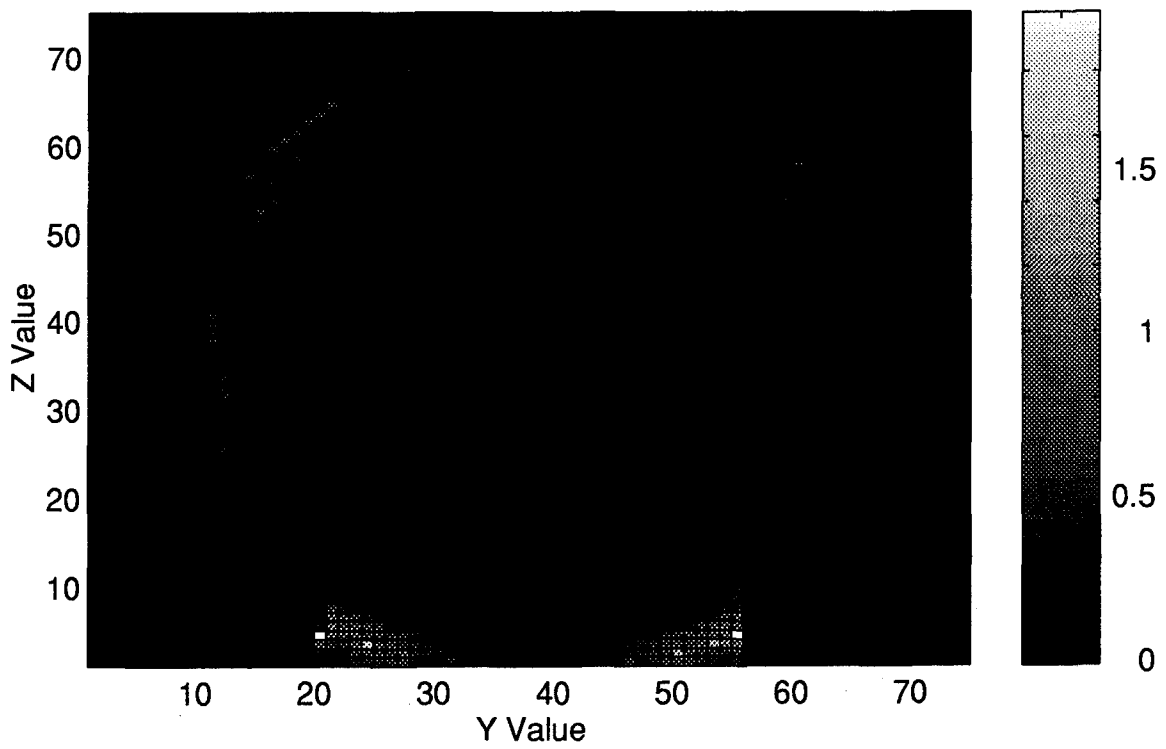
Power at X=34.
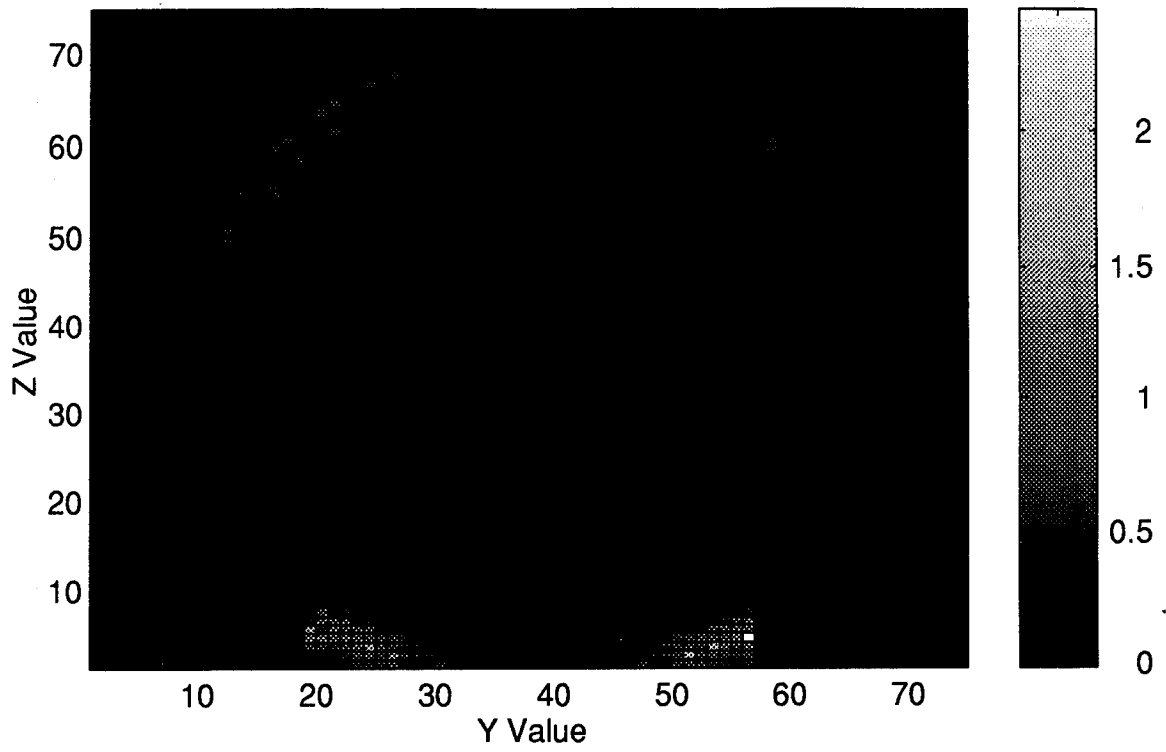
Power at X=36.
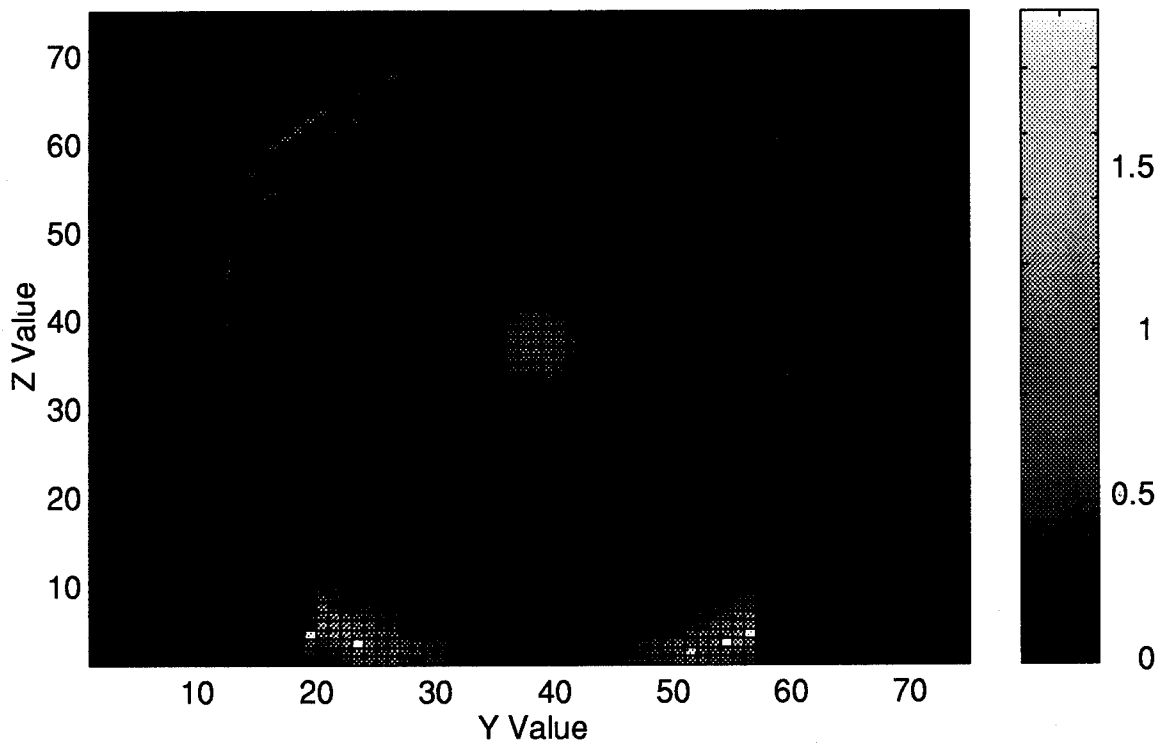
Power at X=37.
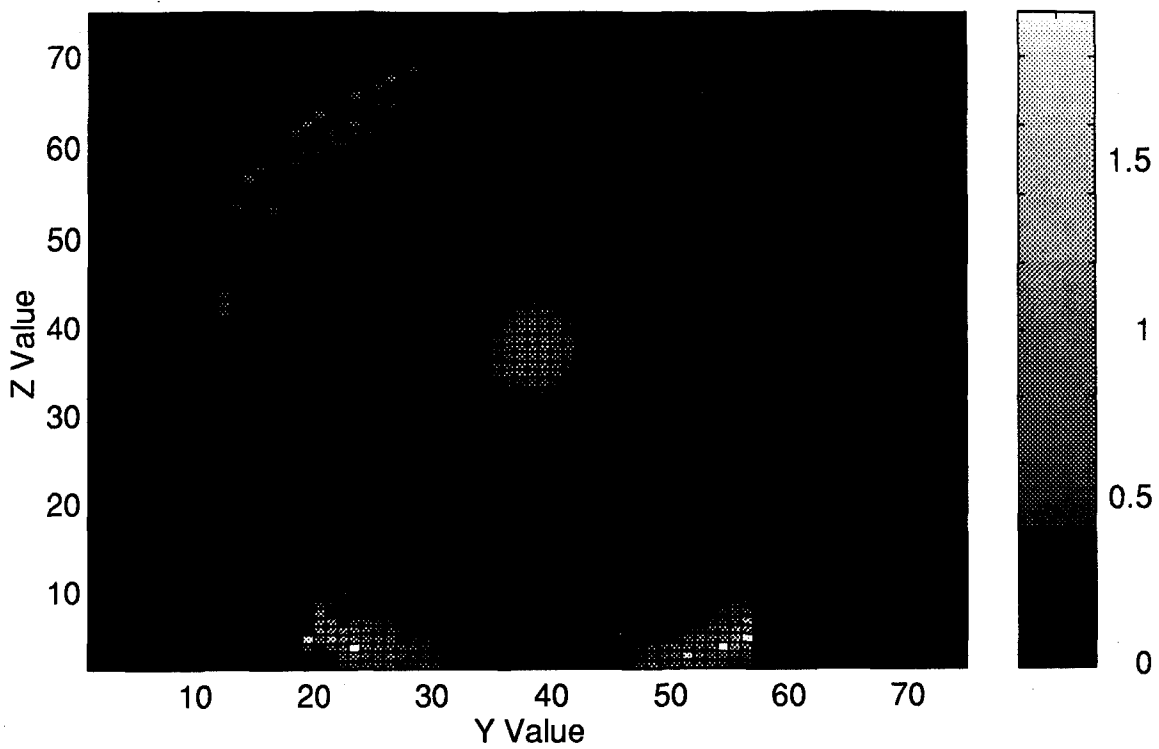
Power at X=38.
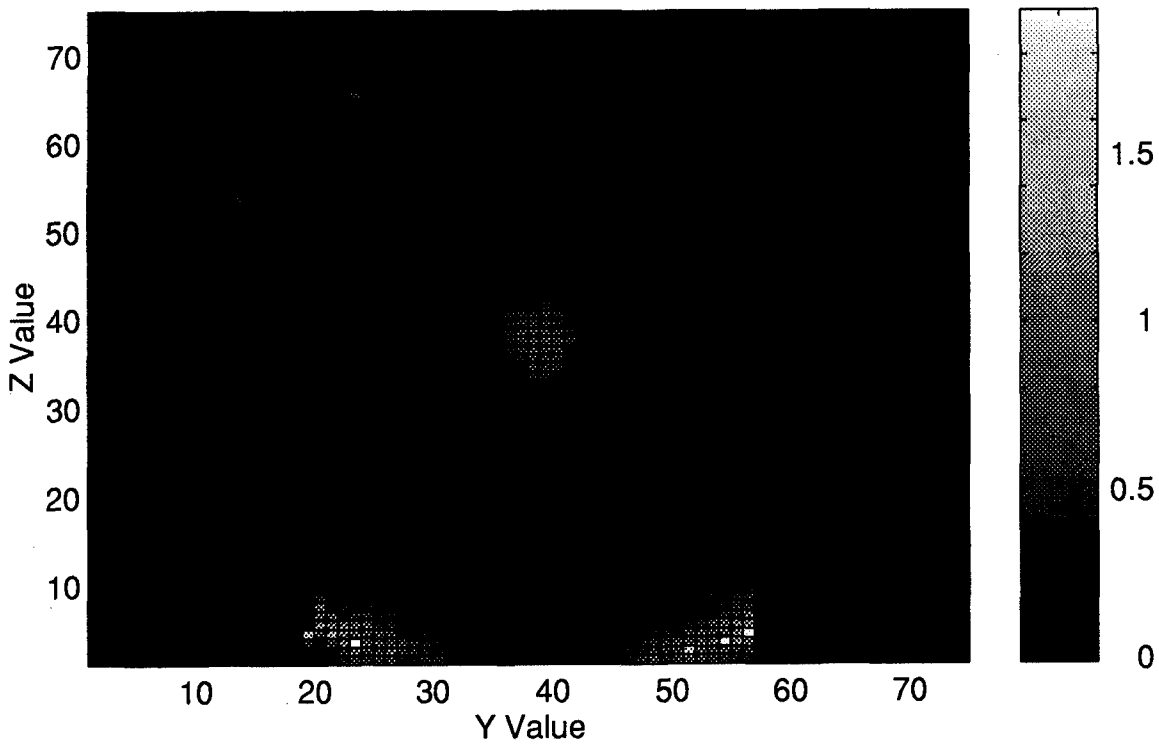
Power at X=39.
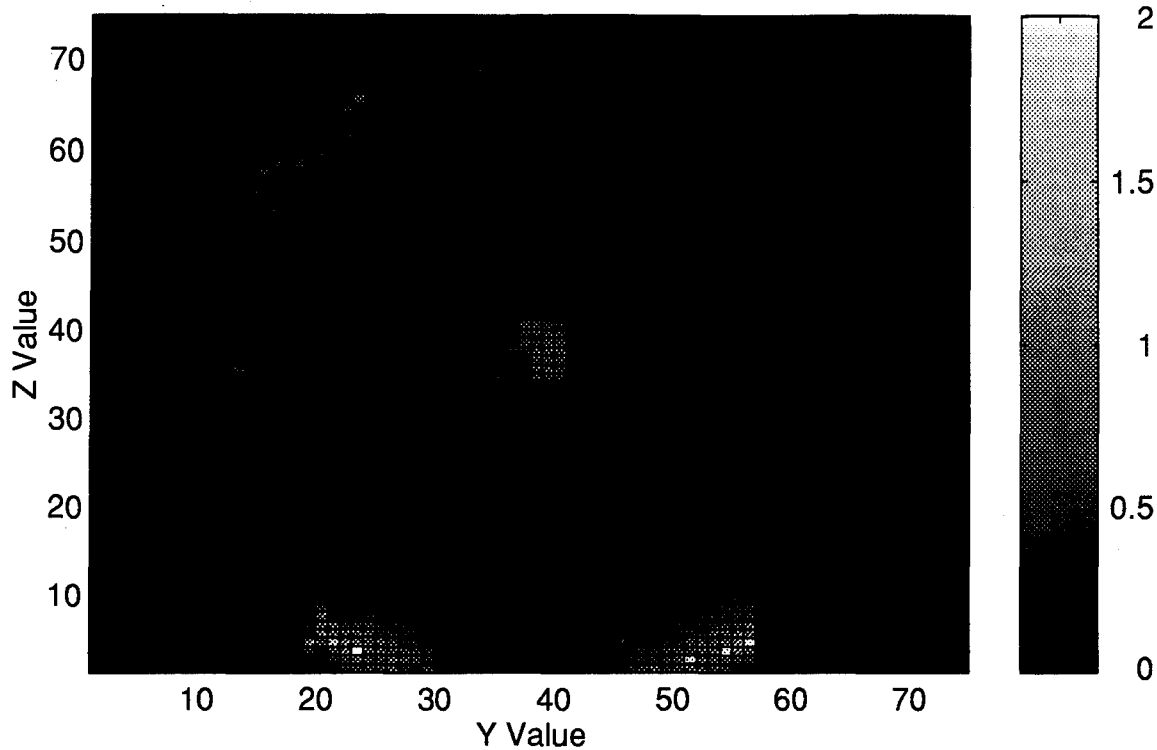
Power at X=40.
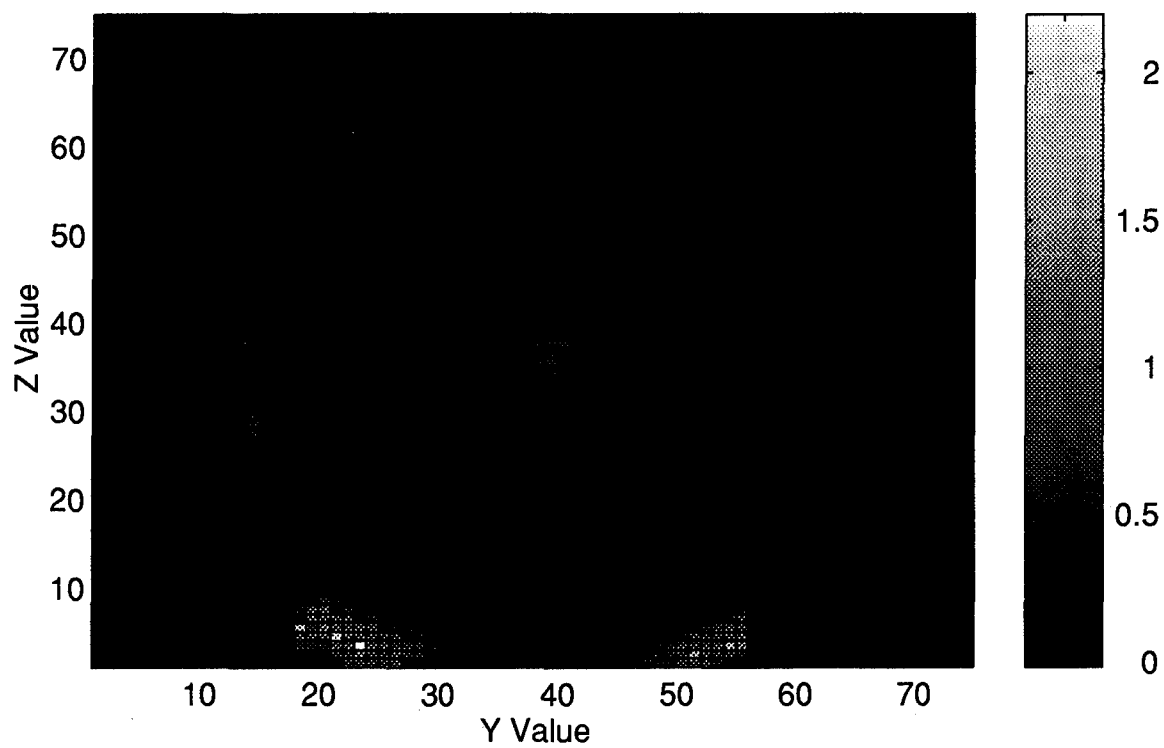
Power at X=42.
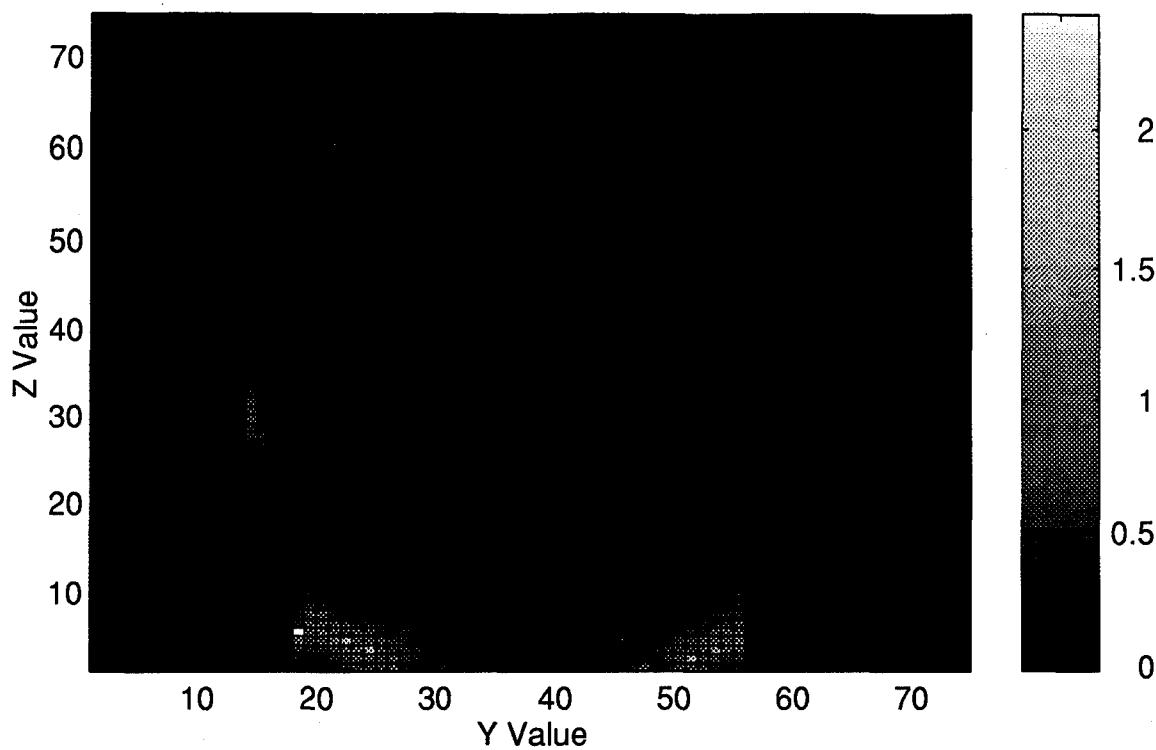
Power at X=44.
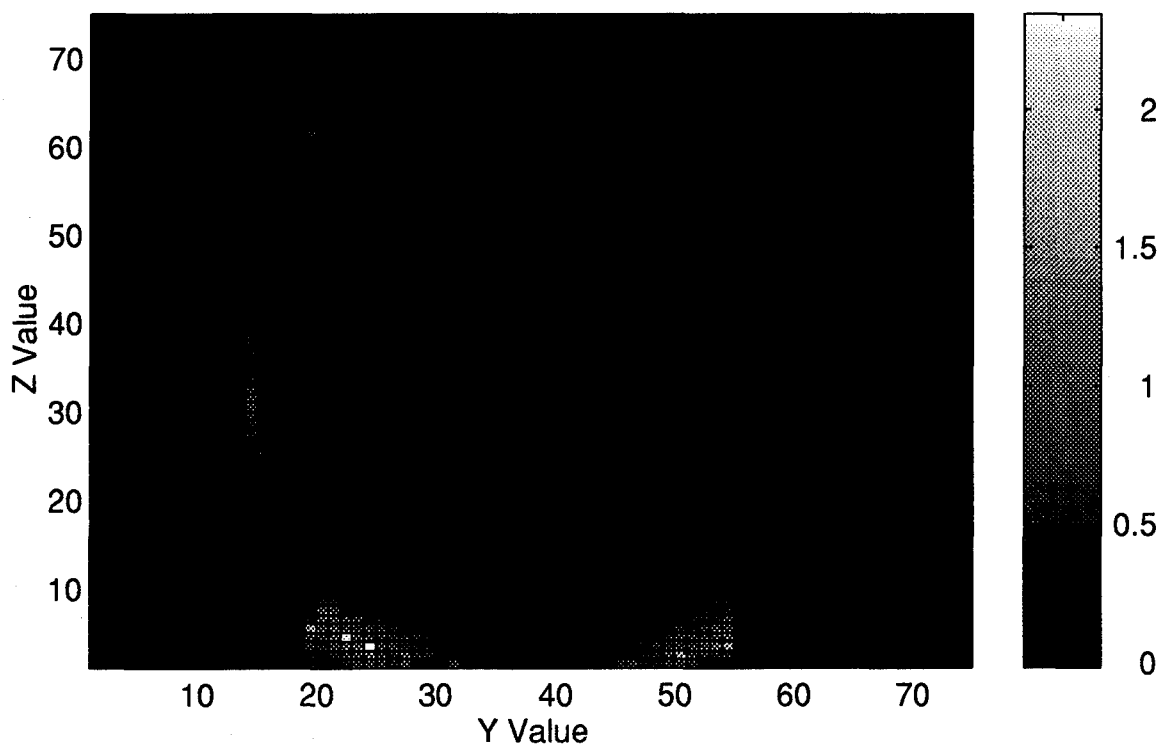
Power at X=48.
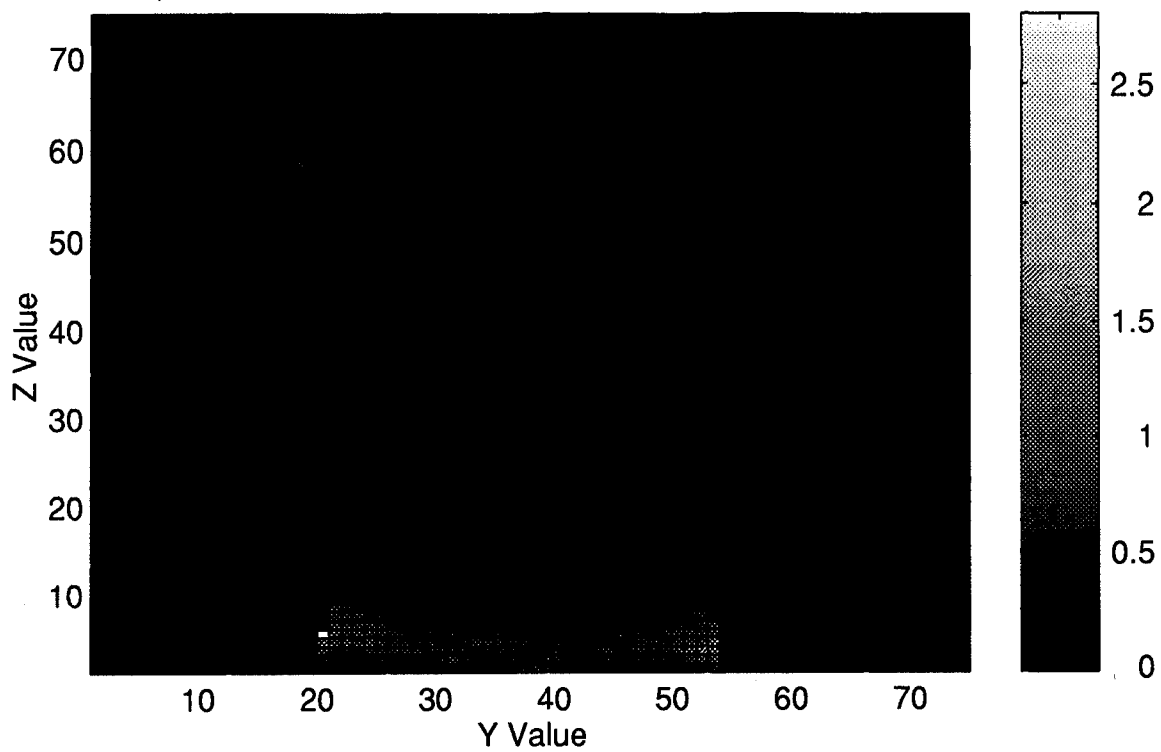
Power at X=52.
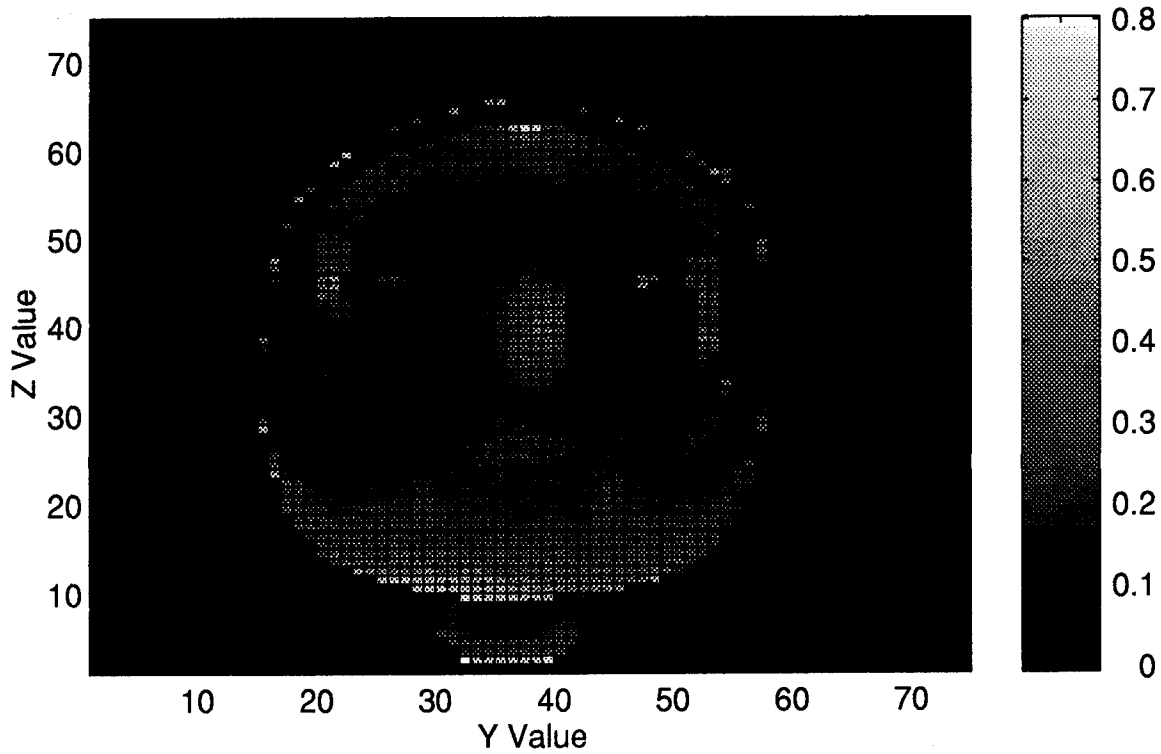
Power at X=56.
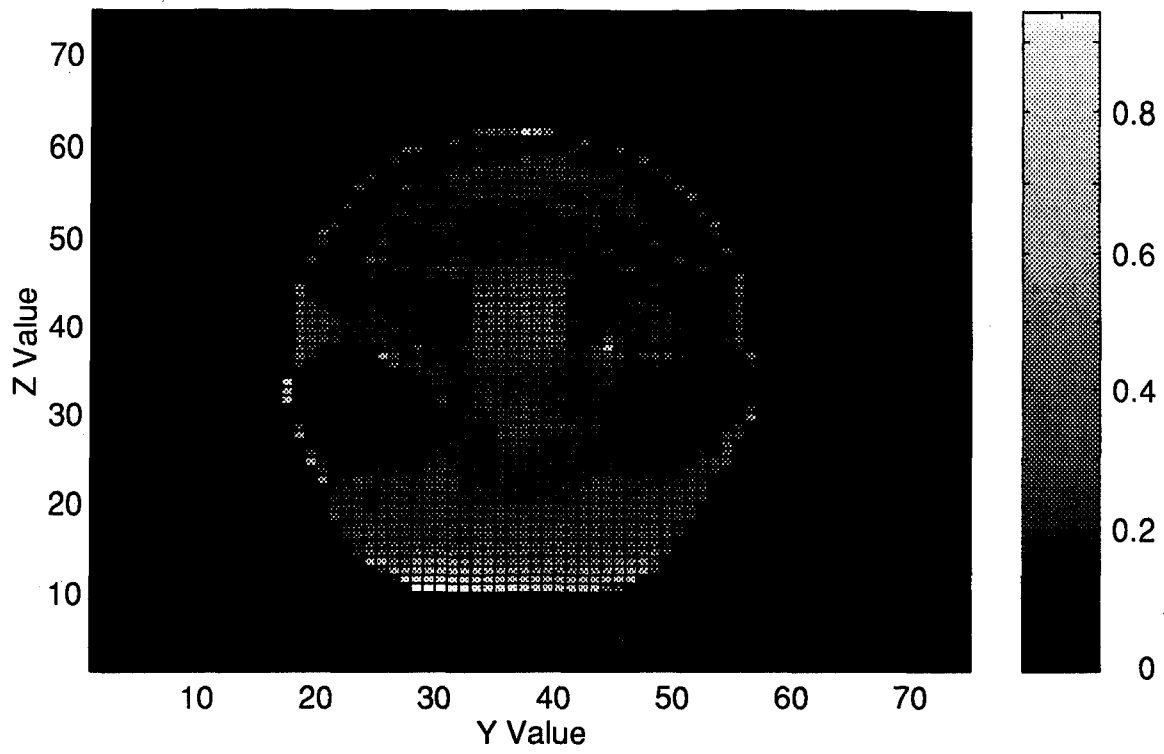
Power at X=60.
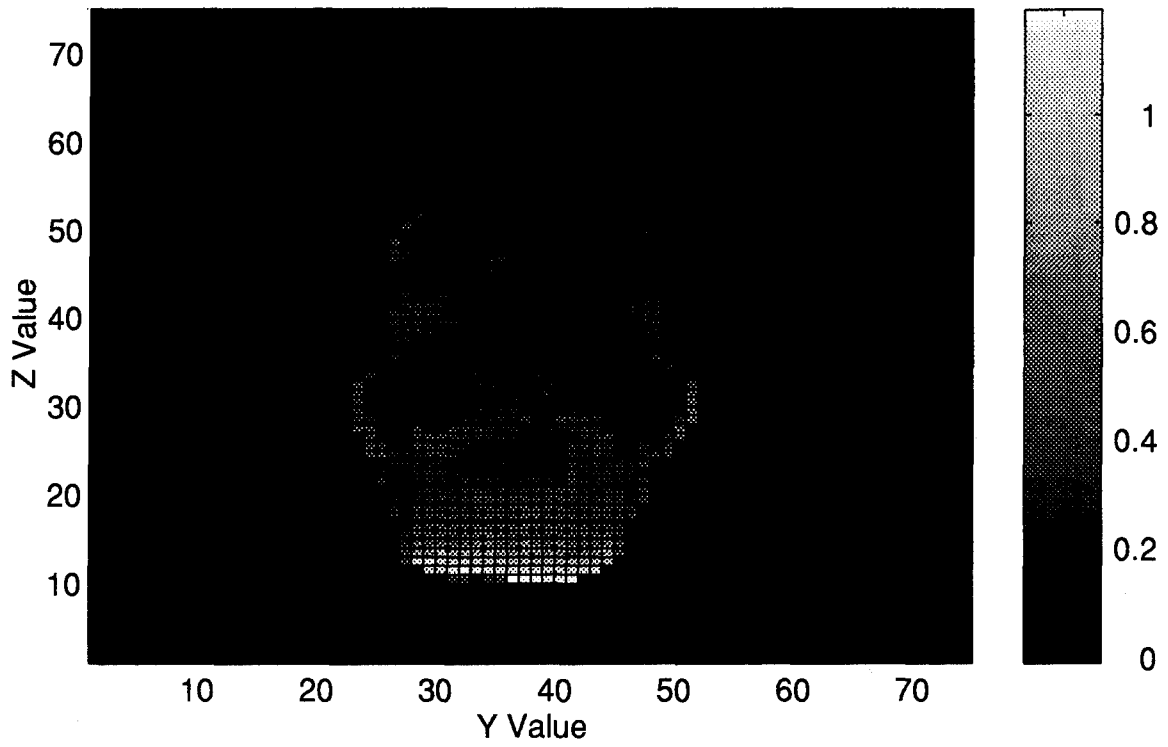
Power at X=64.
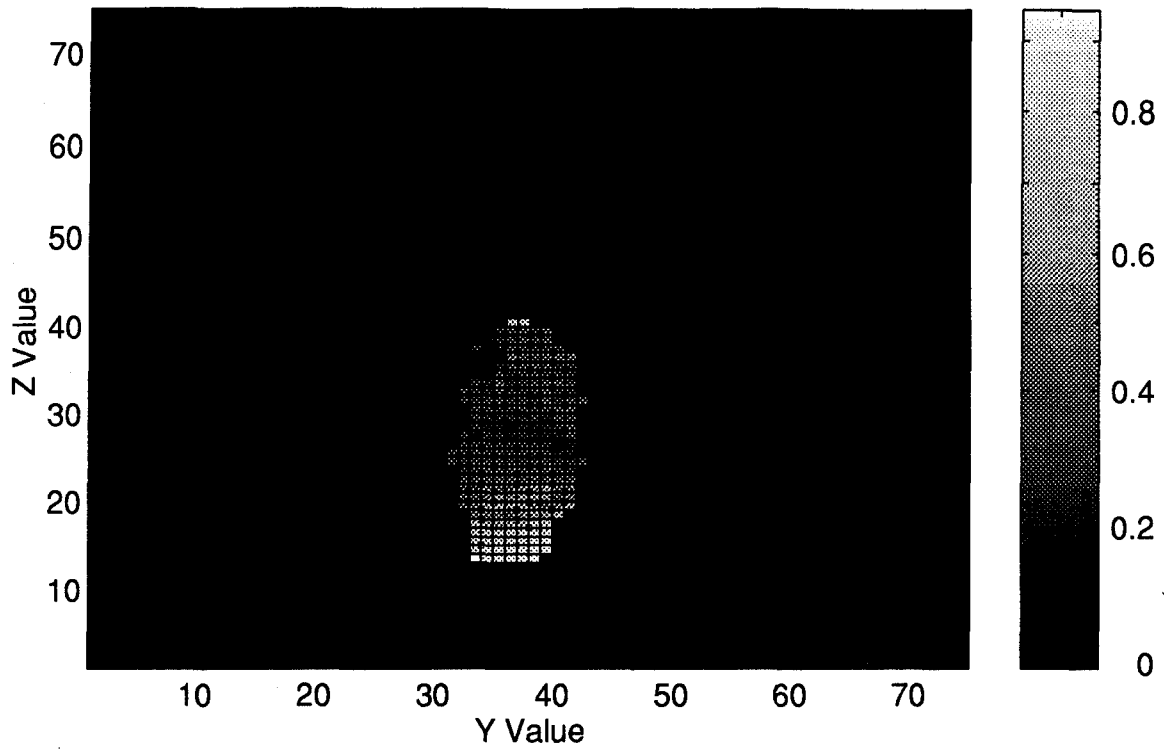
Power at X=68.
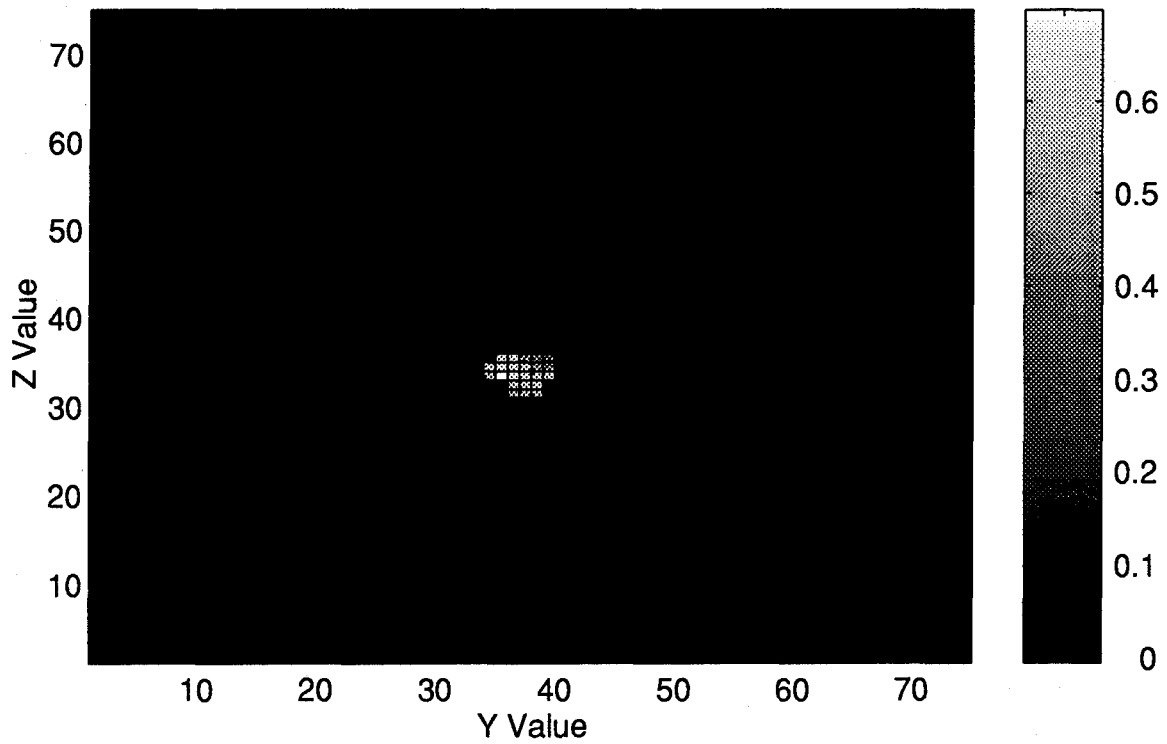
Appendix C: FORTRAN Programs

ANALYTIC.F code

```
      PROGRAM Analytic
C     This program computes the exact field distribution for
a sphere
C     of tissue with a given epsr and sigma
      INTEGER COUNT,I,J,K,RADIUS,I
      COMPLEX JN,EFLDR,EFLDT
      REAL THETA,PHI,PI,ICNTR,JCNTR,KCNTR
      EXTERNAL JN, PN


C *** INITIALIZE *** C
      PI=ACOS(-1.)
      COUNT=0

      CELLSIZE=.002554
      ICNTR=38
      KCNTR=37.5
      JCNTR=38
      RADIUS=37

      OPEN(15,file='analytic.dat',status='unknown')
      DO 163 I=1,75
      WRITE(6,*) 'I=',I
        DO 162 J=1,75
          DO 161 K=1,75
C
            R=SQRT((I-ICNTR)**2.+(J-JCNTR)**2.+(K-KCNTR)**2.)
            R=R*CELLSIZE
            IF (R.LT.0.003) R=.003
            THETA=ATAN2((SQRT((I*1.-ICNTR)**2
     &          +(J*1.-JCNTR)**2)),(K*1.-KCNTR))
```

94

```
              PHI=-PI/2
          ELSE
           PHI=ATAN2((J*1.-JCNTR),(I*1.-ICNTR))
             ENDIF
             IF (PHI.LT.0) PHI=PHI+2*PI
         IF (THETA.EQ.0) THETA=.00000001
         IF (PHI.EQ.0) PHI=.0000001


         CALL COMPUTEAP(R,THETA,EFLDR,EFLDT)
C             CALL CONVERTEF
(THETA,PHI,EFLDR,EFLDT,EFLDX,EFLDY,EFLDZ)
         WRITE (15,*)
     &    sqrt((CABS(EFLDR)**2+CABS(EFLDT)**2))/.002554

161      CONTINUE
162      CONTINUE
163    CONTINUE


       STOP
      END
```

COMPUTEAP code:

```
C *** FIELD AMP AND PHASE COMPUTATION SUBROUTINE ******C

      SUBROUTINE COMPUTEAP (R,THETA, EFIELDR,EFIELDT)

      INTEGER I,N,IM
      REAL R, THETA, PI,MU,EPS,FREQ, PN, OMEGA
      COMPLEX EFIELDR, EFIELDT, AN(5),KR,K, JN
      EXTERNAL JN,PN
     PARAMETER(EPSR=51,SIGMA=1.28)
```

```fortran
      PI=acos(-1.)
      FREQ=914000000
      OMEGA=2*PI*FREQ
     MU=4*PI*1E-7
      EPS=8.854e-12*(EPSR)
C       K=(0.,-1.)*OMEGA*SQRT(MU*EPS)*SQRT(.5*(SQRT(1.
C     &  +(1.28/(OMEGA*EPS))**2.)+1.))
C     WRITE(6,*) K
      K=(0.,-1.)*(SQRT((0.,1.)*OMEGA*MU*(SIGMA+(0.,1.)*
     &   OMEGA*EPS)))
C     K=IMAG(SQRT(-(OMEGA)**2.*MU*EPS+(0,1.)*OMEGA*MU*1.28))
C      WRITE(6,*) K
      KR=K*R
C     WRITE(6,*) KR
      AN(1)=(1.20600400996,.891938522519)
      AN(2)=(0,0)
      AN(3)=(-.19024554426,-.0548692344507)
      AN(4)=(0,0)
      AN(5)=(.050541055694,-.0191137469021)
      An(2)=(0,0)
      An(4)=(0,0)
      EFIELDR=0
      EFIELDT=0
      DO 500 N=1,3
       I=2*N-1
     IM=I-1
        EFIELDR=EFIELDR+AN(I)*((I*(I+1))/(KR))*
     &   JN(I,KR)*PN(I,COS(THETA))
        EFIELDT=EFIELDT+AN(I)*(JN((IM),KR)-
     &
(I/KR)*JN(I,KR))*(I/SIN(THETA))*(COS(THETA)*PN(I,COS(THETA))-
     &   PN((IM),COS(THETA)))

500   CONTINUE
      RETURN
      END
```

```
C*********************************************************C
```

CONVERTEF code:

```
C *** FIELD CONVERSION SUBROUTINE (COMPUTES FROM SPHERICAL TO
RECT) *** C

      SUBROUTINE CONVERTEF
(THETA,PHI,EFLDR,EFLDT,EFLDX,EFLDY,EFLDZ)

      COMPLEX EFLDR, EFLDT, EFLDX, EFLDY, EFLDZ
      REAL THETA,PHI


EFLDX=SIN(THETA)*COS(PHI)*EFLDR+COS(THETA)*COS(PHI)*EFLDT

EFLDY=SIN(THETA)*SIN(PHI)*EFLDR+COS(THETA)*SIN(PHI)*EFLDT
      EFLDZ=COS(THETA)*EFLDR-SIN(THETA)*EFLDT

      RETURN
      END
C
*********************************************************C
```

DIRECT.F Code

```
      PROGRAM direct

C This code is modified often to produce plots of different
areas of the exact source.

      INTEGER I,J,K,KCNTR,ICNTR,JCNTR,RADIUS
```

```
      REAL THETA,PI,R,PN,PHI,CELLSIZE,EFXR,EFYR,EFZR
      REAL EFXI,EFYI,EFZI,MAGEX,MAGEY,MAGEZ
      COMPLEX EFLDT,EFLDR,JN,EFLDX,EFLDY,EFLDZ
      EXTERNAL JN,PN

C     READ (5,*) N, z
C     WRITE(6,*) JN(N,Z)
      KCNTR=40
      JCNTR=40
      ICNTR=40
      RADIUS=30
      CELLSIZE=.0032
      R=.0945
      THETA=ACOS(-1.)/2.
      PI= ACOS(-1.)
      PHI=PI/2
      DO 100 I=0, 90
      theta=(I/90.)*pi
      IF (R.LT.0.004) R=.004
C     WRITE(6,*) R,THETA,PHI
        CALL COMPUTEAP (R,THETA,EFLDR,EFLDT)
      WRITE(6,*)
((sqrt(cabs(EFLDT)**2.+cabs(EFLDR)**2.)**2.)/2.)*1.28
C     CALL CONVERTEF(THETA,PHI,EFLDR,EFLDT,EFLDX,EFLDY,EFLDZ)
C     WRITE(6,*) R, CABS(EFLDT)
100   CONTINUE
      STOP
      END
```

IDROT.F Code

```
      program idrot
C     This program wioll rotate the ID matrix to make it
compatible
```

```
C      with the power matrix.


       REAL id1(75,75,75),id2(75,75,75),id3(75,75,75)
       INTEGER I,J,K


       OPEN(22,FILE='S6ID2.dat',STATUS='OLD')
       OPEN(23,FILE='S6ID3.dat',STATUS='UNKNOWN')
       DO 101 K=1,75
       DO 102 J=1,75
       DO 103 I=1,75
         READ(22,*) id1(I,J,K),ID2(I,J,K),id3(I,J,K)
103    CONTINUE
102    CONTINUE
101    CONTINUE

       DO 104 I=1,75
       DO 105 J=1,75
       DO 106 K=1,75

         WRITE(23,*) id1(I,J,K),id2(I,J,K),id3(I,J,K)
106    CONTINUE
105    CONTINUE
104    CONTINUE
       CLOSE(22)
       CLOSE(23)
       STOP
       END
```

JN code:

```
C****** Spherical Bessel Function Subroutine ***********C
       COMPLEX FUNCTION JN (N,Z)
```

```fortran
      INTEGER N,II
      COMPLEX Z,JJN(20),JN0

      JN0=CSIN(Z)/Z
      IF (N.EQ.0) THEN
       JN=JN0
       RETURN
      ENDIF
      JJN(1)=CSIN(Z)/Z**2.0-CCOS(Z)/Z
      IF (N.EQ.1) THEN
       JN=JJN(1)
       RETURN
      ENDIF
      JJN(2)=(3./z**3.0-1./Z)*CSIN(Z)-(3./Z**2.)*CCOS(Z)
      IF (N.EQ.2) THEN
       JN=JJN(2)
       RETURN
      ENDIF
      IF (N.GT.2) THEN
       DO 100 II=3,N
        JJN(II)=((2*(II-1)+1)/Z)*JJN(II-1)-JJN(II-2)
100    CONTINUE
       JN=JJN(N)
       RETURN
      ENDIF
      RETURN
      END
C******************************************************************C
```

MODIFYGEOM.f Code

```fortran
      PROGRAM MODIFYGEOM
```

```fortran
C THIS PROGRAM MODIFIES THE GEOMETRY FILE TO SHOW WHERE
SOURCES WERE
C SET.



      REAL R
      REAL TMP1,TMP2,TMP3,TMP4,TMP5
      INTEGER
I,J,K,IDONE(92,92,95),IDTWO(92,92,95),IDTHRE(92,92,95)
      INTEGER NX,NY,NZ,ITMP1,ITMP2
      PARAMETER(ICNTR=48,JCNTR=48,KCNTR=4)
      PARAMETER(RADIUS=37)



      OPEN (22,FILE='SPHERE3.id',STATUS='OLD')
      OPEN (23,FILE='SPHERE3.m.id',STATUS='UNKNOWN')
      REWIND(23)
      READ (22,*) NX,NY,NZ
      WRITE(23,*) NX,NY,NZ
      READ(22,*) TMP1,TMP2,TMP3
      WRITE(23,*) TMP1,TMP2,TMP3
      CELLSIZE=TMP1
      READ(22,*) ITMP1
      WRITE(23,*) ITMP1
      DO 100 I=1, 14
       READ(22,*) TMP1, TMP2, TMP3, TMP4, TMP5
       WRITE(23,*) TMP1, TMP2, TMP3, TMP4, TMP5
100   CONTINUE
      READ(22,*) ITMP1,ITMP2
      WRITE(23,*) ITMP1,ITMP2

      WRITE(6,*) ICNTR,KCNTR,JCNTR
       DO 101 K=1, NZ
      WRITE(6,*) K
        DO 102 J=1, NY
      DO 103 I=1, NX
```

```
      READ(22,*) IDONE(I,J,K),IDTWO(I,J,K),IDTHRE(I,J,K)


C  FIRST CHECK THE RADIUS AT THE CENTER OF THE CUBE OF
INTEREST
          R=SQRT(((I*1.+.5)-ICNTR*1.)**2.+((J*1.+.5)-
JCNTR*1.)**2.+
     &            ((K*1.+.5)-KCNTR*1.)**2.)
C  IF IT IS WITHIN 1/2 CELL OF TEH RADIUS THEN SET THE 12 E
COMPONENTS
          IF((R.GT.RADIUS-.5).AND.(R.LE.RADIUS+.5)) THEN
C START BY SETTING THE EX(I,J,K) COMPONENT
        IDONE(I,J,K)=10
C NOW SET THE EX(I,J,K+1) COMPONENT
        IDONE(I,J,K+1)=10
C NOW SET THE EX(I,J+1,K+1) COMPONENT
        IDONE(I,J+1,K+1)=0
C NOW SET THE EX(I,J+1,K) COMPONENT
        IDONE(I,J+1,K)=10
C NOW SET THE EY(I,J,K) COMPONENT
        IDTWO(I,J,K)=10
C NOW SET THE EY(I+1,J,K) COMPONENT
        IDTWO(I+1,J,K)=10
C NOW SET THE EY(I+1,J,K+1) COMPONENT
        IDTWO(I+1,J,K+1)=0
C NOW SET THE EY(I,J,K+1)
        IDTWO(I,J,K+1)=10
C NOW SET THE EZ(I,J,K) COMPONENT
        IDTHRE(I,J,K)=10
C NOW SET THE EZ(I+1,J,K) COMPONENT
        IDTHRE(I+1,J,K)=10
C NOW SET THE EZ(I+1,J+1,K) COMPONENT
        IDTHRE(I+1,J+1,K)=10
C NOW SET THE EZ(I,J+1,K) COMPONENT
        IDTHRE(I,J+1,K)=10
```

```
      ENDIF

      WRITE(23,*) IDONE(I,J,K),IDTWO(I,J,K),IDTHRE(I,J,K)
103   CONTINUE
102     CONTINUE
101   CONTINUE


      CLOSE(22)
      CLOSE(23)
      STOP
      END
```

NECKEXTEND.F Code

```
      PROGRAM NECKEXTEND

C     THIS PROGRAM EXTENDS THE NECK DOWN TO THE EDGE OF FDTD
SPACE

      REAL TMP1,TMP2,TMP3,TMP4,TMP5
      INTEGER
I,J,K,IDONE(92,92,95),IDTWO(92,92,95),IDTHRE(92,92,95)
      INTEGER NX,NY,NZ,ITMP1,ITMP2,Z


      OPEN (22,FILE='head5.id',STATUS='OLD')
      OPEN (23,FILE='head6.id',STATUS='UNKNOWN')
      REWIND(23)
      READ (22,*) NX,NY,NZ
      WRITE(23,*) NX,NY,NZ
      READ(22,*) TMP1,TMP2,TMP3
      WRITE(23,*) TMP1,TMP2,TMP3
      CELLSIZE=TMP1
      READ(22,*) ITMP1
```

```
      WRITE(23,*) ITMP1
      DO 100 I=1, 14
       READ(22,*) TMP1, TMP2, TMP3, TMP4, TMP5
       WRITE(23,*) TMP1, TMP2, TMP3, TMP4, TMP5
100   CONTINUE
      READ(22,*) ITMP1,ITMP2
      WRITE(23,*) ITMP1,ITMP2

       DO 101 K=1, NZ
        DO 102 J=1, NY
      DO 103 I=1, NX

      READ(22,*) IDONE(I,J,K),IDTWO(I,J,K),IDTHRE(I,J,K)

103      CONTINUE
102      CONTINUE
101    CONTINUE

       DO 104 K=1, 17
      WRITE(6,*) K
        DO 105 J=1, NY
      DO 106 I=1, NX

      Z=18-K
      IF (IDONE(I,J,Z+1).NE.0.AND.IDONE(I,J,Z+1).NE.2)
     &    IDONE(I,J,Z)=IDONE(I,J,Z+1)
      IF (IDTWO(I,J,Z+1).NE.0.AND.IDTWO(I,J,Z+1).NE.2)
     &    IDTWO(I,J,Z)=IDTWO(I,J,Z+1)
      IF (IDTHRE(I,J,Z+1).NE.0.AND.IDTHRE(I,J,Z+1).NE.2)
     &    IDTHRE(I,J,Z)=IDTHRE(I,J,Z+1)

106      CONTINUE
105    CONTINUE
104    CONTINUE
```

104

```
      DO 107 K=1, NZ
       DO 108 J=1, NY
      DO 109 I=1, NX

      WRITE(23,*) IDONE(I,J,K),IDTWO(I,J,K),IDTHRE(I,J,K)


109      CONTINUE
108      CONTINUE
107      CONTINUE


      STOP
      END
```

OPTIMIZE.F Code

```
      PROGRAM Optimize
C      This program computes the An coefficients for a given
C      eps and sigma at 915 MHZ for a sphere of radius 9.45
cm

      INTEGER I,N
      COMPLEX KR,JN,K,AN(5)
      REAL PI,FREQ,EPS,EPSR,SIGMA,RADIUS,OMEGA,MU,JNP(5)
      EXTERNAL JN, PN


C *** INITIALIZE *** C
      PI=ACOS(-1.)
      RADIUS=.0945
      WRITE(6,*) 'EPSR=?'
      READ(5,*) EPSR
```

```fortran
      WRITE(6,*) 'Sigma=?'
      READ(5,*) sigma
      JNP(1)=.9509
      JNP(3)=.1148
      JNP(5)=.0260
      FREQ=914000000
      OMEGA=2*PI*FREQ
      MU=4*PI*1E-7
      EPS=8.854e-12*(EPSR)
      K=(0.,-1.)*(SQRT((0.,1.)*OMEGA*MU*(sigma+(0.,1.)*
     &   OMEGA*EPS)))
      KR=K*RADIUS
      WRITE(6,*)K,KR
      DO 100 I=1,3
      WRITE(6,*) 'I=',I
      N=(I*2)-1
      An(N)=JNP(N)/(JN(N-1,KR)-(N/KR)*JN(N,KR))
      WRITE(6,*) 'An(',N,')= ',An(N)
100   CONTINUE
      STOP
      END
```

PN code:

```fortran
C *** LEGENDRE POLYNOMIAL FUNCTION, CALCULATES LEGENDRE
C *** POLYNOMIALS OF ORDER n (n=0-5)

      REAL FUNCTION PN (N,X)

      INTEGER N
      REAL X
```

```
      IF (N.EQ.0) PN=1
      IF (N.EQ.1) PN=X
      IF (N.EQ.2) PN=.5*(3.*X**2.-1.)
      IF (N.EQ.3) PN=0.5*(5.*X**3.-3.*X)
      IF (N.EQ.4) PN=(1./8.)*(35.*X**4.-30.*X**2.+3.)
      IF (N.EQ.5) PN=(1./8.)*(63.*X**5.-70.*X**3.+15.*X)


      RETURN
      END
C  ****************************************************
```

SOURCE.FOR code for the approximate source distribution

```
C  FIRST CHECK THE RADIUS AT THE CENTER OF THE CUBE OF
INTEREST
          R=SQRT((I*1.+.5-ICNTR)**2.+(J*1.+.5-JCNTR)**2.+
     &          (K*1.+.5-KCNTR)**2.)
C  IF IT IS WITHIN 1/2 CELL OF TEH RADIUS THEN SET THE 12 E
COMPONENTS
      -   IF((R.GT.RADIUS-.5).AND.(R.LE.RADIUS+.5)) THEN
C START BY SETTING THE EX(I,J,K) COMPONENT
            R=R*CELLSIZE
        IF (K.EQ.KCNTR) THEN
          THETA=ACOS(-1.)/2.
           ELSE
          THETA=ATAN2((SQRT((I*1.+.5-ICNTR)**2.
     &          +(J*1.-JCNTR)**2.)),(K*1.-KCNTR))
           ENDIF
        PHI=ATAN2((J*1.-JCNTR),(I*1.+.5-ICNTR))
        IF (THETA.EQ.0) THETA=.00000001
        IF (PHI.EQ.0) PHI=.0000001
        CALL COMPUTEAP (R,THETA,EFLDR,EFLDT)
```

107

```
                CALL CONVERTEF
(THETA,PHI,EFLDR,EFLDT,EFLDX,EFLDY,EFLDZ)
                EFXR=REAL(EFLDX)
                EFXI=IMAG(EFLDX)
                MAGEX=CABS(EFLDX)
                IF (MAGEX.GT.LIMIT) THEN
                  IF (EFXR.NE.0.) THEN
                    PHASEX=ATAN2(EFXI,EFXR)
                  ELSE
                PHASEX=ACOS(-1.)/2.
                  ENDIF
                NTAU=NINT(T/DT)
                EXS(I,J,K)=MAGEX/DELX
     &            *FLOAT(MIN(NTAU,NRISE))/NRISE*COS(W1*T+PHASEX).
                EXS(I,J,K+1)=MAGEX/DELX
     &            *FLOAT(MIN(NTAU,NRISE))/NRISE*COS(W1*T+PHASEX)
                EXS(I,J+1,K+1)=MAGEX/DELX
     &            *FLOAT(MIN(NTAU,NRISE))/NRISE*COS(W1*T+PHASEX)
                EXS(I,J+1,K)=MAGEX/DELX
     &            *FLOAT(MIN(NTAU,NRISE))/NRISE*COS(W1*T+PHASEX)
                ENDIF
                EFYR=REAL(EFLDY)
                EFYI=IMAG(EFLDY)
                MAGEY=CABS(EFLDY)
                IF (MAGEY.GT.LIMIT) THEN
                  IF (EFYR.NE.0.) THEN
                    PHASEY=ATAN2(EFYI,EFYR)
                  ELSE
                PHASEY=ACOS(-1.)/2.
                  ENDIF
                EYS(I,J,K)=MAGEY/DELY
     &            *FLOAT(MIN(NTAU,NRISE))/NRISE*COS(W1*T+PHASEY)
                 EYS(I+1,J,K)=MAGEY/DELY
     &            *FLOAT(MIN(NTAU,NRISE))/NRISE*COS(W1*T+PHASEY)
                EYS(I+1,J,K+1)=MAGEY/DELY
     &            *FLOAT(MIN(NTAU,NRISE))/NRISE*COS(W1*T+PHASEY)
```

```fortran
            PHASEY=ACOS(-1.)/2.
              EYS(I,J,K+1)=MAGEY/DELY
     &          *FLOAT(MIN(NTAU,NRISE))/NRISE*COS(W1*T+PHASEY)
            ENDIF
            EFZR=REAL(EFLDZ)
            EFZI=IMAG(EFLDZ)
            MAGEZ=CABS(EFLDZ)
            IF (MAGEZ.GT.LIMIT) THEN
              IF (EFZR.NE.0.) THEN
                PHASEZ=ATAN2(EFZI,EFZR)
               ELSE
            PHASEZ=ACOS(-1.)/2.
              ENDIF
              EZS(I,J,K)=MAGEZ/DELZ
     &          *FLOAT(MIN(NTAU,NRISE))/NRISE*COS(W1*T+PHASEZ)
              EZS(I+1,J,K)=MAGEZ/DELZ
     &          *FLOAT(MIN(NTAU,NRISE))/NRISE*COS(W1*T+PHASEZ)
              EZS(I+1,J+1,K)=MAGEZ/DELZ
     &          *FLOAT(MIN(NTAU,NRISE))/NRISE*COS(W1*T+PHASEZ)
              EZS(I,J+1,K)=MAGEZ/DELZ
     &          *FLOAT(MIN(NTAU,NRISE))/NRISE*COS(W1*T+PHASEZ)
            ENDIF
          ENDIF
```

SOURCE.FOR Code for an exact field distribution:

```fortran
C   FIRST CHECK THE RADIUS AT THE CENTER OF THE CUBE OF
C   INTEREST
          R=SQRT((I*1.+.5-ICNTR)**2.+(J*1.+.5-JCNTR)**2.+
     &          (K*1.+.5-KCNTR)**2.)
C   IF IT IS WITHIN 1/2 CELL OF TEH RADIUS THEN SET THE 12 E
C   COMPONENTS
          IF((R.GT.RADIUS-.5).AND.(R.LE.RADIUS+.5)) THEN
```

```fortran
C START BY SETTING THE EX(I,J,K) COMPONENT
            R=SQRT((I*1.+.5-ICNTR)**2.+(J*1.-JCNTR)**2.+
     &          (K*1.-KCNTR)**2.)*CELLSIZE
          IF (K.EQ.KCNTR) THEN
            THETA=ACOS(-1.)/2.
             ELSE
            THETA=ATAN2((SQRT((I*1.+.5-ICNTR)**2.
     &          +(J*1.-JCNTR)**2.)),(K*1.-KCNTR))
            ENDIF
          PHI=ATAN2((J*1.-JCNTR),(I*1.+.5-ICNTR))
          IF (THETA.EQ.0) THETA=.00000001
          IF (PHI.EQ.0) PHI=.0000001
           CALL COMPUTEAP (R,THETA,EFLDR,EFLDT)
           CALL CONVERTEF
              (THETA,PHI,EFLDR,EFLDT,EFLDX,EFLDY,EFLDZ)
            EFXR=REAL(EFLDX)
            EFXI=IMAG(EFLDX)
            MAGEX=CABS(EFLDX)
            IF (MAGEX.GT.LIMIT) THEN
             IF (EFXR.NE.0.) THEN
                PHASEX=ATAN2(EFXI,EFXR)
               ELSE
            PHASEX=ACOS(-1.)/2.
              ENDIF
              NTAU=NINT(T/DT)
              EXS(I,J,K)=MAGEX/DELX
     &          *FLOAT(MIN(NTAU,NRISE))/NRISE*COS(W1*T+PHASEX)
            ENDIF
C NOW SET THE EX(I,J,K+1) COMPONENT
            R=SQRT((I*1.+.5-ICNTR)**2.+(J*1.-JCNTR)**2.+
     &          (K*1.+1-KCNTR)**2.)*CELLSIZE
          IF ((K+1).EQ.KCNTR) THEN
            THETA=ACOS(-1.)/2.
             ELSE
            THETA=ATAN2((SQRT((I*1.+.5-ICNTR)**2.
     &          +(J*1.-JCNTR)**2.)),(K*1.+1-KCNTR))
```

```fortran
              ENDIF
         PHI=ATAN2((J*1.-JCNTR),(I*1.+.5-ICNTR))
         IF (THETA.EQ.0) THETA=.00000001
         IF (PHI.EQ.0) PHI=.0000001
         CALL COMPUTEAP (R,THETA,EFLDR,EFLDT)
            CALL CONVERTEF
(THETA,PHI,EFLDR,EFLDT,EFLDX,EFLDY,EFLDZ)
            EFXR=REAL(EFLDX)
            EFXI=IMAG(EFLDX)
            MAGEX=CABS(EFLDX)
            IF (MAGEX.GT.LIMIT) THEN
             IF (EFXR.NE.0.) THEN
                PHASEX=ATAN2(EFXI,EFXR)
               ELSE
           PHASEX=ACOS(-1.)/2.
             ENDIF
             NTAU=NINT(T/DT)
             EXS(I,J,K+1)=MAGEX/DELX
     &          *FLOAT(MIN(NTAU,NRISE))/NRISE*COS(W1*T+PHASEX)
            ENDIF
C NOW SET THE EX(I,J+1,K+1) COMPONENT
            R=SQRT((I*1.+.5-ICNTR)**2.+(J*1.+1-JCNTR)**2.+
     &          (K*1.+1-KCNTR)**2.)*CELLSIZE
         IF ((K+1).EQ.KCNTR) THEN
           THETA=ACOS(-1.)/2.
             ELSE
           THETA=ATAN2((SQRT((I*1.+.5-ICNTR)**2.
     &          +(J*1.+1-JCNTR)**2.)),(K*1.+1-KCNTR))
             ENDIF
         PHI=ATAN2((J*1.+1-JCNTR),(I*1.+.5-ICNTR))
         IF (THETA.EQ.0) THETA=.00000001
         IF (PHI.EQ.0) PHI=.0000001
         CALL COMPUTEAP (R,THETA,EFLDR,EFLDT)
            CALL CONVERTEF
(THETA,PHI,EFLDR,EFLDT,EFLDX,EFLDY,EFLDZ)
            EFXR=REAL(EFLDX)
```

111

```fortran
            EFXI=IMAG(EFLDX)
            MAGEX=CABS(EFLDX)
            IF (MAGEX.GT.LIMIT) THEN
             IF (EFXR.NE.0.) THEN
               PHASEX=ATAN2(EFXI,EFXR)
              ELSE
           PHASEX=ACOS(-1.)/2.
             ENDIF
             NTAU=NINT(T/DT)
             EXS(I,J+1,K+1)=MAGEX/DELX
     &         *FLOAT(MIN(NTAU,NRISE))/NRISE*COS(W1*T+PHASEX)
            ENDIF
C NOW SET THE EX(I,J+1,K) COMPONENT
            R=SQRT((I*1.+.5-ICNTR)**2.+(J*1.+1-JCNTR)**2.+
     &         (K*1.-KCNTR)**2.)*CELLSIZE
           IF (K.EQ.KCNTR) THEN
            THETA=ACOS(-1.)/2.
             ELSE
            THETA=ATAN2((SQRT((I*1.+.5-ICNTR)**2.
     &          +(J*1.+1-JCNTR)**2.)),(K*1.-KCNTR))
             ENDIF
           PHI=ATAN2((J*1.+1-JCNTR),(I*1.+.5-ICNTR))
           IF (THETA.EQ.0) THETA=.00000001
           IF (PHI.EQ.0) PHI=.0000001
           CALL COMPUTEAP (R,THETA,EFLDR,EFLDT)
            CALL CONVERTEF
   (THETA,PHI,EFLDR,EFLDT,EFLDX,EFLDY,EFLDZ)
            EFXR=REAL(EFLDX)
            EFXI=IMAG(EFLDX)
            MAGEX=CABS(EFLDX)
           IF (MAGEX.GT.LIMIT) THEN
            IF (EFXR.NE.0.) THEN
               PHASEX=ATAN2(EFXI,EFXR)
              ELSE
           PHASEX=ACOS(-1.)/2.
             ENDIF
```

```fortran
                 NTAU=NINT(T/DT)
                 EXS(I,J+1,K)=MAGEX/DELX
     &           *FLOAT(MIN(NTAU,NRISE))/NRISE*COS(W1*T+PHASEX)
                 ENDIF
C NOW SET THE EY(I,J,K) COMPONENT
                 R=SQRT((I*1.-ICNTR)**2.+(J*1.+.5-JCNTR)**2.+
     &           (K*1.-KCNTR)**2.)*CELLSIZE
             IF (K.EQ.KCNTR) THEN
               THETA=ACOS(-1.)/2.
               ELSE
               THETA=ATAN2((SQRT((I*1.-ICNTR)**2.
     &             +(J*1.+.5-JCNTR)**2.)),(K*1.-KCNTR))
               ENDIF
             PHI=ATAN2((J*1.+.5-JCNTR),(I*1.-ICNTR))
             IF (THETA.EQ.0) THETA=.00000001
             IF (PHI.EQ.0) PHI=.0000001
             CALL COMPUTEAP (R,THETA,EFLDR,EFLDT)
                 CALL CONVERTEF
 (THETA,PHI,EFLDR,EFLDT,EFLDX,EFLDY,EFLDZ)
                 EFYR=REAL(EFLDY)
                 EFYI=IMAG(EFLDY)
                 MAGEY=CABS(EFLDY)
               IF (MAGEY.GT.LIMIT) THEN
                 IF (EFYR.NE.0.) THEN
                   PHASEY=ATAN2(EFYI,EFYR)
                 ELSE
               PHASEY=ACOS(-1.)/2.
                 ENDIF
                 NTAU=NINT(T/DT)
                 EYS(I,J,K)=MAGEY/DELY
     &           *FLOAT(MIN(NTAU,NRISE))/NRISE*COS(W1*T+PHASEY)
                 ENDIF
C NOW SET THE EY(I+1,J,K) COMPONENT
                 R=SQRT((I*1.+1-ICNTR)**2.+(J*1.+.5-JCNTR)**2.+
     &           (K*1.-KCNTR)**2.)*CELLSIZE
             IF (K.EQ.KCNTR) THEN
```

113

```
            THETA=ACOS(-1.)/2.
              ELSE
            THETA=ATAN2((SQRT((I*1.+1-ICNTR)**2.
     &            +(J*1.+.5-JCNTR)**2.)),(K*1.-KCNTR))
              ENDIF
          PHI=ATAN2((J*1.+.5-JCNTR),(I*1.+1-ICNTR))
          IF (THETA.EQ.0) THETA=.00000001
          IF (PHI.EQ.0) PHI=.0000001
          CALL COMPUTEAP (R,THETA,EFLDR,EFLDT)
            CALL CONVERTEF
  (THETA,PHI,EFLDR,EFLDT,EFLDX,EFLDY,EFLDZ)
            EFYR=REAL(EFLDY)
            EFYI=IMAG(EFLDY)
            MAGEY=CABS(EFLDY)
            IF (MAGEY.GT.LIMIT) THEN
              IF (EFYR.NE.0.) THEN
                PHASEY=ATAN2(EFYI,EFYR)
               ELSE
           PHASEY=ACOS(-1.)/2.
              ENDIF
              NTAU=NINT(T/DT)
              EYS(I+1,J,K)=MAGEY/DELY
     &          *FLOAT(MIN(NTAU,NRISE))/NRISE*COS(W1*T+PHASEY)
            ENDIF
C NOW SET THE EY(I+1,J,K+1) COMPONENT
            R=SQRT((I*1.+1-ICNTR)**2.+(J*1.+.5-JCNTR)**2.+
     &          (K*1.+1-KCNTR)**2.)*CELLSIZE
          IF ((K+1).EQ.KCNTR) THEN
            THETA=ACOS(-1.)/2.
              ELSE
            THETA=ATAN2((SQRT((I*1.+1-ICNTR)**2.
     &            +(J*1.+.5-JCNTR)**2.)),(K*1.+1-KCNTR))
              ENDIF
          PHI=ATAN2((J*1.+.5-JCNTR),(I*1.+1-ICNTR))
          IF (THETA.EQ.0) THETA=.00000001
          IF (PHI.EQ.0) PHI=.0000001
```

114

```fortran
          CALL COMPUTEAP (R,THETA,EFLDR,EFLDT)
            CALL CONVERTEF
(THETA,PHI,EFLDR,EFLDT,EFLDX,EFLDY,EFLDZ)
            EFYR=REAL(EFLDY)
            EFYI=IMAG(EFLDY)
            MAGEY=CABS(EFLDY)
            IF (MAGEY.GT.LIMIT) THEN
             IF (EFYR.NE.0.) THEN
               PHASEY=ATAN2(EFYI,EFYR)
              ELSE
          PHASEY=ACOS(-1.)/2.
             ENDIF
             NTAU=NINT(T/DT)
             EYS(I+1,J,K+1)=MAGEY/DELY
     &       *FLOAT(MIN(NTAU,NRISE))/NRISE*COS(W1*T+PHASEY)
            ENDIF
C NOW SET THE EY(I,J,K+1)
            R=SQRT((I*1.-ICNTR)**2.+(J*1.+.5-JCNTR)**2.+
     &         (K*1.+1-KCNTR)**2.)*CELLSIZE
          IF ((K+1).EQ.KCNTR) THEN
            THETA=ACOS(-1.)/2.
             ELSE
            THETA=ATAN2((SQRT((I*1.-ICNTR)**2.
     &          +(J*1.+.5-JCNTR)**2.)),(K*1.+1-KCNTR))
            ENDIF
          PHI=ATAN2((J*1.+.5-JCNTR),(I*1.-ICNTR))
          IF (THETA.EQ.0) THETA=.00000001
          IF (PHI.EQ.0) PHI=.0000001
          CALL COMPUTEAP (R,THETA,EFLDR,EFLDT)
            CALL CONVERTEF
(THETA,PHI,EFLDR,EFLDT,EFLDX,EFLDY,EFLDZ)
            EFYR=REAL(EFLDY)
            EFYI=IMAG(EFLDY)
            MAGEY=CABS(EFLDY)
            IF (MAGEY.GT.LIMIT) THEN
             IF (EFYR.NE.0.) THEN
```

```fortran
            PHASEY=ATAN2(EFYI,EFYR)
          ELSE
      PHASEY=ACOS(-1.)/2.
          ENDIF
          NTAU=NINT(T/DT)
          EYS(I,J,K+1)=MAGEY/DELY
     &      *FLOAT(MIN(NTAU,NRISE))/NRISE*COS(W1*T+PHASEY)
          ENDIF
C NOW SET THE EZ(I,J,K) COMPONENT
          R=SQRT(((I*1.-ICNTR)**2.+(J*1.-JCNTR)**2.+
     &       (K*1.+.5-KCNTR)**2.)*CELLSIZE
       THETA=ATAN2((SQRT((I*1.-ICNTR)**2.
     &         +(J*1.-JCNTR)**2.)),(K*1.+.5-KCNTR))
          IF (I.EQ.ICNTR.AND.J.EQ.JCNTR) THEN
        PHI=-ACOS(-1.)/2.
       ELSE
        PHI=ATAN2((J*1.-JCNTR),(I*1.-ICNTR))
          ENDIF
       IF (THETA.EQ.0) THETA=.00000001
       IF (PHI.EQ.0) PHI=.0000001
       CALL COMPUTEAP (R,THETA,EFLDR,EFLDT)
          CALL CONVERTEF
(THETA,PHI,EFLDR,EFLDT,EFLDX,EFLDY,EFLDZ)
          EFZR=REAL(EFLDZ)
          EFZI=IMAG(EFLDZ)
          MAGEZ=CABS(EFLDZ)
          IF (MAGEZ.GT.LIMIT) THEN
           IF (EFZR.NE.0.) THEN
            PHASEZ=ATAN2(EFZI,EFZR)
           ELSE
        PHASEZ=ACOS(-1.)/2.
          ENDIF
          NTAU=NINT(T/DT)
          EZS(I,J,K)=MAGEZ/DELZ
     &      *FLOAT(MIN(NTAU,NRISE))/NRISE*COS(W1*T+PHASEZ)
          ENDIF
```

```
C NOW SET THE EZ(I+1,J,K) COMPONENT
              R=SQRT((I*1.+1-ICNTR)**2.+(J*1.-JCNTR)**2.+
     &           (K*1.+.5-KCNTR)**2.)*CELLSIZE
              THETA=ATAN2((SQRT((I*1.+1-ICNTR)**2.
     &            +(J*1.-JCNTR)**2.)),(K*1.+.5-KCNTR))
              IF ((I+1).EQ.ICNTR.AND.J.EQ.JCNTR) THEN
               PHI=-ACOS(-1.)/2.
              ELSE
                PHI=ATAN2((J*1.-JCNTR),(I*1.+1.-ICNTR))
               ENDIF
              IF (THETA.EQ.0) THETA=.00000001
              IF (PHI.EQ.0) PHI=.0000001
              CALL COMPUTEAP (R,THETA,EFLDR,EFLDT)
              CALL CONVERTEF
     (THETA,PHI,EFLDR,EFLDT,EFLDX,EFLDY,EFLDZ)
              EFZR=REAL(EFLDZ)
              EFZI=IMAG(EFLDZ)
              MAGEZ=CABS(EFLDZ)
              IF (MAGEZ.GT.LIMIT) THEN
                IF (EFZR.NE.0.) THEN
                   PHASEZ=ATAN2(EFZI,EFZR)
                 ELSE
                PHASEZ=ACOS(-1.)/2.
                 ENDIF
                 NTAU=NINT(T/DT)
                 EZS(I+1,J,K)=MAGEZ/DELZ
     &             *FLOAT(MIN(NTAU,NRISE))/NRISE*COS(W1*T+PHASEZ)
                 ENDIF
C NOW SET THE EZ(I+1,J+1,K) COMPONENT
              R=SQRT((I*1.+1-ICNTR)**2.+(J*1.+1.-JCNTR)**2.+
     &           (K*1.+.5-KCNTR)**2.)*CELLSIZE
              THETA=ATAN2((SQRT((I*1.+1.-ICNTR)**2.
     &            +(J*1.+1.-JCNTR)**2.)),(K*1.+.5-KCNTR))
              IF ((I+1).EQ.ICNTR.AND.(J+1).EQ.JCNTR) THEN
               PHI=-ACOS(-1.)/2.
               ELSE
```

117

```fortran
            PHI=ATAN2((J*1.+1-JCNTR),(I*1.+1.-ICNTR))
          ENDIF
      IF (THETA.EQ.0) THETA=.00000001
      IF (PHI.EQ.0) PHI=.0000001
      CALL COMPUTEAP (R,THETA,EFLDR,EFLDT)
          CALL CONVERTEF
(THETA,PHI,EFLDR,EFLDT,EFLDX,EFLDY,EFLDZ)
          EFZR=REAL(EFLDZ)
          EFZI=IMAG(EFLDZ)
          MAGEZ=CABS(EFLDZ)
          IF (MAGEZ.GT.LIMIT) THEN
           IF (EFZR.NE.0.) THEN
             PHASEZ=ATAN2(EFZI,EFZR)
            ELSE
          PHASEZ=ACOS(-1.)/2.
            ENDIF
            NTAU=NINT(T/DT)
            EZS(I+1,J+1,K)=MAGEZ/DELZ
     &           *FLOAT(MIN(NTAU,NRISE))/NRISE*COS(W1*T+PHASEZ)
          ENDIF
C NOW SET THE EZ(I,J+1,K) COMPONENT
            R=SQRT((I*1.-ICNTR)**2.+(J*1.+1.-JCNTR)**2.+
     &           (K*1.+.5-KCNTR)**2.)*CELLSIZE
          THETA=ATAN2((SQRT((I*1.-ICNTR)**2.
     &           +(J*1.+1.-JCNTR)**2.)),(K*1.+.5-KCNTR))
          IF (I.EQ.ICNTR.AND.(J+1).EQ.JCNTR) THEN
           PHI=-ACOS(-1.)/2.
          ELSE
           PHI=ATAN2((J*1.+1-JCNTR),(I*1.-ICNTR))
           ENDIF
      IF (THETA.EQ.0) THETA=.00000001
      IF (PHI.EQ.0) PHI=.0000001
      CALL COMPUTEAP (R,THETA,EFLDR,EFLDT)
          CALL CONVERTEF
(THETA,PHI,EFLDR,EFLDT,EFLDX,EFLDY,EFLDZ)
          EFZR=REAL(EFLDZ)
```

118

```
               EFZI=IMAG(EFLDZ)
               MAGEZ=CABS(EFLDZ)
               IF (MAGEZ.GT.LIMIT) THEN
                 IF (EFZR.NE.0.) THEN
                    PHASEZ=ATAN2(EFZI,EFZR)
                  ELSE
              PHASEZ=ACOS(-1.)/2.
                 ENDIF
                 NTAU=NINT(T/DT)
                 EZS(I,J+1,K)=MAGEZ/DELZ
     &              *FLOAT(MIN(NTAU,NRISE))/NRISE*COS(W1*T+PHASEZ)
               ENDIF



           ENDIF
```

WRITEEF code:

```
C *** SUBROUTINE TO WRITE OUT FIELDS TO A FILE ********C

      SUBROUTINE WRITEEF (EFLDX,EFLDY,EFLDZ,I,J,K,COUNT)

      COMPLEX EFLDX,EFLDY,EFLDZ
      REAL
EFXR,EFXI,EFYR,EFYI,EFZR,EFZI,TESTX,TESTY,TESTZ,LIMIT
      REAL PHASEX,PHASEY,PHASEZ
      INTEGER I,J,K,COUNT

      LIMIT=.01

OPEN(UNIT=25,FILE="SPHERESOURCE.DAT",STATUS="OLD",ACCESS='APP
END')
      EFXR=REAL(EFLDX)
```

```
EFYR=REAL(EFLDY)

EFZR=REAL(EFLDZ)

EFXI=IMAG(EFLDX)

EFYI=IMAG(EFLDY)

EFZI=IMAG(EFLDZ)


TESTX=CABS(EFLDX)*1000

TESTY=CABS(EFLDY)*1000

TESTZ=CABS(EFLDZ)*1000

IF (TESTX.GT.LIMIT) THEN

COUNT=COUNT+1

IF (EFXR.NE.0) THEN

    PHASEX=ATAN2(EFXI,EFXR)

ELSE

     PHASEX=(ACOS(-1.)/2)

ENDIF

     WRITE(25,80) I,J,K,0,TESTX,PHASEX

ENDIF

IF (TESTY.GT.LIMIT) THEN

COUNT=COUNT+1

   IF (EFYR.NE.0) THEN

PHASEY=ATAN2(EFYI,EFYR)

ELSE

     PHASEY=ACOS(-1.)/2

ENDIF

WRITE(25,80) I,J,K,1,TESTY,PHASEY

ENDIF

IF (TESTZ.GT.LIMIT) THEN

COUNT=COUNT+1

   IF (EFZR.NE.0) THEN

PHASEZ=ATAN2(EFZI,EFZR)

ELSE

     PHASEZ=ACOS(-1.)/2

ENDIF

WRITE(25,80) I,J,K,2,TESTZ,PHASEZ

ENDIF
```

```
80      FORMAT(I3,I3,I3,I2,E14.6,E14.6)
        CLOSE(25)

        RETURN
        END
C  *********************************************************C
```

Appendix D: Matlab Programs

AVG.M Code

```
function y=avg(file,file2)

% This function computes the average material characteritics
% throughout the head/bolus structure.  File is the ID file.
% File2 is a file containing the electrical characteristics
% of each material.

% Initialize
top=size(file)
count(1)=0;
count(2)=0;
count(3)=0;
y(1,1)=0;
y(1,2)=0;
y(1,3)=0;
y(2,1)=0;
y(2,2)=0;
y(2,3)=0;

% Run through the locations and the x,y and z components
% keeping a running tally of permitivity and permeability.
for i=1:top(1,1)
 for j=1:top(1,2)

% If the location isn't free space (Is part of the head/bolus
% structure).
  if file(i,j)>1,
   y(1,j)=y(1,j)+file2(file(i,j)-1,1);
   y(2,j)=y(2,j)+file2(file(i,j)-1,2);
   count(j)=count(j)+1;
  end
```

```
  end
 end


% Compute the average across all three components
 y(1,4)=(y(1,1)+y(1,2)+y(1,3))/(count(1)+count(2)+count(3));
 y(2,4)=(y(2,1)+y(2,2)+y(2,3))/(count(1)+count(2)+count(3));


% Compute the x,y, and z averages
 for j=1:top(1,2)
 y(1,j)=y(1,j)/count(j);
 y(2,j)=y(2,j)/count(j);
 end
```

AXY.M Code

```
 function y=axy(file,idfile,level,stat)
% this function will analyze an xy level of an output file
% First plot the ids for the level.  file is the power file,
% ID file is a file of the id's, level is the level to be
% analyzed, stat is a string file that describes the files
% (for display)
 idpxy(idfile,level,stat);

%now plot the power picture
 pwrpxy(file,level,stat);

% Now plot the normalized power.
 meshxyn(file,level,[-60 45],stat);
```

AYZ.M Code

```
 function y=ayz(file,idfile,level,stat)
% this function will analyze an yz level of an output file
% First plot the ids for the level.  file is the power file,
% ID file is a file of the id's, level is the level to be
% analyzed, stat is a string file that describes the files
% (for display)
 idpyz(idfile,level,stat);

%now plot the power picture
 pwrpyz(file,level,stat);

% Now plot the normalized power.
 meshyzn(file,level,[-60 45],stat);
```

CLEARSOURCE.M Code

```
 function y=clearsource(meshfile,x)
% This function clears everything from the source out for a
% particular cut of the sphere.  meshfile is a file of a
% single layer of the power file.  X is the level of the
% layer.
 y=file;

 for i=1:75
  for j=1:75

% Compute the radius at the point
   r=sqrt((i-37.5)^2+(j-37.5)^2+(x-37.5)^2);

% if the point is outside th esource, replace it with an NaN
   if r>36.5000001,
```

```
  y(i,j)=NaN;
 end
end
end
```

DIFF.M Code

```
function y=DIFF(file,level,type)

% this function computes the id changes across two level
% changes.  file is th eidfile of interes, level is the level
% of interes, and type is a string to describe the scenario
% (for display).  Insert (:,1,2 or 3) after the TEST* files
% to plot the cahnges of only the x,y or z componenets.

TEST1=meshxy(file,level-1);
TEST2=meshxy(file,level);
TEST3=meshxy(file,level+1);

figure
pcolor(TEST1-TEST2)
colormap(gray)
colorbar
ylabel('Y Value')
xlabel('X Value')
title(['Changes in ',type,' From Z=',num2str(level-1),' to
       Z=',num2str(level),'.'])

figure
pcolor(TEST3-TEST1)
colormap(gray)
colorbar
ylabel('Y Value')
xlabel('X Value')
```

```
title(['Changes in ',type,' From Z=',num2str(level+1),' to
        Z=',num2str(level),'.'])
```

ERRYZ Code:

```
function y=erryz(file1,file2,level)

% This function computes the error along one YZ slice of two
% files.  File1 is the "correct" fiel and file2 is the file
%which is being compared.  level is the level of interest.
 y=zeros(75,75);

tmp1=clearsource(meshyz(file1,level),level);
tmp2=clearsource(meshyz(file2,level),level);

for i=1:75
 for j=1:75

  if tmp1(i,j)~=NaN,
   y(i,j)=((tmp1(i,j)-tmp2(i,j))/tmp1(i,j))*100;
  else
   y(i,j)=NaN;
  end
 end
end

mesh (y)
```

ERRXY.M Code

```
function y=errxy(file1,file2,level)
```

```
% This function computes the error along one XY slice of two
% files.  File1 is the "correct" fiel and file2 is the file
%which is being compared.  level is the level of interest.
 y=zeros(75,75);


 tmp1=clearsource(meshxy(file1,level),level);
 tmp2=clearsource(meshxy(file2,level),level);


 for i=1:75
  for j=1:75


   if tmp1(i,j)~=NaN,
    y(i,j)=((tmp1(i,j)-tmp2(i,j))/tmp1(i,j))*100;
   else
    y(i,j)=NaN;
   end
  end
 end


 mesh (y)
```

EXPAND.M Code

```
 function y=expand(FILE,THRSH)


% This function takes a file and sets any value above a
% threshold to 30 in order to make the hot points standout.
 y=FILE;
 for i=1:75
  for j=1:75
   if y(i,j)>THRSH,
    y(i,j)=30;
```

```
   end
  end
 end
```

GETAXIS.M Code

```
 function y=getaxis(file);

% This function computes the maximum and minimum of a power
% file in order to get values for the axes of a movie plot.
 SIZE=size(file);

 ZMAX=1;
 ZMIN=0;

 for i=1:SIZE(1,1)
  file1=sqrt(file(i,1)^2+file(i,2)^2+file(i,3)^2);
  if file1>ZMAX,
   ZMAX=file1;
  end
  if file1<ZMIN,
   ZMIN=file1;
  end
 end

 y=[ZMIN ZMAX];
```

IDPXY.M Code

```
 function y=idpxy(idfile,level,stat)
```

```
% This function plots a picture of the specified  XY plane of
%  an ID file. stat is a string describing the IDfile.
 figure
 idxy=clearsource(meshxy(idfile,level),level);
 idxy=idxy;
 colormap(hsv);
 colorbar
 pcolor(idxy);
 xlabel 'X Value'
 ylabel 'Y Value'
 title (['Material id''s across an XY cut at
         Z=',num2str(level),'.'])
 text(15,-7,['Results for ',stat]);
```

IDPYZ.M Code

```
 function y=idpyz(idfile,level,stat)

% This function plots a picture of the specified level of an
% idfile.  stat is a string description of the idfile.
 figure
 idyz=clearsource(meshyz(idfile,level),level);
 idyz=idyz*75/6;
 colormap(hsv);
 colorbar;
 pcolor(idyz);
 xlabel 'Z Value'
 ylabel 'Y Value'
 title (['Material id''s across an YZ cut at
         X=',num2str(level),'.'])
 text(15,-7,['Results for ',stat]);
```

MESHXY.M Code

```
function y=meshxy(file,pln)


% This file creates a mesh in the specified xy plane
% It also tests the file and plots the total field if
% multiple fields are given in the input.

count=(pln);
test=size(file);
for i=1:75
 for j=1:75
  if test(2)==1,
   y(i,j)=file(count);
  end
  if test(2)==2,
   y(i,j)=sqrt(file(count,1)^2+file(count,2)^2)/2;
  end
  if test(2)==3,
   y(i,j)=sqrt(file(count,1)^2+file(count,2)^2+
    file(count,3)^2);
  end
  count=count+75;
 end
end
```

MESHXYN.M Code

```
function y=meshxyn(file1,x,view,TXT)


% This function creates a mesh of the specified yz plane
% and plots the mesh fully formatted.
```

```
y=nrml(meshxy(file1,x),vlu(file1,38,38,38));

figure
y=clearsource(y,x);
colormap(hsv);
mesh(y,view)
xlabel 'X Value'
ylabel 'Y Value'
zlabel '|E|^2 normalized to 1 at center'
title (['E Field Distribution Across XY ',num2str(x),'
    Plane.'])
msg=['Results for ',TXT];
text (-40,35,0,msg)
```

MESHYZ.M CODE

```
function y=meshyz(file,pln)

% This file creates a mesh in the specified yz plane
% It also tests the file and plots the total field if
% multiple fields are given in the input.

count=(pln-1)*75*75+1;
test=size(file);
for j=1:75
 for k=1:75
  if test(2)==1,
   y(j,k)=file(count);
  end
  if test(2)==2,
   y(j,k)=file(count,1)+file(count,2);
  end
  if test(2)==3,
```

```
      y(j,k)=sqrt(file(count,1)^2+file(count,2)^2+
           file(count,3)^2)/2;
    end
    count=count+1;
  end
 end
```

MESHYZN.M Code

```
function y=meshyzn(file,x,view,TXT)

% This function creates a mesh of the specified yz plane
% and plots the mesh fully formatted.

 y=(meshyz(file,x));

 y=clearsource(y,x);

 figure;
 colormap(hsv);
 mesh(y,view);
 shading faceted;
 xlabel 'Z Value'
 ylabel 'Y Value'
 zlabel '|E|^2'
 title (['E Field Distribution Across YZ Plane at
   X=',num2str(x)])
 msg=['Results for ',TXT];
 text (-69,35,-17,msg)
```

MMOVIE.M Code

```
function y=mmovie(file,name,A)


% This function creates a movie through the xy slices of a
% file.  This allows cycling through the levels quickly to
% spot hotspots easily.

Y=moviein(75);


for i=1:75
 j=i
 pcolor(meshxy(file,j));
 caxis(A);
 colorbar;
 colormap(jet);


 title ([name,' at Z=',num2str(j),'.'])
 xlabel 'Y Location'
 ylabel 'X Location'
 y(:,i)=getframe;
end


movie(y)
```

PLOTCY.M Code

```
function y=plotcy(file1,file2,x,Z)
% This fnction plots the power along a y line along with the
% material id's along the line.File1 is the idfile, file2 is
% the power file, and X and Z define the line of interest.

tmp1=meshyzid(file1(:,1),x);
```

```
tmp2=meshyzid(file1(:,2),x);
tmp3=meshyzid(file1(:,3),x);
tmp4=meshyz(file2,x);
k=x2;
I=1:75;
plot(I,tmp1(:,k),'x',I,tmp2(:,k),'o',I,tmp3(:,k),'+',
        I,tmp4(:,k),'-')
xlabel 'Y Value'
ylabel 'Power (W/m^2)'
tmp3=['Total Power with material ID''s at X='];
title ([tmp3,num2str(x),' Z=',num2str(x2),'.'])
```

PLOTCZ.M Code

```
function y=plotcz(file1,file2,x,x2)
% This function plots the power along a Z line along with the
% material id's along that line different files. file1 is the
% id file, file2 is the power file of interest. X and Y
% define the line of interest.


tmp1=meshyzid(file1(:,1),x);
tmp2=meshyzid(file1(:,2),x);
tmp3=meshyzid(file1(:,3),x);
tmp4=meshyz(file2,x);
k=x2;
I=1:75;
plot(I,tmp1(k,:),'o',I,tmp2(k,:),'+',I,tmp2(k,:),
        'x',I,tmp4(k,:),'-')
xlabel 'Z Value'
ylabel 'Power'
tmp3=['Plot of Power and Material ID's at X='];
title ([tmp3,num2str(x),' Y=',num2str(x2),'.'])
```

134

PLOTX.M Code

```
function y=plotx(file,x,x2,type);

% This function plots a power file along a y line.  X is the
% Y value, X2 is the Z location of the line.  type is a
% string giving the style of line to draw.
tmp=meshxy(file,x2);
k=x;
plot (tmp(:,k),type);
xlabel 'Y Value'
ylabel 'E-field strength'
title (['E field along line X=',num2str(x),',
        Z=',num2str(x2),'.'])
```

PLOTY.M Code

```
function y=ploty(file,x,x2,type);

% This function plots the power file along a y line.  X is
% the S value, X2 is the Z value and type is the type of line
% to plot the line as.
tmp=meshyz(file,x);
k=x2;
plot (tmp(:,k),type);
xlabel 'Y Value'
ylabel 'E-field strength'
title (['E field along line X=',num2str(x),',
        Z=',num2str(x2),'.'])
```

PLOTZ.M Code

```
function y=plotz(file,x,x2,type);


% This function plots the power file along a y line.  X is
% the X value, X2 is the Y value and type is the type of line
% to plot the line as.
tmp=meshyz(file,x);
k=x2;
plot (tmp(k,:),type);
xlabel 'Y Value'
ylabel 'E-field strength'
title (['E field along line X=',num2str(x),',
        Z=',num2str(x2),'.'])
```

POWERAVG.M Code

```
function y=poweravg(pfile,idfile,matpar)


% This function computes the average power at the center of
% the head as well as across the entire head.  It also
% computes the power over three different thresholds.  pfile
% is a file of the E-field over the head, idfile is the id's
% of the head mesh, matpar is a file of th ematerial
% characteristics for each id.
Tmp(:,1)=matpar(round(idfile(:,1))+1);
Tmp(:,2)=matpar(idfile(:,2)+1);
Tmp(:,3)=matpar(idfile(:,3)+1);

power=pfile.*Tmp;
power1=sqrt(power(:,1).^2+power(:,2).^2+power(:,3).^2);
```

```matlab
power1=power1/vlu(power1,38,38,38);

% Compute the average power at the center.
 Tmp=0;
 count=0;
 for i=37:39
   for j=37:39
    for k=37:39
     Tmp=Tmp+vlu(power1,i,j,k);
     count=count+1;
    end
   end
 end
 centeravg=Tmp/count
 y(1,1)=centeravg;

% Now compute the average power across the entire head
 hpower=power1(~isnan(power1));
 totalavg=mean(hpower)
 y(1,2)=totalavg;

 y(1,3)=y(1)/y(2);

% Now compute the power spikes
 SIZE=size(hpower)
 numspikes=0;
 num9spikes=0;
 num8spikes=0;
 count=0;
 for i=1:SIZE(1,1);
  count=count+1;
  if hpower(count)>=.8,
   num8spikes=num8spikes+1;

   if hpower(count)>=.9,
    num9spikes=num9spikes+1;
```

```
      if hpower(count)>=1,
        numspikes=numspikes+1;
      end
    end
  end
end

numspikes
y(1,4)=numspikes;
num9spikes
y(1,5)=num9spikes;
num8spikes
y(1,6)=num8spikes;
```

PWRPXY.M Code

```
function y=pwrpxy(file,level,stat)


% This functione plots a picture of the power across the
% level specified.  stat is a string decripter to be printed
% on the plot.
pxy=clearsource(nrml(meshxy(file,level),
        vlu(file,38,38,38)),level);
figure
colormap(hsv);
pcolor(pxy);
colorbar;
brighten(.75);
xlabel 'X Value'
ylabel 'Y Value'
title (['E field magnitude across an XY cut at
        Z=',num2str(level),'.'])
```

```
text(15,-7,['Results for ',stat]);
text(74.5,77,'E field Mag');
```

PWRPYZ.M Code

```
function y=pwrpyz(file,level,stat)

% This function plots apicture of the power across the YZ
% plane specified.  stat is a string descriptor to be used in
% the title of the plot.
pyz=clearsource(meshyz(file,level),level);
figure
colormap(hsv);
pcolor(pyz);
brighten(.75);
colorbar;
xlabel 'Z Value'
ylabel 'Y Value'
title (['E field magnitude across an YZ cut at
        X=',num2str(level),'.'])
text(15,-7,['Results for ',stat]);
text(74.5,77,'E field Mag');
```

SHRINK.M Code

```
function y=shrink(file)

% This function shrinks an idfile from the 92X92X95 grid down
% to a 75X75X75 grid to match the E-field files.

count=0;
counts=0;
```

139

```
 y=zeros(421875,3);
 for k=1:92
  disp(k)
  for j=1:95
   for i=1:92
    counts=counts+1;
     if (i>10 & i<86 & j>10 & j<86 & k>10 & k<86),
      count=count+1;
      y(count,:)=file(counts,:);
     end
    end
   end
  end
 end
```

TERR.M Code

```
 function y=terr(file1,file2)

% this function calculates teh error between two files across
% all of space.
 y=zeros(211873,1);
 count=0;
 count1=0;
 for i=1:75
 i
  for j=1:75
   for k=1:75
    count=count+1;
    if sqrt((i-38)^2+(j-38)^2+(k-38)^2)<37,
     count1=count1+1;
     y(count1)=abs((file1(count)-
           file2(count))/file1(count))*100;
```

```
        end
      end
    end
  end
```

VLU.M Code

```
function y=vlu(file,x,y,z)

% This function finds the value of the file at the specified
% location.
test=size(file);
count=(x-1)*5625+(y-1)*75+(z-1)+1;
if test(2)==1,
 y=file(count,1);
end
if test(2)==3,
 y=sqrt(file(count,1)^2+file(count,2)^2+file(count,3)^2);
end
```

References

(1) Rappaport, C. and Morgenthaler, F. "Optimal Source Distribution for Hyperthermia at the center of a sphere of muscle tissue," *IEEE Microwave Trechnology* : 1322-1327 (December 1987).

(2) Rappaport,C. and Pereira, J. "Optimal Microwave Source Distribution for Heating Off-Center Tumors in Spheres of High Water Content Tissue," *IEEE Transactions on Microwave Theory ond Techniques* : 1979-1982 (October 1992).

(3) Rappaport, C. "Focusing Power at Off-Centert Targets in Biological Spheres-Azimuthal Polarization." In review for publication.

(4) Pereira, J. *Double Layer Ideal Spherical Model of an Optimal Microwave Power Transducer*. MSEE Thesis. The Department of Electrical and Computer Engineering. Northeastern University, Boston, Massachusetts. August 1990.

(5) Luebbers, Raymond J., Penn State FDTD code, version F.

(6) Shaw, Joseph A., Durney, Carl H., Christenen, Douglas A. "Computer-Aided Design of Two-dimensional Electric-type Hyperthermia Applicators Using the Finite Difference Time Domain Method." *IEEE Trans. on Biomedical Engineering*. 861-870 (September 1991)

(7) Johnson, Curtis C., Guy, Arthur W. "Nonionizing Electromagnetic Wave Effects in Biological Materials and Systems." *Proc. of the IEEE*. 692-720 (June 1972)

(8) Stuchly, M.A and Stuchly, S.S. "Dielectric Properties of Biological Substances." *Journal Of Microwave Power*. 19-23 (Vol 15(1), 1980)

(9) Luebbers, R. and Kunz, K. *The Finite Difference Time Domain Method for Electromagnetics*. Ann Arbor: CRC Press, Inc., 1993.

(10) Stratton, Julius A., *Electromagnetic Theory*. St. Louis: McGraw-Hill, Inc., 1941.

(11) Arfken, George. *Mathematical Methods for Physicists*. Third Edition, New York: Academic Press, Inc., 1985.

(12) Balanis, Constantine A. *Advanced Engineering Electromagnetics*. New York: John Wiley & Sons, Inc., 1989.

(13) Stutzman, Warren L. and Theile, Gary A. *Antenna Theory and Design*. New York: John Wiley & Sons, Inc., 1981.

(14) Shen, Liang Chi and Kong, Jin Au. *Applied Electromagnetism*. Second Edition, Boston: PWS Publishers, 1987.

(15) Kreysig, Erwin. *Advanced Engineering Mathematics*. Sixth Edition, New York: John Wiley & Sons, Inc., 1988.

(16) Christensen, D.A. and Durney, C.H., "Hyperthermia Production for Cancer Therapy: A Review of Fundamentals and Methods." *The Journal of Microwave Power and Electromagnetic Energy.* 89-105. (Vol 16(2), 1981).

Vita

Lieutenant David Dunn was born on 14 December, 1970 in Heidelberg, Germany. He grew up in Port Huron, Michigan, graduating from Port Huron Nothern High School in 1989. He Attended the United States Air Force Academy, where he graduated in 1993 with a BSEE. He was accepted into the Air Force Institute of Technology's masters program in May of 1993.

GENERAL INSTRUCTIONS FOR COMPLETING SF 298

The Report Documentation Page (RDP) is used in announcing and cataloging reports. It is important that this information be consistent with the rest of the report, particularly the cover and title page. Instructions for filling in each block of the form follow. It is important to *stay within the lines* to meet *optical scanning requirements*.

Block 1. Agency Use Only *(Leave blank)*.

Block 2. Report Date. Full publication date including day, month, and year, if available (e.g. 1 Jan 88). Must cite at least the year.

Block 3. Type of Report and Dates Covered. State whether report is interim, final, etc. If applicable, enter inclusive report dates (e.g. 10 Jun 87 - 30 Jun 88).

Block 4. Title and Subtitle. A title is taken from the part of the report that provides the most meaningful and complete information. When a report is prepared in more than one volume, repeat the primary title, add volume number, and include subtitle for the specific volume. On classified documents enter the title classification in parentheses.

Block 5. Funding Numbers. To include contract and grant numbers; may include program element number(s), project number(s), task number(s), and work unit number(s). Use the following labels:

C	-	Contract	**PR**	- Project
G	-	Grant	**TA**	- Task
PE	-	Program Element	**WU**	- Work Unit Accession No.

Block 6. Author(s). Name(s) of person(s) responsible for writing the report, performing the research, or credited with the content of the report. If editor or compiler, this should follow the name(s).

Block 7. Performing Organization Name(s) and Address(es). Self-explanatory.

Block 8. Performing Organization Report Number. Enter the unique alphanumeric report number(s) assigned by the organization performing the report.

Block 9. Sponsoring/Monitoring Agency Name(s) and Address(es). Self-explanatory.

Block 10. Sponsoring/Monitoring Agency Report Number. *(If known)*

Block 11. Supplementary Notes. Enter information not included elsewhere such as: Prepared in cooperation with...; Trans. of...; To be published in.... When a report is revised, include a statement whether the new report supersedes or supplements the older report.

Block 12a. Distribution/Availability Statement. Denotes public availability or limitations. Cite any availability to the public. Enter additional limitations or special markings in all capitals (e.g. NOFORN, REL, ITAR).

DOD	-	See DoDD 5230.24, "Distribution Statements on Technical Documents."
DOE	-	See authorities.
NASA	-	See Handbook NHB 2200.2.
NTIS	-	Leave blank.

Block 12b. Distribution Code.

DOD	-	Leave blank.
DOE	-	Enter DOE distribution categories from the Standard Distribution for Unclassified Scientific and Technical Reports.
NASA	-	Leave blank.
NTIS	-	Leave blank.

Block 13. Abstract. Include a brief *(Maximum 200 words)* factual summary of the most significant information contained in the report.

Block 14. Subject Terms. Keywords or phrases identifying major subjects in the report.

Block 15. Number of Pages. Enter the total number of pages.

Block 16. Price Code. Enter appropriate price code *(NTIS only)*.

Blocks 17. - 19. Security Classifications. Self-explanatory. Enter U.S. Security Classification in accordance with U.S. Security Regulations (i.e., UNCLASSIFIED). If form contains classified information, stamp classification on the top and bottom of the page.

Block 20. Limitation of Abstract. This block must be completed to assign a limitation to the abstract. Enter either UL (unlimited) or SAR (same as report). An entry in this block is necessary if the abstract is to be limited. If blank, the abstract is assumed to be unlimited.